University of Nebraska - Lincoln

DigitalCommons@University of Nebraska - Lincoln

Mechanical (and Materials) Engineering -- Dissertations, Theses, and Student Research

Mechanical & Materials Engineering, Department of

8-20-2013

Flow-Induced Crystallization of Isotactic Polypropylene and Random Polyethylene-Polypropylene Copolymers

Frederic Aubin
University of Nebraska-Lincoln, af-pro@orange.fr

Follow this and additional works at: https://digitalcommons.unl.edu/mechengdiss

 Part of the Other Mechanical Engineering Commons

Aubin, Frederic, "Flow-Induced Crystallization of Isotactic Polypropylene and Random Polyethylene-Polypropylene Copolymers" (2013). *Mechanical (and Materials) Engineering -- Dissertations, Theses, and Student Research*. 60.
https://digitalcommons.unl.edu/mechengdiss/60

This Article is brought to you for free and open access by the Mechanical & Materials Engineering, Department of at DigitalCommons@University of Nebraska - Lincoln. It has been accepted for inclusion in Mechanical (and Materials) Engineering -- Dissertations, Theses, and Student Research by an authorized administrator of DigitalCommons@University of Nebraska - Lincoln.

FLOW-INDUCED CRYSTALLIZATION OF ISOTACTIC POLYPROPYLENE AND RANDOM POLYETHYLENE-POLYPROPYLENE COPOLYMERS

By

Frederic Aubin

A THESIS

Presented to the Faculty of

The Graduate College at the University of Nebraska

In Partial Fulfillment of the Requirements

For the Degree of Master of Science

Major: Mechanical Engineering and Applied Mechanics

Under the Supervision of Professor Lucia Fernandez-Ballester

Lincoln, Nebraska

August, 2013

Flow-induced crystallization of isotactic polypropylene and random polyethylene-polypropylene copolymers

Frederic Aubin

University of Nebraska, 2013

Adviser: Lucia Fernandez-Ballester

Flow-induced crystallization (FIC) has been investigated for decades but the effect of molecular characteristics that hinder crystallization—such as the presence of random comonomers— on FIC remains scarcely explored. Flow greatly enhances crystallization kinetics and can induce the formation of highly oriented morphologies that affect final properties (i.e. stiffness, permeability, thermal conductivity, elastic modulus, etc.). Therefore, understanding FIC remains particularly important for developing predictive models to allow optimization of processing techniques involving flows.

Polypropylene represents ~ 40% of the global polyolefin production. The addition of ethylene comonomer allows their use as engineering plastics because of their particular toughness and flexibility. This study explores the influence of ethylene content on FIC by using isotactic polypropylene and random ethylene copolymers and imposing high shear stress in a pressure driven flow. The types of morphologies formed are compared for all three grades, as well as the required critical shear stress σ_{crit} for formation of oriented crystallites. A depth sectioning method has been used to explore the oriented nucleation densities within the highly oriented skin in all three grades. A saturation behavior has been detected for iPP and 3% ethylene—but not for 7% content—which correlates with an increase in viscosity.

ACKNOWLEDGEMENTS

I would like to thank all the persons that helped me during these last two years.

I firstly would like to thank my supervisor Dr. Lucia Fernandez-Ballester. Thank you Lucia for your great interest, your assistance and your remarkable guidance though this project, it was very enriching and enjoyable to work with you.

I would also thank Jean-Marc Saiter, Mehrdad Negabahn and Eric Dargent who made the exchange between the university of Rouen and UNL possible. It was an enriching and enjoyable experience.

I would also thank all the students whom I had the pleasure to meet during this project; I will keep you in my heart.

Finally, I would like to thank my family. I couldn't be at this point without you.

CONTENTS

LIST OF FIGURES

LIST OF TABLES

Chapter 1 INTRODUCTION

1.1 Isotactic Polypropylene

Polypropylene (PP) is one of the simplest polyolefins along with polyethylene (PE). Polypropylene is obtained by polymerization of propylene and consists of a sequence of ethylene monomers on the back-bone with a methyl side group on every other carbon. The three possible configurations of the methyl side groups in space—the tacticity—have a large impact on the mechanical, thermal and optical properties of the material For instance, atactic PP (aPP) has methyl groups randomly oriented, which precludes it from crystallizing (Figure 1.1, bottom). Differently, isotactic PP (iPP) has methyl groups on one side of the back-bone and is able to crystallize due to its regular structure (Figure 1.1, top). Likewise, syndiotactic polypropylene (sPP) has methyl group alternatively arranged on either side of the back-bone and is able to crystallize (Figure 1.1, middle).

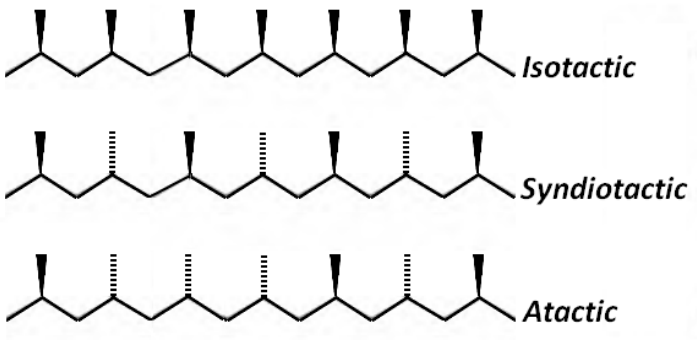

Figure 1.1 Schematic representation of stereo-configuration of polypropylene.

Syndiotactic PP (sPP) is obtained by alternative addition of two stereo-isomeric configurations specific of Ziegler-Natta's catalysis. The atactic form (aPP) is obtained by classical radical reaction. Isotactic polypropylene (iPP) is obtained by polymerization of only one isomeric configuration of propylene monomer [1]. Only the crystallization of the isotactic configuration will generate crystalline forms such a monoclinic α phase, an hexagonal β phase or a triclinic γ phase, but some intermediate forms of crystalline have been observed with the syndiotactic configuration [2]. These forms will be discussed in another chapter in this thesis.

Isotactic polypropylene (iPP) is a thermoplastic that is used in a wide range of applications because of its remarkable properties such as hardness, high tensile strength and chemical resistance [3]. It is the most common form of PP found commercially, is stiff and is one of the polymers with lowest density. Its glass transition is of -8°C and its nominal melting point lies in a range of 165 to 175°C. The degradation occurs around 350°C but starts at lower temperatures in solution (230°C) [4].

1.2 Crystalline structure of iPP

Within the crystalline structure of iPP, the chains usually take a helicoidal shape. Their spatial conformation is such that the side groups of the chain arrange to get the intermolecular energy to be the lowest [3].

Three major phases can be present in iPP depending on the experimental conditions. These phases have an impact on the kinetics of crystallization and the final microstructure. The α and β phases of isotactic polypropylene are major constituents in bulk crystallization in comparison to the γ phase [5] and share the same three-fold helical conformation. While the growth rate of the more stable α phase is slower than the less stable β phase, the metastable β-iPP melts at a lower temperature than αiPP, Tm_β ~ 155°C and Tm_α ~ 170°C respectively [6].

The β phase has a trigonal unit-cell with the following parameters a = b = 11.0 Å, c = 6.5 Å and β = 120° (Figure 1.2) [2]. It can be obtained by using β nucleating agents, under large temperature gradients and under shear. Nevertheless, a recent study [7] determined that, under flow, an increase of shear is responsible for an increase of the α-phase at the expense of the β-phase meaning that, for highly sheared duct flow, β-iPP must be present at very low scale.

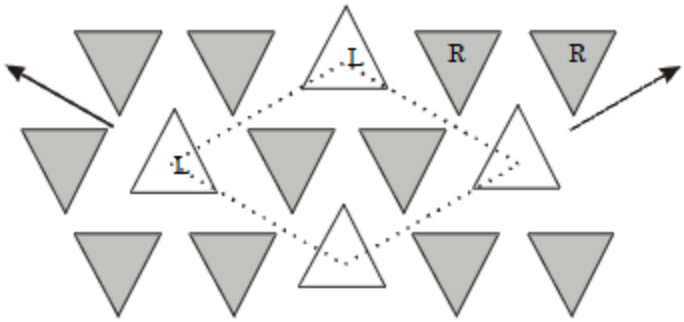

Figure 1.2 **Schematic representation of β-phase reproduced from reference *[2]*. b-axis are represented by the arrows while c-axis is perpendicular to the plane of view.**

The α form of iPP has a monoclinic unit cell with parameters a = 6.65 Å, b = 20.96 Å, c = 6.5 Å and β = 99.62° (Figure 1.3) [2]. αiPP has a unique particularity in the generation of daughter lamellae which grow at an angle of 80° from their parent lamellae and generate a structure called 'cross hatched'.

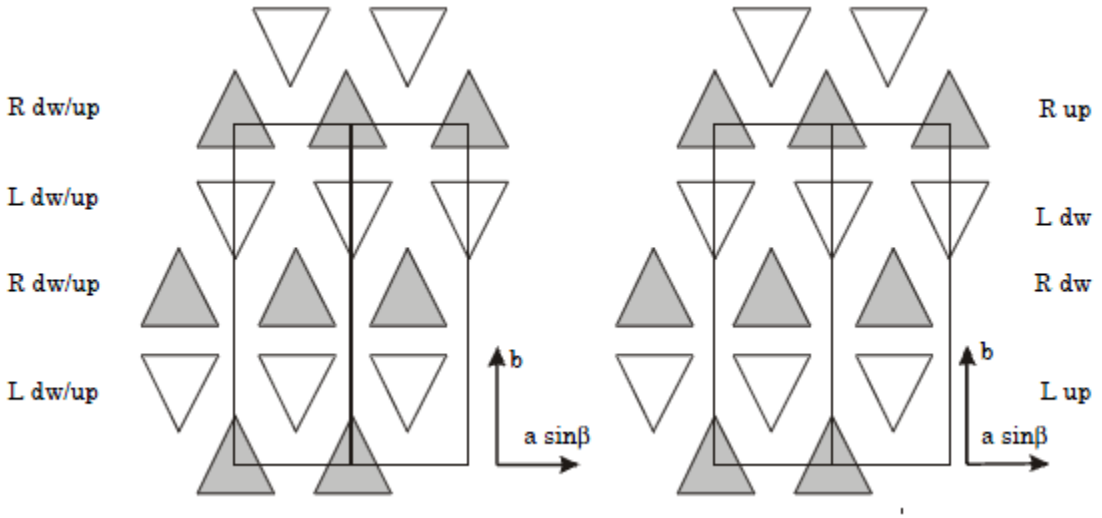

Figure 1.3 **Schematic representation of α-phase reproduced from reference *[2]*. Two different α-phases can be recognized depending on the position of the methyl group and are classed as left : disordered and right : ordered. The c-axis is perpendicular to the plane of view**

The interdigitation of methyl groups as well as the close identity of the two axis a and c from the cell of this crystal encourage the development of α daughter branching at 80° [8]. Therefore, a higher chance to observe this phenomenon will be particularly

observed with copolymer of iPP with a range of methyl high enough to affect the overall amount of defects and therefore the amount of seeds for the branching. The concentration of stereo and regio defects as well as the stereoregularity are then important parameters for α branching [2], but they also remain important for the formation of the particular γ phase [9].

These α and γ phases are particularly related, because the γ phase acts similarly to the α branching. While daughter α lamellae grow on parent lamellae at 80°, the γ phase grows on α parent lamellae with an angle of 40°, which represents an epitaxial growth on the lateral (010) plane of the unit cell (Padden and Keith, 1973). Due to the 80° angle between parent and daughter lamellae in the α phase, a γ lamellae grown from a parent will also have a 40° angle with respect to the daughter lamellae [2]. Differently from the α phase—which has its fastest growth along the a-axis—the γ phase has its fastest growth at right angle to the α phase, along the c-axis [10]. Therefore, the γ phase forms elongated filaments for high molecular mass of iPP. The structure of γ phase is an orthorhombic cell with the following parameters a = 8.54 Å, b = 9.93 Å and c = 42.41 Å [2]. Two different chain directions composed its unit cell within a non-parallel direction which can be perceived as a α-quadrite constituting a unique character of γ phase crystallites [2].

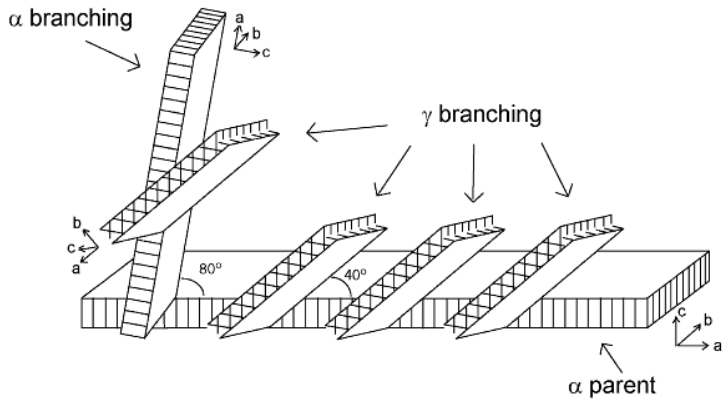

Figure 1.4 **Schematic representation of α and γ branching from a parent α-lamellae (with representation of cross hatching) from reference *[10]*.**

For iPP melts, formation of α crystals occurs in the beginning of crystallization, while γ crystals are only observed at longer crystallization times [11] because nucleation of the γ form requires the presence of α parent lamellae. A high crystallization rate will therefore favor the α phase of iPP in regard to the γ phase while the trend will change favorably to the γ phase with a low crystallization rate [12]. Mezghani and Phillips have shown that the formation of γ phase depends on pressure and temperature [9]. Additionally, one has to consider the role of the defects which shorten the crystallizable length of the chains and decrease of the crystallization rate. Several studies have shown that stereoregularity and comonomers favor the γ phase [2] [9] [10].

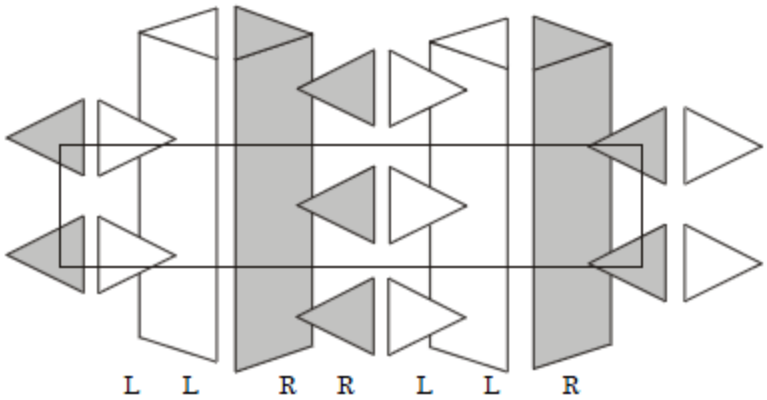

Figure 1.5 **Schematic representation of γ-phase reproduced from reference *[2]*.**

The equilibrium melting temperature for fully isotactic polypropylene for the γ phase is 186.1°C [11]. For the α phase, the equilibrium melting temperature is reported ~ 186°C or ~ 220°C depending on the study [13]. The equilibrium melting temperature of the β phase is typically reported to be ~ 177°C [2].

Other phases of iPP exist, but are quite rare and still discussed. A sharp quench of polypropylene will not provide a totally amorphous phase but have certain intermediate crystalline order [2].

1.3 Quiescent crystallization of polymers

1.3.1 Nucleation and growth

The nucleation and growth of polymers meets some major difficulties to combine theories with experimental data. The most accepted approach is the use of an extension of the nucleation and growth process for small particles adopted by Hoffman [14]. At the equilibrium melting point $T_{m,eq}$, consisting to the theoretical required temperature to

completely melt an ideal crystal, the Gibbs free energy ΔG is null. When the temperature $T < T_{m,eq}$, the polymer is subject to undercooling and a driving force arises for crystallization. A nucleus has then to be formed, but this process has an activation energy.

With the relation known between the Gibbs free energy and the enthalpy H with entropy S, a useful expression for ΔG_m can be used with the enthalpy of mixing H_m and the entropy of mixing S_m [14].

$$\Delta G_m = \Delta H_m - T\Delta S_m \quad (1)$$

The primary nucleation step has been envisaged by the creation of small cylindrical crystalline embryo from the package of few molecules side by side. There are two contributions to the ΔG of this process: the addition of molecules in the crystal causes a decrease of G (proportional to the crystal volume), but at the same time the creation of crystal surface leads to an increase of G (free energy penalty, or surface tension penalty). If the embryo is very small, the ratio between its surface and its volume is high and any increase in size of the embryo entails an increase in free energy G because the interfacial contribution dominates. However, if the size of the embryo becomes large enough, the ratio of surface-to-volume decreases leading to a decrease of G with further grows. This particular point is called the critical size r_c and define the size over which an embryo is stable enough to create a nucleus favorable for the creation of a crystal (Figure 1.6) [14]. The peak corresponding to the critical size can be recognized as an energy barrier where at crystallization temperature, thermal fluctuations are such that this energy can be overcome which for a nucleus larger than this critical size will grow spontaneously.

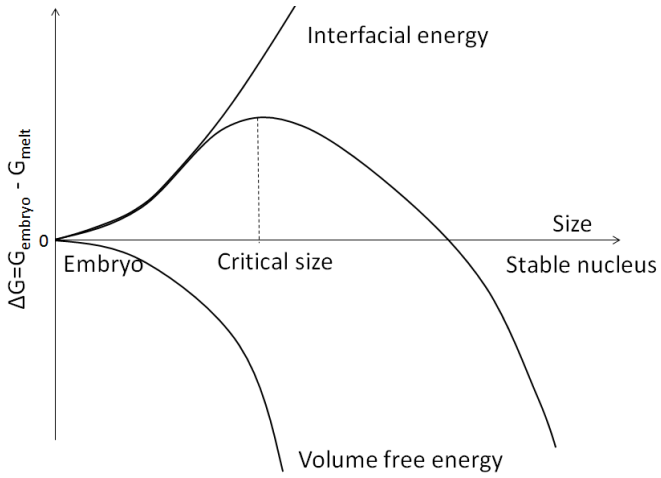

Figure 1.6 Schematic representation of the creation of nucleus by changes in free energy during polymer crystallization.

Once the primary nucleation process starts, the secondary nucleation process (growth) can take place on a pre-existing crystal surface. Similarly to primary nucleation, secondary nucleation also has an activation energy barrier, but it is lower due to the smaller surface per unit volume of crystal created, molecules are added onto an already existing molecularly smooth crystal surface (Figure 1.7). A molecular stem first lays down on a smooth crystal surface and then, by chain folding, other segments can be added next to it if the molecules are flexible enough and the rotation about the polymer backbone is relatively free [14].

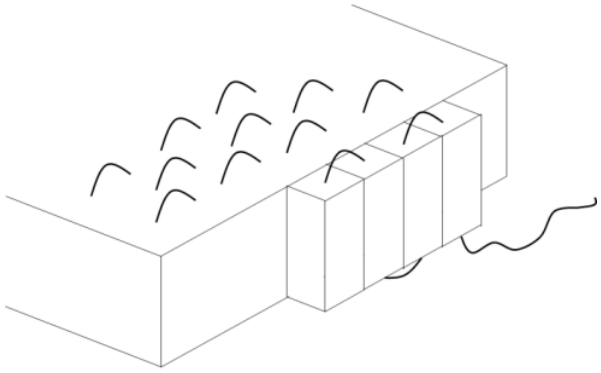

Figure 1.7 **Schematic of a secondary nucleation by succession of laying down of adjacent molecular stems.**

The nature of chain folding remains controversial even today, for melt crystallized crystals, the radius of gyration in solid crystalline polymer revealed by SANS experiments are very close to that in the melt state [15]. It was proposed in some analyses a non-adjacent re-entry meaning that stems from a given chain are separated by at least two stems from another chain.

1.3.2 Morphology

The addition of stems in the way described above form platelet-like crystals called lamellae. The polymer molecular weight and the degree of supercooling ($\Delta T = T_{m,eq} - T_c$) govern the lamellae thickness [16]: longer molecules and higher crystallization temperatures leads to thicker crystallites. For crystallization from a polymer melt, the regions between lamellae remain amorphous. This amorphous phase is composed by molecule loops, entanglements and chain ends and constitutes a weak linkage within the polymer [16]. Semi-crystalline polymers are characterized by their crystallinity defined as the ratio between the amount of crystals and the whole structure.

For melt crystallization, lamellae can arrange themselves into different superstructures depending on crystallization conditions (hedrites, axialites, spherulites) [17]. Spherulites are the most common. They are three-dimensional structures that form from branching and twisting of lamellae which grow in radial direction starting from a central nucleus. In a spherulite, polymer chains lie perpendicular to the radius of the spherulite. Due to this arrangement and to the fact that the index of refraction is different along and perpendicular a polymer chain (birefringence), an extinction pattern called Maltese Cross is observed under polarized optical microscopy. Sometimes, the Maltess cross cannot been seen, and sometimes regular concentric banding appear and are due to twist of lamellae along the growth direction (Figure 1.8) [18] [19].

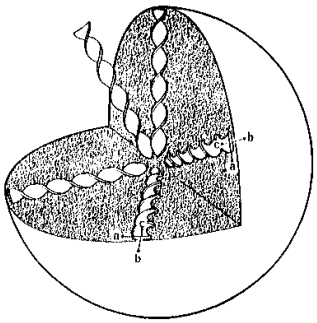

Figure 1.8 Schematic representation of lamellae twisted into a spherulite and growing from a single nucleus [19].

The morphology obtained under non-isothermal crystallization is strongly dependent on the cooling rate. For high cooling rates, the lower temperatures favor nuclei formation resulting in a higher number of spherullites and therefore, smaller sizes. Nucleation can even been bypassed if the polymer is quickly quenched to temperature below the glass transition temperature and can result in an entirely amorphous phase [20].The degree of crystallization is higher when slow cooling rates are used [14].

1.4 Flow induced crystallization

1.4.1 Introduction

In industrial conditions, polymer processing implies high levels of shearing and elongational flow on molten polymers. Macromolecules can undergo orientation and stretching depending of the strength of flow while passing into a cavity [21]. Polymer melts also experience high temperature gradients and high cooling rate due to the contact with the wall of the mold. The combination of high cooling rate and flowing melt leads to the formation of anisotropic and non-homogeneous structures that differ from the morphologies that develop under quiescent and isothermal conditions.

Under these conditions, at least three and up to six different layers can be observed [22]. An oriented skin layer appears near the wall composed of non-spherulitic structures created during sudden freezing due to the cold mold at the wall. An intermediate layer composed of conical spherulites is observed and is explained by the thermal gradient present during their formation. Innermost, the core of the sample is composed of spherulites with high crystallinity formed under isothermal crystallization conditions. The thickness of these layers depends on the processing conditions [23].

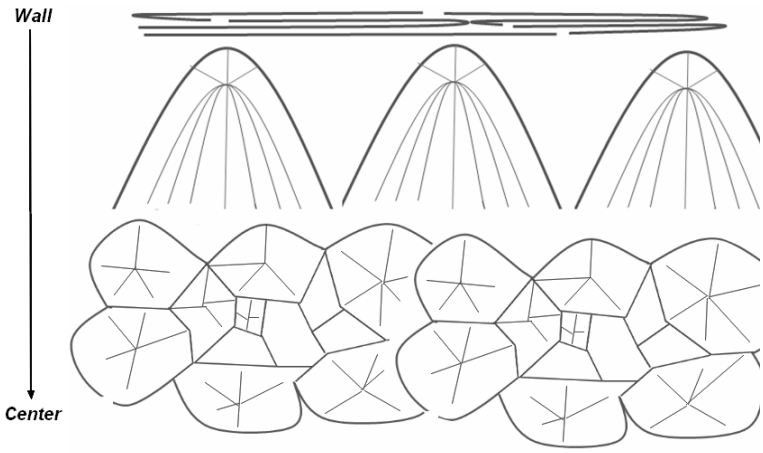

Figure 1.9 Schematic representation of polymer morphologies occurring during injection in a mold

Under flow, the kinetics of crystallization of polymers can drastically change [24]. The long chains can undergo large deformations which lead to chain stretching, especially when the concentration of these chains is such at or above their overlap concentration [25]. The result of this stretching is thought to be key to the formation of oriented precursors [26], onto which oriented lamellae nucleate. This large increase in nucleating surface results in a considerable increase of the crystallization rate and high orientation. While under quiescent conditions the crystallization is entrained by the free energy difference between the crystalline phase and the amorphous phase, under flow the melt's free energy observes changes by an increase of the order degree of polymer morphology [27]. The stretching of the chains lowers the conformational entropy which has the effect to reduce the free energy barrier for crystal formation [28].

1.4.2 Proposed model of parameters

One theory relies on dormant nuclei that would exist in the undercooled melt and upon cooling become activated [29]. The work of Janeschitz-Kriegl has brought them to the conclusion that flow treatments allow the activation of nuclei similarly to those

obtained after an effective quench. With Polypropylene, experiments were conducted at temperatures ranging from 140°C to 160°C where in the quiescent melt the initial amount of nuclei remains relatively small, after flow the density of nuclei increased by at least one million [29]. A high rate of work (shear rate times shear stress) is necessary in order to activate these dor mant nuclei, low rate of work trend the sample to behave as in a quiescent melt [30]. The rate of work is then an important factor for the activation of these initially spherical nucleuses formed from the condensation of an undercooled vapor which by the flow are continuously elongated to form "Fringe micelles [30].

Point precursors leads on the growth of spherulites on them after cessation of flow, this growth will continue until all the free space is filled, but this space is limited by the number of precursors which continuously increases during the flow. A long shearing time will then create a high density of precursors but then a reduced free space between them to allow the growth of spherulites [30].

1.4.3 Some parameters thought to be the controlling forces

Many works have been established on flow induced crystallization, Eder et al have brought a premise of description of flow induced crystallization by assuming the shear rate as the driving force of the crystallization [31]. So that, the shear rate can be used as a prediction tool to figure for example the amount of 'shish kebabs' structures and their length [32], however, this model relies on kinematics of the flow and do not take in consideration the dynamics of the molecules in the melt. Other models such ito's and Verhoyens model has brought out that the amount of nuclei formed during flow are dependent of the amount of strain or the viscous stress [33] [34].

The formation of highly oriented crystallization precursors during flow will favor radial growth of oriented lamellae resulting to the so called “shish-kebabs” structure. This structure has an important impact for the final properties of the material as it increases stiffness and decreases permeability [35]. This change in the microstructure is particularly followed for the industry, as it has an influence on dimensional accuracy, dimensional stability thermal conductivity, modulus and strength evidenced in the work of Emmanuelle Koscher and René Fulchiron [36].

We call “Thread-like nuclei” elongated nucleus from flow which will form the basis of the shishs structure. Those precursors can appear in high temperatures in the melt of polymer and in the case of polypropylene close to the equilibrium melting temperature if subject to an intense shear [29].

The structure shish-kebab arises from the oriented precursors that provide nucleating sites for the growth of lateral folded-chain crystals called kebabs. These precursors are oriented parallel to flow and (oriented lamellae) hence the kebabs that grow radially are transverse to the flow [24].

Under duct flow, for a high and sudden pressure released on the polymer we generally can distinguish highly oriented layers commonly called “skin” or “skin layer” for PP emerging from the wall and sometimes followed by a fine grain layer. As knows, shear stress decreases linearly from the wall to the center of the sample; we have seen previously that the creation of oriented precursors relies on high shear stresses explaining that this oriented layer can only be found close the wall [37]. While the skin consists of a

shih kebab structure, the fine grain layer has been reported to be of thread like structures perpendicular to the flow direction [38] or small spherulites arising from point-nuclei.

The explanation of the existence of these well-defined layers remain possibly related to the behavior of the flow itself during shear, the Non-Newtonian nature of the flow implies a sharp decrease of the shear rate with the increasing distance from the wall. In this condition, the plug flow can be reached for high rate of flow. Thus, the product of the shearing time and the local shear rate giving the total shear has its value decreasing tremendously when the distance from the wall increase [29]. One has also to consider the activation of nuclei during flow which become more and more numerous during the shear. While their density increases, their length also increases to form the shish structure and arrive to a point where the space for the growth of spherulites becomes limited. This parameter associated to the share rate change leads to a sharp transition between an oriented area containing a dense quantity of shish growing their kebab structure and an area with grain layer. The transition can even be such high that the fin grain layer can be absent. For a shear rate not high enough to activate nuclei, the oriented skin will simply not appear [29].

1.4.4 Effect of molecular weight / long chain distribution

We can define the critical shear stress the value of shear threshold where orientation can appears. Are also defined the critical orientation molecular weight (M*) the minimum molecular weight for a chain to be able to form stable nuclei and being oriented for a given shear rate. Hsiao et al have calculated M* for iPP for a temperature

of crystallization at 140°C a shear strain of 1428% and a shear rate of $57s^{-1}$ to be around 300,000g/mol [39].

The molecular weight M_w as well as the polydispersity has an important effect under crystallization flow. Due to the longer time to relax for high molecular weight chains after application of shear, some orientation is retained into the melt before the subsequent crystallization, therefore, any increase of M_w or polydispersity will lead to an increase of crystallization under flow especially for iPP [40]. This effect has been noticed in particular in LCB-iPP. Long Chain Branched isotactic polypropylene or LCB-iPP was investigated by in situ rheo-SAXS and WAXD [41] and showed for a brief impulse of shear the fraction of oriented crystal was higher compared to the linear iPP polymer. The crystallization kinetics had an order of magnitude over more than one order in regard to the conventional iPP. In fact, any contribution that increases the relaxation time of molten polymer chains under flow crystallization will enhance the formation of oriented nuclei implying a faster rate of crystallization.

This influence of molecular weight on orientation comes directly from the propriety of the critical shear rate which, at a given temperature, is function of molecular weight and therefore agrees the work of Eder et al cited previously. The longer the chain is and the lower the required strain rate is to extend chains, so that a lower flow field can be applied [42] . This characteristic imply for a given polymer to observe chains fully stretched and chains basically not extended, an increase of the shear rate will not fundamentally increase the degree of orientation of chains by stretching them more, but increase the amount of ‘shishs’ meaning the chains being in an extended state [43].

1.4.5 4-steps governing the formation of shishs

The formation of the shish is still under investigation, it can rise from the growth of a single event or from the alignment of several nuclei [44]. This last hypothesis is explained in this section.

Orientation under flow can be resumed in 4 stages [26].

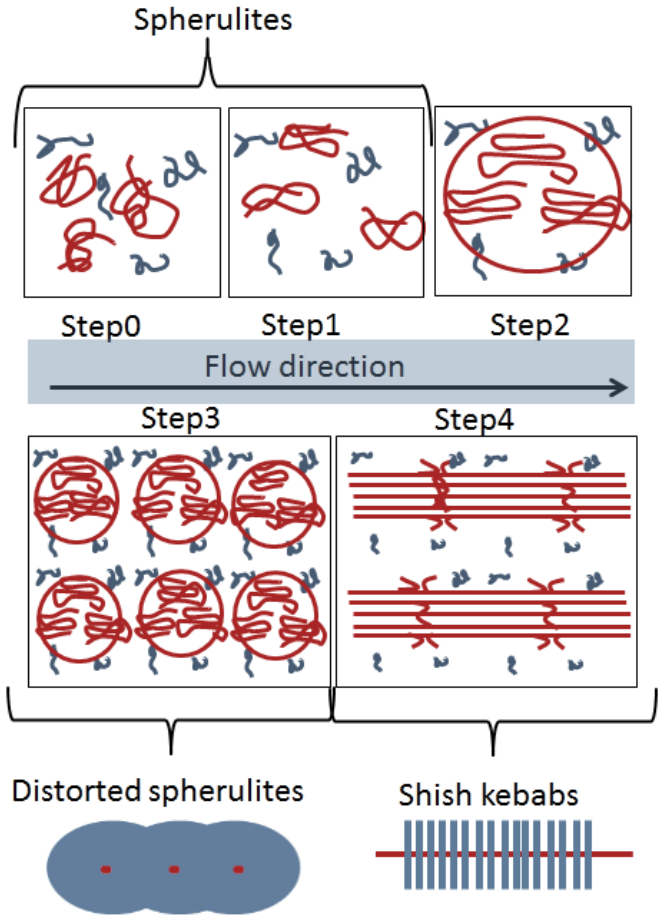

Figure 1.10 From the melt (Step0), molecules are stretched (step1) and aggregate into nuclei (step2) which align with neighboring nuclei to form rows (step3) that impinge resulting to shish structures (step4) that act as nucleating agent for the growth of kebabs. If the flow is stopped at step0 or 1, spherulites structures develop, at step 3 rows of nuclei impinge to form distorted spherulites and the typical Shish-kebab structure is obtained at step 4.

The stretch of molecules is considered to be the first step to form the shish. The shear has to be sufficiently long regarding the rouse time relaxation of the molecules. A

shear pulse with a comparable time than the rouse time would result in a relaxation of the molecules in their initial state such as in quiescent conditions. The aggregation of stretched segments of molecules nucleates into an anisotropic point like nuclei if the aggregate is larger than the critical size of stable nucleus. Caused by the strain, neighboring nucleus undergo alignment prior of the threadlike (shish) formation. Under such state, the cessation of flow would generate distorted spherulites as shish nuclei would initiate their crystal growth from their secondary nucleation and impinge between each other by their proximity. For a prolonged shearing, rows of aligned nucleus continue to aggregate with the continuous formation of shish nuclei. The interface between aggregate disappears to form aggregates energetically more favorable resulting to long crystallized structures (shish) acting as nucleating agent. The epitaxial growth is then rendered possible and kebabs can develop [26].

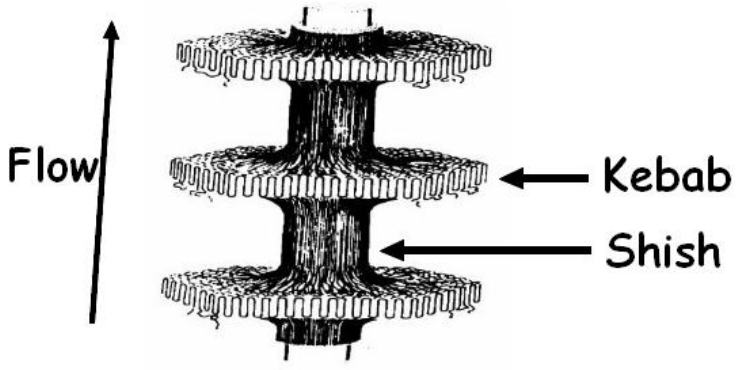

Figure 1.11Representation of a shish-kebab structure, from reference [45]

1.5 Random copolymers and crystallization

1.5.1 Structure of copolymers

A homopolymer consists on the repetition of a single type of repeat unit. When more than one type of repeat unit is present, the polymer is referred to as a copolymer. Several types of copolymers can be found depending on the co-monomers arrangement. Block copolymers have an arrangement of different blocks of monomer distributed linearly or radially (A-A-B-B). Alternating copolymers have a regular and alternating arrangement of monomers (A-B-A-B). Random copolymers have a random distribution of the comonomers.

1.5.1 Crystallization

Several views can rise as two extremes models of lamellar random copolymer (composed of a mixture of A and B units) crystal morphology can be represented; the first one assuming the exclusion of comonomer B units responsible of defects from lamellae composed exclusively of comonomer A units and the second one based on the inclusion of defects in the lamellae by the presence of comonomer B units in the crystalline phase [46]. It has been observed that the type of polymer and comonomer influence the state of inclusion or exclusion of the defect into the lattice crystalline, Alamo et al went to the conclusion that polypropylene with ethylene units are in an intermediate case implying partial exclusion [47].

Figure 1.12 **Schematic representation of lamellae crystals including the exclusion model (left) and the inclusion model (right)**

The exclusion model allows the observation of influence of molecular weight and composition fraction of random copolymer on crystallization kinetics independently [48]. At a given undercooling, the addition of co-unit content drastically decreases the crystallization rate. The distribution of crystallizable units affects the kinetic aspect of copolymer crystallization; the increase of accumulation of non crystallisable sequences from the residual melt affects the undercooling by decreasing the melting point temperature. Hence, the crystallization rate during isothermal crystallization may be altered and decreases with time [48]. This depression of the undercooling with the increase of non-crystallizable units also results into a decrease of nucleation rate.

Experimentally, random copolymers with comonomers that are excluded from the crystal melt over a larger range of temperature than homopolymers. The presence of excluded units “along the otherwise crystallizable backbone” and the varying lengths of the crystallizable sequences may explain this difference [49]. The presence of these excluded units causes a decrease in crystallite thickness. The scantiness of the longest sequences in random copolymers precludes an accurate determination of the equilbrium melting point [50].

From the Flory theory for random copolymer, the melting temperature and the crystallinity are function of temperature and the distribution of the sequence length [49]. This theory explains that the thickness of the crystallite for stable crystals meet a minimum which implies that the sequences of units to form crystals have a minimum length to respect in order to form stable crystal [49]. This sequence length relies on the crystallization temperature Tx thus, an increase of Tx will lead to a highest minimum. Close to the melting temperature, the sequence length is the highest and therefore the crystallites formed will be thicker.

On polypropylene, the crystallinity Xc decreases with the addition of ethylene content due to the increased depletion of length and number of crystallizable sequences [48]. This decrease is particularly high for the random copolymer than for the block copolymer [1].

1.5.2 Equilibrium melting point

Thermodynamically, the equilibrium melting point is also affected. A depression of the crystalline melting point happens due to the required preferential ordering of the copolymer chains for crystallization that increases the entropy of fusion according to Flory [51]. Following several assumptions described elsewhere [46] one can define the following equation for the melting temperature of a lamellar copolymer crystal ($T_{m(l)}$):

$$T_{m(l)} = \left\{1 - \frac{2\,\sigma e}{\Delta H(T_{m0})}\left(\frac{1}{l}\right) - AX\right\} T_{m0} \qquad (2)$$

With σ_e The surface free energy of the basal plane of the lamellar crystal, T_{m0} the equilibrium melting point of the homopolymer, *A* the ratio of the heat of

transition associated with the formation of a defect in the crystalline lattice over the heat of fusion from the homopolymer and *l* the thickness of a lamellar crystal. The depression here is due to the defective heat of fusion accompanying the crystallization.

Two extrapolations methods can be used for the equilibrium melting point determination, known as the Gibbs-Thomson (GT) method and the Hoffman-Weeks (HW) method [52]. The GT method, already been reviewed through the equation (2) in this report is, with the HW in equation (3), highly dependent on lamellar thickening. The determination of the lamellar thickness however, is determined at the room temperature for GT, which may vary during melting. The HW method requires the thickening coefficient to be independent of the crystallization temperature to be accurately computed [52]. Using both methods, Mezghani et al found different values of T_{m0} for iPP with 186°C and 210°C for GT and HW respectively [53]. Observations on copolymer P/E RACO with 7.3% of ethylene content revealed severe discrepancies of about 20°C difference for T_{m0} [52].

$$T_m = T_{m0}\left\{1 - \left(\frac{li}{l}\right)\right\} + \frac{T_c . li}{l} \quad (3)$$

With T_c the temperature of crystallization and l / l_i the thickening coefficient [52].

From the easiness to make error from these two procedures, the determination of equilibrium melting point for iPP and particularly for RACO's is arduous.

1.5.3 Crystalline phases in PP and random copolymers.

In the case of polypropylene, an addition of ethylene content also impact on the ratio of the two polymorphic forms created during isothermal crystallization. Indeed, the increase of the ethylene concentration result in an increase of the orthorhombic crystal form (γ-form) compared to the monoclinic crystal form (α-form) that impact on the kinetics and mechanism of growth [54].

1.6 Aim of the project

Flow-induced crystallization has been an important subject in polymer processing from decades and has raised many works. Polymers under flow, such isotactic polypropylene, have been thoroughly studied. Its behavior under flow is henceforth well known, and its quiescent crystallization does not reserve any more surprises.

The rising interest in the use of engineering plastic, requirement of addition of defects such polypropylene copolymer with ethylene units, brings a certain interest in the study of such polymer under flow crystallization.

Few works have been made on the crystallization of these plastics under very high shear stresses. Several experiments have been carried out through cone and plate rheometer as for example [52], however, these kind of rheometers are limited from their geometry and the shear applied remain much lower than shear conducted through slit duct like the one use in this project [55].

A recent work has been carried out with P/E RACO units with the use of cartridge similar to this project through WAXD analysis [56]. This project is to be complementary with the observance of the influence of ethylene content through three different grades thanks to in-situ measurement of birefringence and ex-situ observation under the use of optical polarized microscope.

Chapter 2 Experimental methods

2.1 Materials

In this study, an isotactic homopolymer PP (Borealis HD244CF) and two random copolymers propylene/ethylene Raco3 and Raco7 (Borealis RD204CF and RD208CF) are used (Table 2.1). They were produced by bulk polymerization in liquid propylene and a fourth-generation Ziegler-Natta type catalyst with a conventional external donor at a commercial scale [57]. The three grades have the same weight average molecular mass and polydispersity with M_w ~ 310 kg mol^{-1} and M_w/M_n ~ 3.4 respectively [57]. Thereby, all three grades have similar rheological behavior [52].

Their nominal melting temperature (T_m) is 164, 153 and 139 for PP, Raco3 and Raco7 respectively (Table 2.1). Melting enthalpy (ΔH_m) and crystallization temperature (T_c) were determined by DSC (ISO 3146) at a cooling rate of 10K min^{-1} [57]. The crystallinity has been deduced using $X_c = \Delta H_m / \Delta H_{m0}$ with $\Delta H_{m0} = 209$ J g^{-1} [52].

Table 2.1 Characteristics of PP, RACO4 and RACO8 from literature [57] [52].

Name	Type	Ethylene content		Tm by	Tc
		FTIR(wt %)	NMR(mol %)	DSC (°C)	
iPP (homo)	HD244CF	0	0	164	110
RACO3	RD204CF	2.2	3.4	153	105
RACO7	RD208CF	4.9	7.3	139	98

The Raco3 and Raco7 manifest a higher chance of creating γ-phase under the following processing: with films of 0.2 microns thickness heated well above the melting temperature for a time long enough to relax the polymer, the sample undergo a first quench to a crystallization temperature and then is flooded under water at room temperature. The WAXS (wide angle X-ray scattering) measurement provides an amount of γ-modification content of zero, 7% and 17% for Homopolymer, Raco3 and Raco7 respectively [57].

2.2 Ingot making

A cylindrical polymer ingot with a diameter of 19 mm is prepared by using a stainless steel mold composed of three parts (Figure 1). The lower and middle pieces are screwed together and a plastic O-ring is placed between them to avoid polymer leaks. The polymer sample is placed in the middle piece, which has a small hole for a thermocouple and a vacuum port to minimize bubble inclusion during molding. The top piece closes the mold and allows the application of a slight pressure.

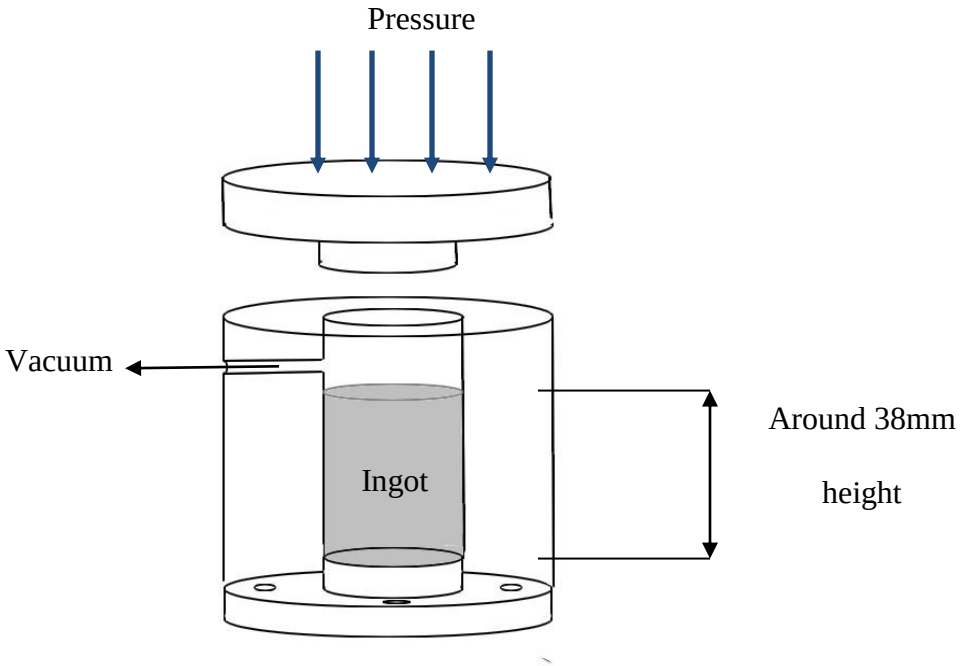

Figure 2.1 Schematic diagram of the ingot mold with dimensions.

The closed mold with polymer sample is placed in a heated platen press (Carver model2699). The polymer pellets are compressed (less than 2 Tons) and then heated slowly from room temperature to 212°C (~50-55 min) while a vacuum is pulled. One hour after heating has started; the mold is taken out of the heated press and allowed to cool to room temperature on a metallic piece while still under vacuum. To remove the ingot, the bottom part of the mold is unscrewed then pushed with a press. Any small leaks are cut with razor blades. The final size of the ingot is approximately 21mm height.

2.3 Flow induced experiments

2.3.1 Apparatus

The shear apparatus (Figure 2.2) is based on Kumaraswamy's rig [37]. Designed to impose a short-term shearing pulse through a thin slit, the apparatus delivers a controlled stress pulse for a determined time and temperature. These types of apparatus are relatively inexpensive to build, simple to operate and in contrast to some types of rheometers, they are able to deliver high levels of shear stress on the polymer [58].They can also be used as a capillary rheometer.

The apparatus is mounted horizontally. The polymer ingots are inserted into a stainless steel reservoir which is strong enough to handle the forces exerted by the piston. The reservoir is maintained at a set temperature of 195°C to keep the polypropylene molten and allows its injection into the front block of the apparatus, which contains a flow cell with a thin slit. During injection, a pneumatic piston hits the back of the reservoir to create a sudden and short pulse. The pressure is controlled by a buffer tank fitted with a gauge.

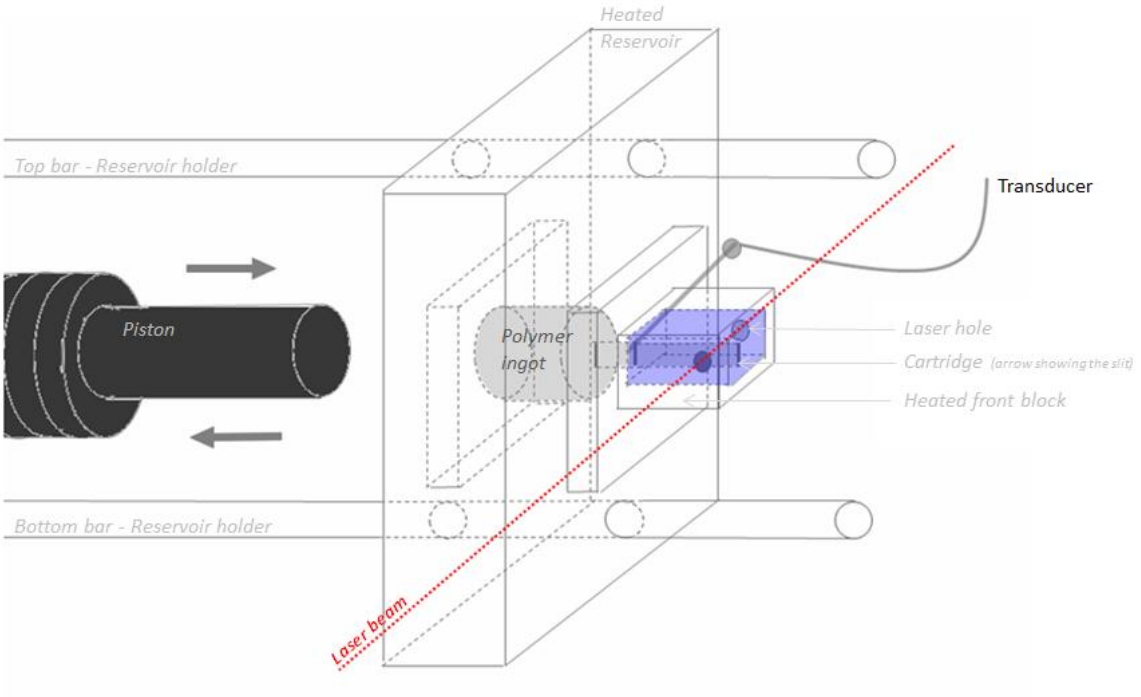

Figure 2.2 Diagram of the shear apparatus.

The flow cell consists of two stainless steel pieces to allow sample removal once the experiment is finished Figure 2.3. The duct of the cell has 63.5 mm length x 6.20mm width x 0.52 mm depth. A sheet of aluminum foil is places between the two cell pieces to facilitate opening of the cell in case of a polymer leak.

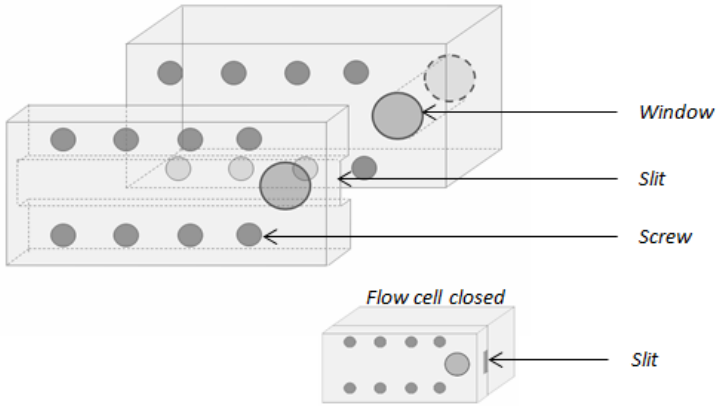

Figure 2.3 Schematic drawings of the flow cell.

The flow cartridge [37] is fitted with flush quartz windows (5.3mm Ø, 1.7mm depth) to allow transmission of the laser beam. The windows are glued on the cartridge with low thermal expansion epoxy resin (Aremco Products, AREMCO-BOND 526N). It was found that the multiple temperature cycling to which the windows were subjected could cause some glue degradation and residual stress birefringence. A specific gluing protocol was worked out to minimize this issue, as follows. Glue is applied on the aperture edge with the lowest possible quantity and the smoothest spread. Windows were carefully inserted and rotated to ensure homogeneous glue coverage. The epoxy was allowed to cure for 2 hours at room temperature, then for 2 hours in a furnace at 93°C. The cell was allowed to cool to room temperature, and then further cured in the furnace at 140°C (i.e. at the isothermal crystallization temperature to be used in flow experiments) for at least 3 days. Finally, the cell was kept at 163°C left for 16 hours to ensure complete curing.

2.3.2 Shearing protocol

The temperature and flow protocol goes as follows. The flow cell is filled and held at T_{erase} = 215°C (above the equilibrium melting point T_{mo} of iPP [Lijima, Marand]) for 5 minutes to erase the polymer history. Then, the flow cell is cooled to the desired crystallization temperature T_{cryst}, 140C. Wet tissues are used to help cool until 148°C is reached. When the isothermal crystallization temperature T_{cryst} is reached, an intense and sudden shearing pulse P_{shear} is applied and the optical signals and pressure are monitored. Note that the isothermal crystallization temperature is chosen such that crystallization under quiescent condition is much slower than the shearing time. Also, it must be

ensured that no significant crystallization occurs during cooling before reaching isothermal conditions.

While the piston course takes only 50ms, the pressure set takes about 0.1 second to be applied and released for the highest pressure, thus, no experiment with a shearing time under 0.5 second has been conducted.

A Labview program was written to control the shearing process and signal acquisition.

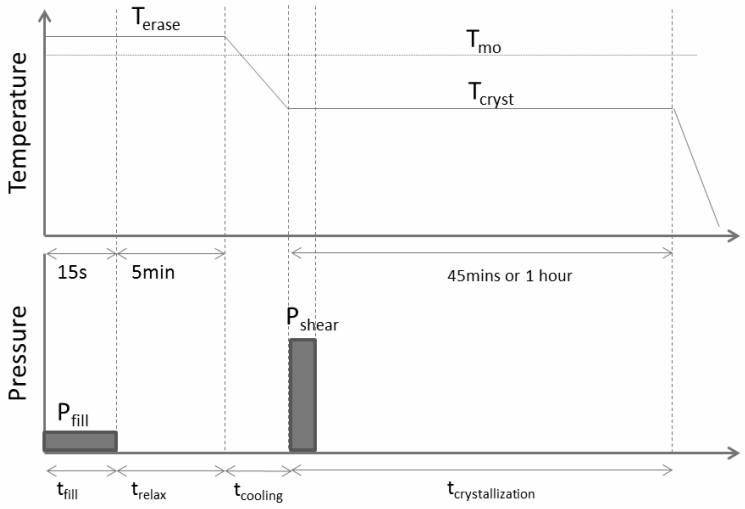

Figure 2.4 Protocol of the flow induced crystallization.

2.3.3 Optical setup

The optical setup (Figure 2.5) consists of a standard arrangement of polarizer, analyzer and detectors. For the purpose of this study, enough information is provided by this arrangement, so the addition of a photoelastic modulator (PEM) is not required.

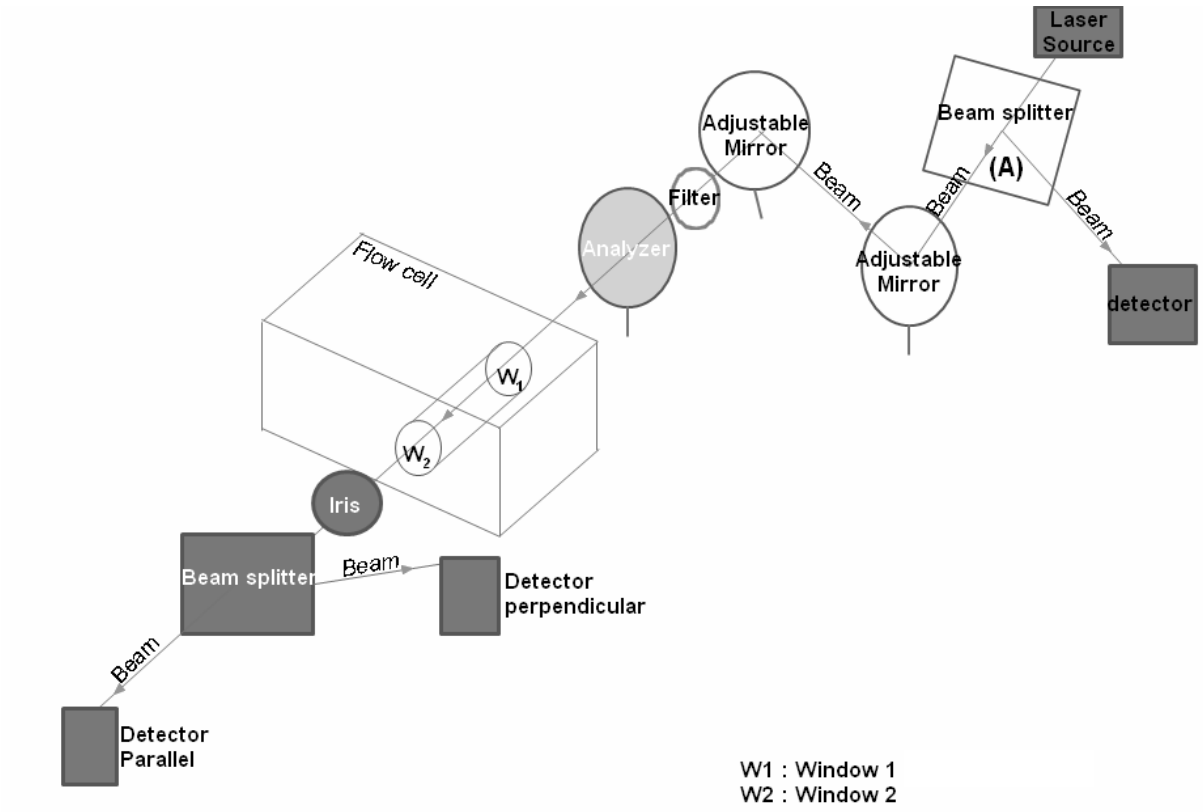

Figure 2.5 Schematic representation of the optical arrangement.

A HeNe laser with a wavelength of 633nm from Thorlabs, Inc was used. The laser beam is oriented horizontally and is first split in a beamsplitter (A) to control the stability of the emitted intensity. Two mirrors are carefully used to align the transmitted beam, and a neutral density filter is used to decrease the intensity and avoid saturation of the detectors. The laser beam traverses a first polarizer oriented at 45° from the direction of flow, then traverses the cell windows perpendicularly, and then goes into a polarizing beamsplitter cube that separates the S and P polarization components (parallel P is transmitted and perpendicular S is reflected) which are captured by amplified Si detectors [Thorlabs PDA55] connected to a computer and recorded with Labview. The beamsplitter is oriented such that the polarizer is oriented at -45° from the flow direction (so the two

polarizers are crossed). The relative orientations of polarizer/analyzer with respect to flow were chosen to result in maximum levels of intensity [59].

2.3.4 Analysis of optical measurements

The turbidity is defined as the ratio of the total intensity at a given time and the total initial intensity (equation 4):

$$T = \frac{I_{\perp} + I_{\parallel}}{I_{\perp 0} + I_{\parallel 0}} \tag{4}$$

Where $I_{\perp}$ the intensity captured from the perpendicular detector (S polarized component from the beam) and $I_{\parallel}$ captured from the parallel detector (P polarized component from the beam). $I_{\perp 0}$ and $I_{\parallel 0}$ are the initial values of $I_{\perp}$ and $I_{\parallel}$ respectively.

The ratio between $I_{\perp}$ and I_{total} ($I_{\text{total}} = I_{\perp} + I_{\parallel}$) can be used to calculate retardation, which is related to birefringence Δn by [60] :

$$\delta' = \frac{2\pi \Delta n d m}{\lambda} \tag{5}$$

where λ is the wavelength of light, and d_m the thickness of the birefringent sample. For the optical setup used in this work, the retardation δ' is determined with the measured parallel and perpendicular intensities $I_{\parallel}$ and $I_{\perp}$ as follows [37] [60]:

$$\delta' = 2 \arcsin \sqrt{\frac{I\perp}{I\perp + I\parallel}} \tag{6}$$

The measured ratio $I_{\perp}$ / I_{total} theoretically varies between 0 and 1, but in reality those values are not reached due to depolarization. For early times, equation (6) is used to calculate retardance. For later times, the maxima and minima from the sinusoidal

signal are computed to the ideal known value of δ' (δ' = π, 2 π, 3 π, etc.). It has been shown that even significant depolarization doesn't affect the accuracy of calculated δ' [61].

Retardance values give a measure of the amount of oriented crystallites that have formed in the sample. Oriented crystallites have birefringence Δn because the refractive index *n*, is higher in the flow direction than perpendicular to it. This can be explained with the backbone of the molecules: if there is no preferred orientation, backbones point in every direction resulting in no net refractive index difference, but if they are oriented in one direction, the light going along the chain direction is more retarded [62].

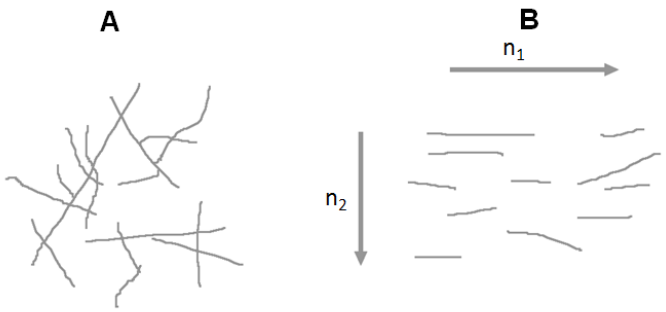

Figure 2.6 Schematic representation of random orientation resulting to no birefringence (A) and orientation with refractive indexes exhibiting birefringence (B).

2.4 Microtoming

After each experiment, the cell is cooled down to room temperature aided by thermal conduction through metal pieces placed underneath and on top of the cartridge. Then the sample is withdrawn for microtoming with an ultramicrotome LKB Ultrotome

III was used with a Diatome 8 mm Histo knife. A simple cut with a razor blade can be effective but requires practice for obtaining satisfactory results.

The region of interest for microtoming is comprised within the window area, which is where measurements are taken during experiments Figure 2.7). To prevent border effects the sample is cut through the center (cut 1 in Figure 2.7) and a second cut (cut 2) is performed to isolate the measured area. The window is ~ 6mm in diameter, so the resulting rectangle must not exceed this dimension. This is convenient as, also the microtome does not allow cuts longer than 8 mm.

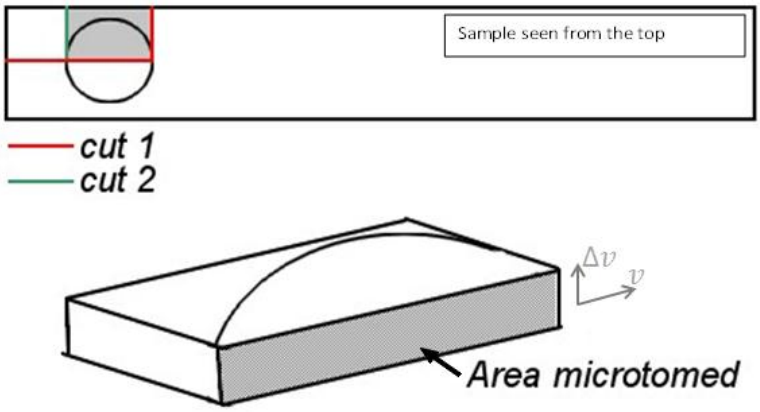

Figure 2.7 Post-preparation of samples before microtome. The circle on the sample represents the area measured by optics and is the area of interest.

Thin sections are microtomed along the flow direction. Some selected samples were also microtomed transversely to flow.

A detailed description of the Ultramicrotome is provided bellow.

Figure 2.8 Detailed pictures of LKB Ultrotome III with the entire unit (top) and the cutting area with knife and specimen installed (bottom).

Figure 2.9 Detailed picture of LKB Ultrotome III control unit for elevation and automation controls of specimen.

Caption Figure 2.8:

A : Optical area based on microscope.

1: Focus, 2: Magnification control.

B : Feeding area

3: Macro feed knob, 4: Micro feed knob.

C : Cutting area

5: Specimen chuck attachment screw, 6: Specimen chuck, 7: Specimen arm, 8: adjustable arc, 9: Specimen head orientation adjustment screw, 10: blade, 11: specimen height adjustment screw, 12: knife trough, 13: Sliding base, 14: knife attachment clamping screw, 15: light.

Caption Figure 2.9:

16: Auto / manual control switch, 17: start switch, 18: specimen elevation control

First, the sample is attached to the specimen chuck while unmounted off the Ultramicrotome unit. The control unit is turned on with the specimen elevation control set at its maximum value. The specimen arm is unlocked (switch located on the other side of the unit, not represented on Figure 2.8) and allowed to reach its maximum height. Then, the chuck is fixed onto the ultramicrotome unit with the long axis of the sample oriented horizontally. The macro feed is turned clockwise (a couple of turns) to ensure that there is space between the knife and the specimen before affixing the knife, in order to prevent any contact with the blade. Then the knife is affixed onto the unit.

At this point, the chuck is manually rotated to have the long axis of the specimen placed vertically. In this way, the shortest dimension of the sample will later become in contact with the edge of the knife while cutting: reducing the surface in contact decreases the strain exerted on the knife and allows for a more even cut [63]. The knife has a trough conceived to receive distilled water to allow sections to move away from the blade and to maintain them in a flat position [63]. However, in this work, the size of the sections is big enough for them to fall by gravity into the trough; therefore, the trough is left dry.

The specimen is brought near the knife edge with the macro feed (the sample is still at the maximum height allowed by the specimen arm). This step requires visual control through the microscope to allow making any necessary adjustments to have the specimen perfectly oriented vertically. Once the sample is near the blade, the inner knob of the macro-feed is slightly turned to bring the specimen over the knife edge. The elevation of the specimen is then changed using the specimen elevation manual control

and a first cut is performed. The specimen elevation is brought back to its maximal value after cut.

This first cut can be repeated until the sample has a flat smooth surface. The manual control has a protection limiting the cutting force which is activated if the thickness of the sample is too large as an excessive cutting force may damage the blade [64]. The knife blade is really sensitive; any damage would result in marks on specimen visible under microscope. If the protection mechanism is activated, the blade must be carefully raised using the specimen elevation manual control and a thinner cut must be attempted by rotating the macrofeed knob. Sections must be thinner than 5 microns.

The outer knob of the macro feed has marks indicating the feed distance but the absolute value of the distance unit is not labeled. This work doesn't require a specific thickness, but it remains constant for every section by always turning the outer knob at 20 units. Several preliminary sections are performed to ensure homogeneity of the cuts. Then some cuts are made without moving the feeding knob, and when no matter is cut the specimen is considered to be ready for cutting and collection of sections. Several sections are cut with different parts of the blade to avoid marks due to knife defects.

2.5 Capillary Rheometry

The slit flow apparatus was used as a capillary rheometer to measuring viscosity. A major advantage of capillary rheometers is the absence of free surface in the test region: for example, the maximum share rate in cone and plate geometries is mostly limited by edge effects [55]. Our setup allows using a shear strain up to 120 [37] and

shear stresses on the order of ~ 0.1MPa shear stress. The pressure transducer has a diaphragm whose deflection provides a measure of pressure, so the slit wall is subject to some irregularities where the probe is located [55]. However, those deflections are relatively small and this effect has been neglected.

For all flow-induced crystallization experiments, the extruded mass was collected right after the shear pulse and the weight was measured and recorded. The volumetric flow rate Q is determined by:

$$Q = \frac{me}{ts \cdot \rho} \tag{7}$$

where h is the slit height, w is the width, t_s is the shearing time, ρ is the density of iPP in the melt (855 kg/m^3) [65], and m_e is the extruded weight of polymer.

Our slit channel has dimensions such that $w >> h$, so the contribution to resistance flow can be neglected as well [55]. First, the apparent shear rate $\dot{\gamma}_A$—defined as the shear rate that would correspond to a liquid with Newtonian behavior—is calculated as:

$$\dot{\gamma}_A = \frac{6Q}{h^2 w} \tag{8}$$

To calculate the true shear rate at the wall $\dot{\gamma}_W$ a correction term is needed. Specifically for rectangular slits, $\dot{\gamma}_W$ is calculated as [55] :

$$\dot{\gamma}_W = \frac{6Q}{h^2 w}\frac{2+\beta}{3} \tag{9}$$

with the correction term β given by

$$\beta = \frac{d[\log(\frac{6Q}{h^2 w})]}{d[\log(\sigma_W)]} \quad . \tag{10}$$

where σ_W is the shear stress at the wall. The slope of the log ($\dot{\gamma}_A$) vs. log (σ_W) provides the value of the n exponent for the model of power-law behavior in a polymer. β is then calculated by :

$$n = 1 / \beta \tag{11}$$

The shear stress at the wall σ_W is calculated from a force balance in the slit:

$$2\sigma_W . A_1 = -\Delta P . A_2 \tag{12}$$

where ΔP the pressure drop, A_1 = w.L (L=80 mm, the distance between the pressure transducer and the exit of the slit) and A_2 is the cross section w.h, so

$$\sigma_W = \frac{-\Delta P . h}{2L} \tag{13}$$

Finally, the viscosity μ ($\dot{\gamma}$) can be determined as:

$$\mu(\dot{\gamma}) = \frac{\sigma_W}{\dot{\gamma}_W} \tag{14}$$

2.6 Depth sectioning of retardation

The "Depth Sectioning method" is a useful tool that allows isolating the stress dependence of flow-induced crystallization of pressure driven duct flows [60]. The local shear stress varies linearly with distance from the wall in pressure driven rectangular duct

flow cell, which means that in-situ measurements that traverse the thickness of the sample correspond to the average of the range of shear stress from the wall to the center of the channel. Depth sectioning consists on taking measurements in real-time at two different wall shear stresses $\sigma_{w,1}$ and $\sigma_{w,2}$ (while keeping all other parameters fixed, i.e., type of polymer, crystallization temperature, shearing time, etc) and subtracting the normalized in-situ measurements of the lowest stress experiment from the highest stress experiment. This subtraction gives the contribution to the real-time measurement that arises solely from the interval of stress between $\sigma_{w,1}$ and $\sigma_{w,2.}$

The depth sectioning procedure is schematically illustrated in Figure 2.10, which shows two experiments that have been performed with different wall shear stresses $\sigma_{w,1}$ and $\sigma_{w,2}$. Due to shear stress linearity throughout the depth of the slit, it can be observed that the experiment performed at $\sigma_{w,2}$ corresponds to the inner part of the experiment performed at the higher $\sigma_{w,1.}$ Therefore, a normalized substraction corresponds to the structure development $\sigma_{w,2}$ and $\sigma_{w,1}$.

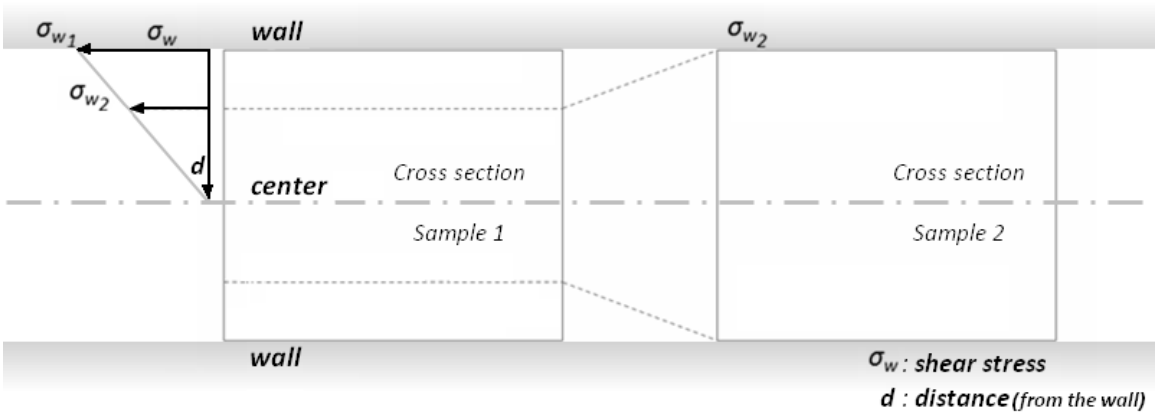

Figure 2.10 **Schematic representation of Ex-situ observation of microstructure after sheared at a given temperature and time. Dash lines show the value of another experiment with same conditions but lower wall shear stress and the range of analyze that the depth sectioning can provide between these two experiments.**

Depth sectioning was applied to the in-situ retardance measurements, which have been described previously in this thesis. For any two experiments performed at $\sigma_{w,1}$ and $\sigma_{w,2}$ resulting in retardances of $\delta_{\sigma w,1}$ and $\delta_{\sigma w,2}$, results are first normalized to the highest wall shear stress used for all experiments $\sigma_{w,max}$:

$$\delta_{n(\sigma w,1)} = \frac{\delta_{(\sigma w,1)} \cdot \sigma_{w,1}}{\sigma_{w,max}} \tag{15}$$

where δn is the rescaled retardation.

The contribution to δ_n due to the structure development arising between the stresses $\sigma_{w,1}$ and $\sigma_{w,2}$ is calculated as:

$$D(_{\sigma w,1\text{-}2}) = \frac{R_{n(\sigma w,1)} - R_{n(\sigma w,2)})}{\sigma_{w,1} - \sigma_{w,2}} \tag{16}$$

Therefore, the result of this equation isolates the signal from a specific slice of sample.

2.7 Optical microscopy

An optical polarized microscope Olympus BX51 was used to determine the depth of appearance of different microstructures and their thickness. From the computed Wall shear stress σ_w defined in equation (13), the shear stress at any distance from the wall was determined from its linear behavior represented in Figure 2.10.

Chapter 3 Discussion and results

3.1 Effect of flow on iPP morphology

3.1.1 Quiescent crystallization of iPP

In order to assess the specific influence of flow on crystallization for iPP, quiescent control tests (where no flow is applied) have been carried out at the same crystallization temperature T_x = 140°C. The thermal history protocol is identical to that used for shearing tests, with the exception that no flow impulse is applied when T_x is reached. In these control experiments, samples were allowed to isothermally crystallize for two different times before quenching to room temperature: 1) for 45 min, which matches the crystallization time of sheared samples before cooling to room temperature (Figure 3.1, top), and 2) for 37 h, which allows the sample to isothermally crystallize to a greater extent (Figure 3.1, bottom).

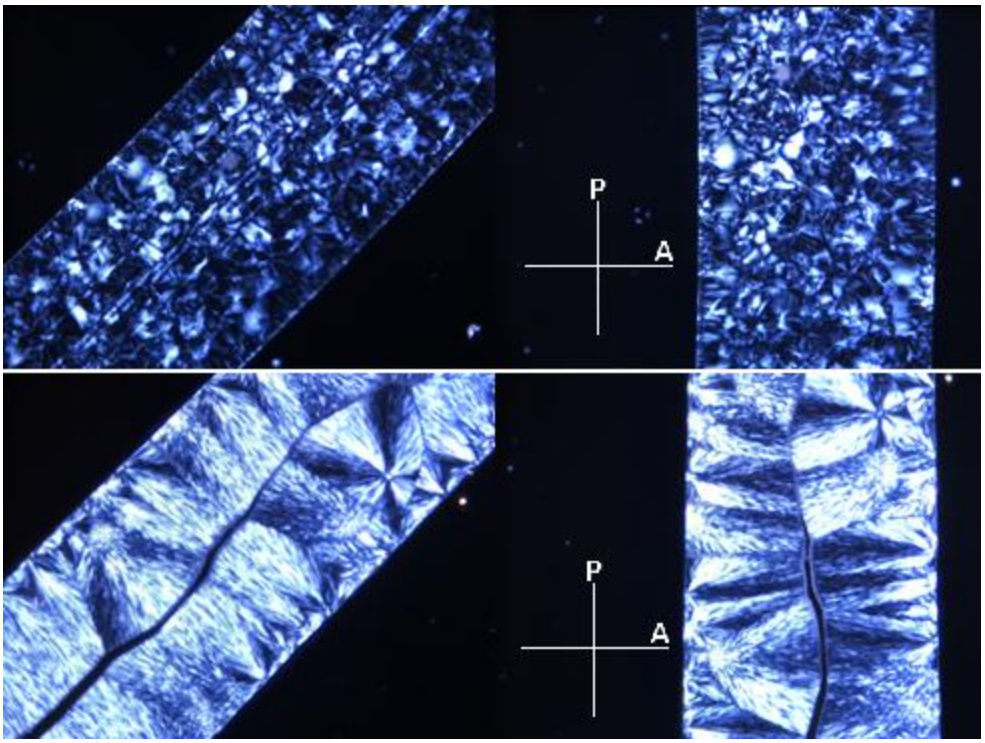

Figure 3.1 Optical polarized micrographs (OPM) of homopolymer crystallized isothermally at 140C for (top) 45 min and (bottom) 37 h 19 min. Afterwards the sample is allowed to cool to room temperature. Polarizer and analyzer are vertical and horizontal, respectively.

The sample quiescently crystallized for 45 min exhibits a spherulitic core with a large number of small spherulites(Figure 3.1, top), while the sample crystallized for 37 h exhibits a much smaller number of big spherulites mainly nucleated near the mold wall (Figure 3.1, bottom). It can be inferred that during crystallization at 140°C, very few nuclei form which translates into large structures. However, when the sample is only allowed to crystallize at 140C for 45 minutes, very little crystallization has occurred isothermally so the core of the sample crystallizes essentially during cooling. Therefore, the resulting spherulites are much smaller because the number of nuclei there that appears increases greatly when temperature is lowered.

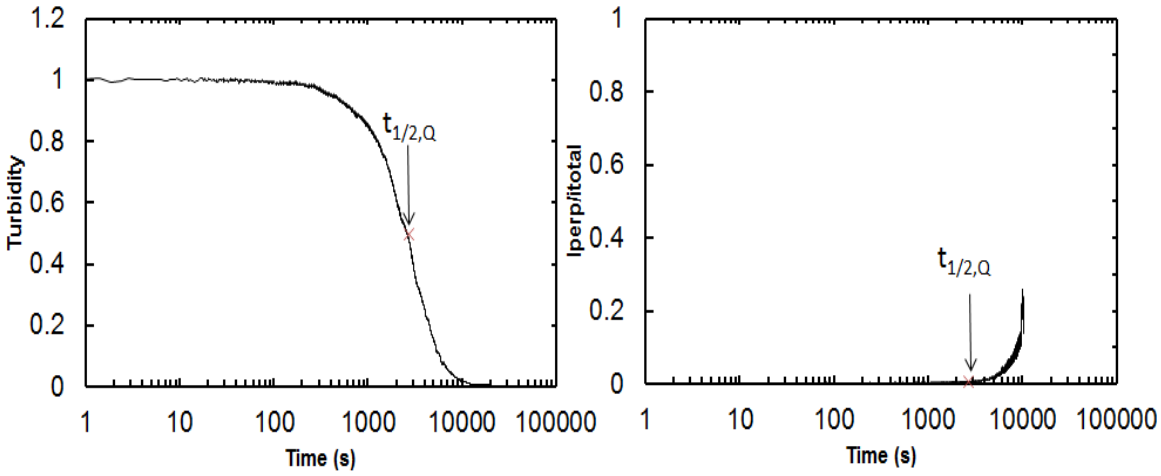

Figure 3.2 **Turbidity and birefringence versus time measured during the long quiescent test. $T_{1/2,Q}$ is the half-time of quiescent turbidity measured at 2719 seconds after shear.**

Turbidity measurements (Figure 3.2, left) qualitatively show that after 45 min, the crystallization process has started (likely near the walls, Figure 3.1, bottom). However, note that turbidity remains constant during the first 10 minutes of isothermal crystallization. Since shear pulses used in flow-experiments are much shorter—of up to 5s, quiescent crystallization is not expected to interfere during flow. Birefringence measurements indicate that no highly oriented structures are formed under quiescent conditions (Figure 3.2, right). The slight increase at later times is attributed to depolarization due to multiple scattering, which appears when samples become very turbid

3.1.2 Enhanced iPP crystallization under flow

Application of flow dramatically changes the morphology, which is observed to be highly dependent on shear stress σ. Figure 3.3 illustrates the types of

morphology that can be encountered for flow-induced crystallization of iPP: oriented skin, skin-lines, fine grained layer and spherulitic core.

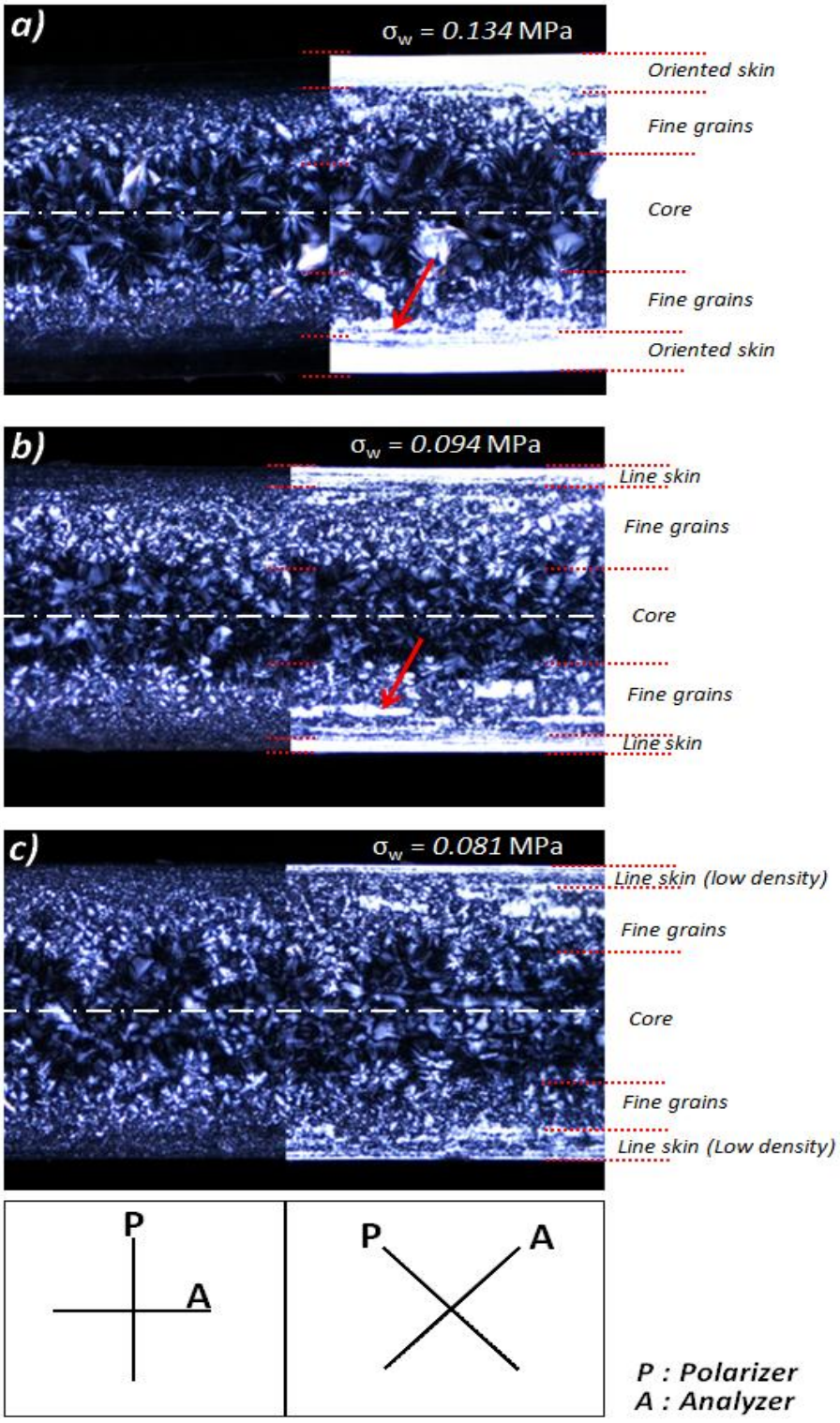

Figure 3.3 **Cross section under optical polarized microscope of iPP subjected to a) σ_w = 0.134 MPa and t_s = 2 s, b) σ_w = 0.094 MPa and t_s = 3 s, c) σ_w = 0.081MPa and t_s = 5 s at Tx = 140°C. Samples were quenched after 45 mins. The red arrow shows an isolated 'sausage-like' structure.**

At high enough stresses, an oriented layer called “skin” can be found, which appears white when oriented at 45 degree with respect to A (Analyzer) and completely dark when oriented parallel (Figure3.3a). Further from the wall, the highly oriented skin doesn’t show a sharp transition between oriented and unoriented structures: instead, oriented ‘sausage like’ structures are present adjacent to the skin (i.e. at lower shear stress, see red arrow in Figure 3.3). When the concentration of sausages is high enough, they appear bright at 45° (similarly to the oriented skin) but a structure is revealed when oriented parallel to A (differently from the skin, which appears completely dark). Such regions of concentrated sausages are denominated “skin-line”. Both the highly oriented skin and the sausage structures have previously been determined to arise from the formation of oriented nuclei (also called thread-like precursors) during flow [24].

At lower levels of stress, a structure mostly constituted of small spherulites is observed and identified as the “fine grained” layer. This structure is absent in quiescent samples, therefore it arises due to the application of flow. The fine-grained layer is a macroscopically isotropic morphology, as it has a similar appearance in micrographs at 0 and 45° to A. The fine grain layer cedes the space at the center of the sample (i.e. at lower stresses) to a core of medium to big spherulites, which are expected to have mostly developed during cooling. The fine grained layer has previously been identified as the result of crystallization from point-like precursors or point-like nuclei created during flow [24], while the core would correspond to regions of the sample that do not experience significant creation of flow-induced precursors (Figure 3.4).

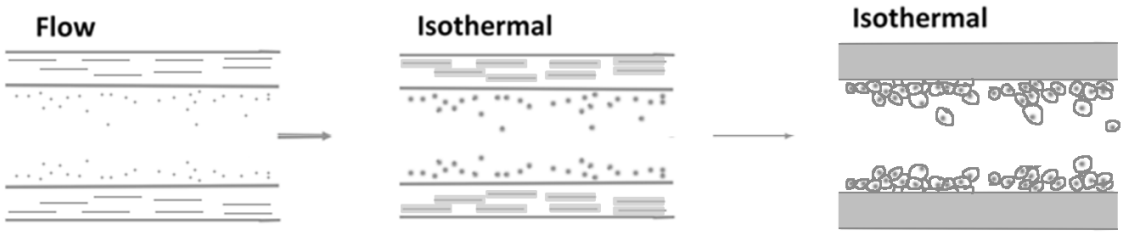

Figure 3.4 **Schematic representation of crystallization of iPP under and after flow during duct flow experiment.**

The flow-induced morphology obtained under different conditions of σ_w and t_s is shown in Figure 3.5, which contains micrographs of sections placed parallel and 45° with respect to the analyzer axis.

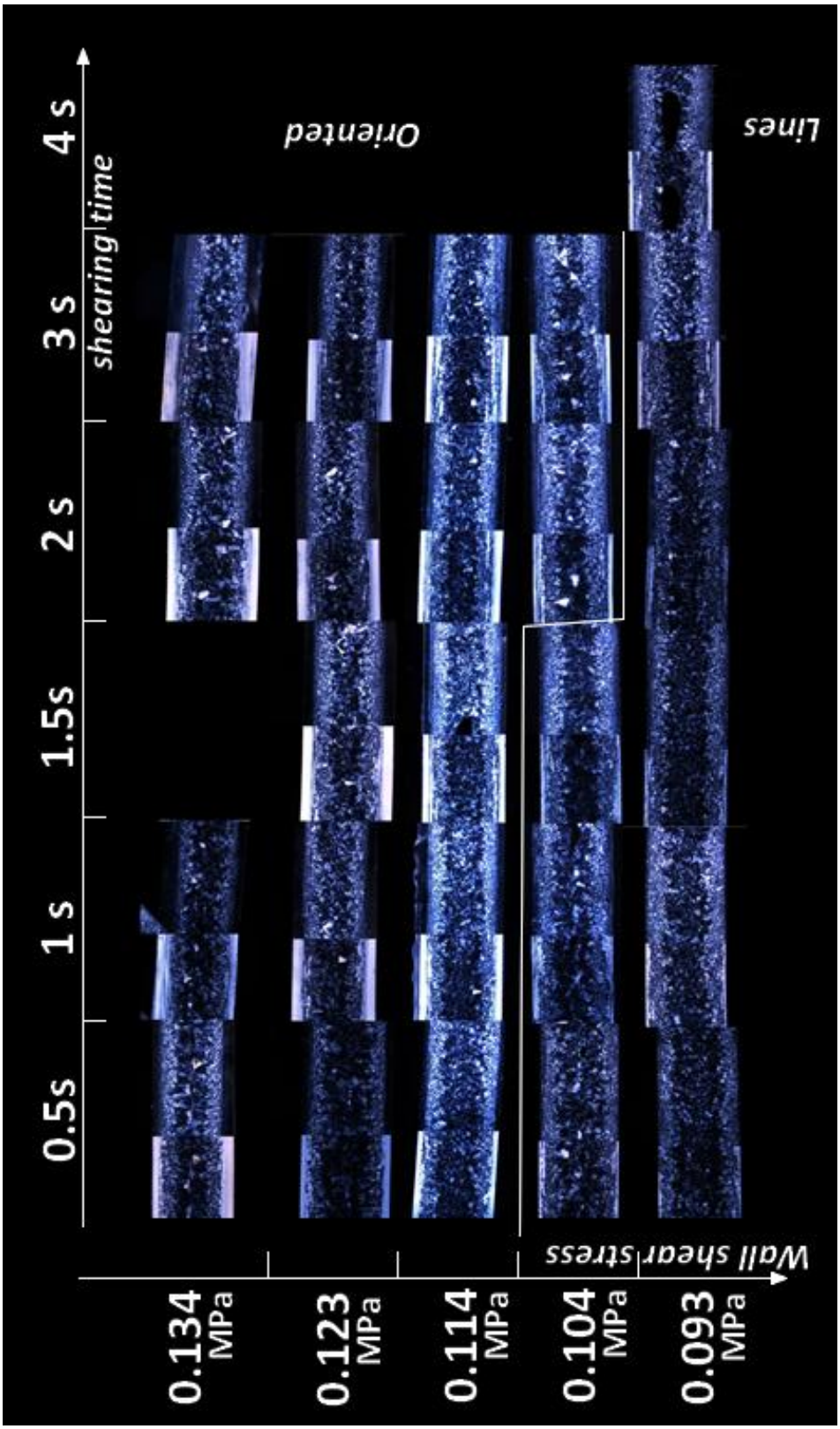

Figure 3.5 Micrographs of samples cuts of iPP ordered by shearing time and shearing stress.

At fixed σ_w, the thickness of the highly oriented skin remains approximately constant for increasing t_s. However, the skin thickness decreases with decreasing σ_w and is absent for the lowest values of σ_w. The oriented line structures are observed to become denser for longer t_s, and typically appear below the highly oriented skin or near the wall when a skin is absent. The fine grain layer is present in all samples examined.

3.1.3 Critical shear stress

The critical shear stress σ_{crit} is defined to be the minimum shear stress required for the appearance of a given type of flow-induced structure. σ_{crit} can be easily computed due to the linear variation of shear stress from the wall to the center of the channel:

$$\sigma_{crit} = \left(1 - \frac{2.\Delta w}{w}\right) . \sigma_w \qquad (17)$$

where Δw is the distance from the mold wall to the largest depth at which the structure appears, w is the thickness of the sample and σ_w is the wall shear stress. σ_{crit} has been determined for skin, lines and grain layers for experiments with different σ_w and t_s (Figure 3.6).

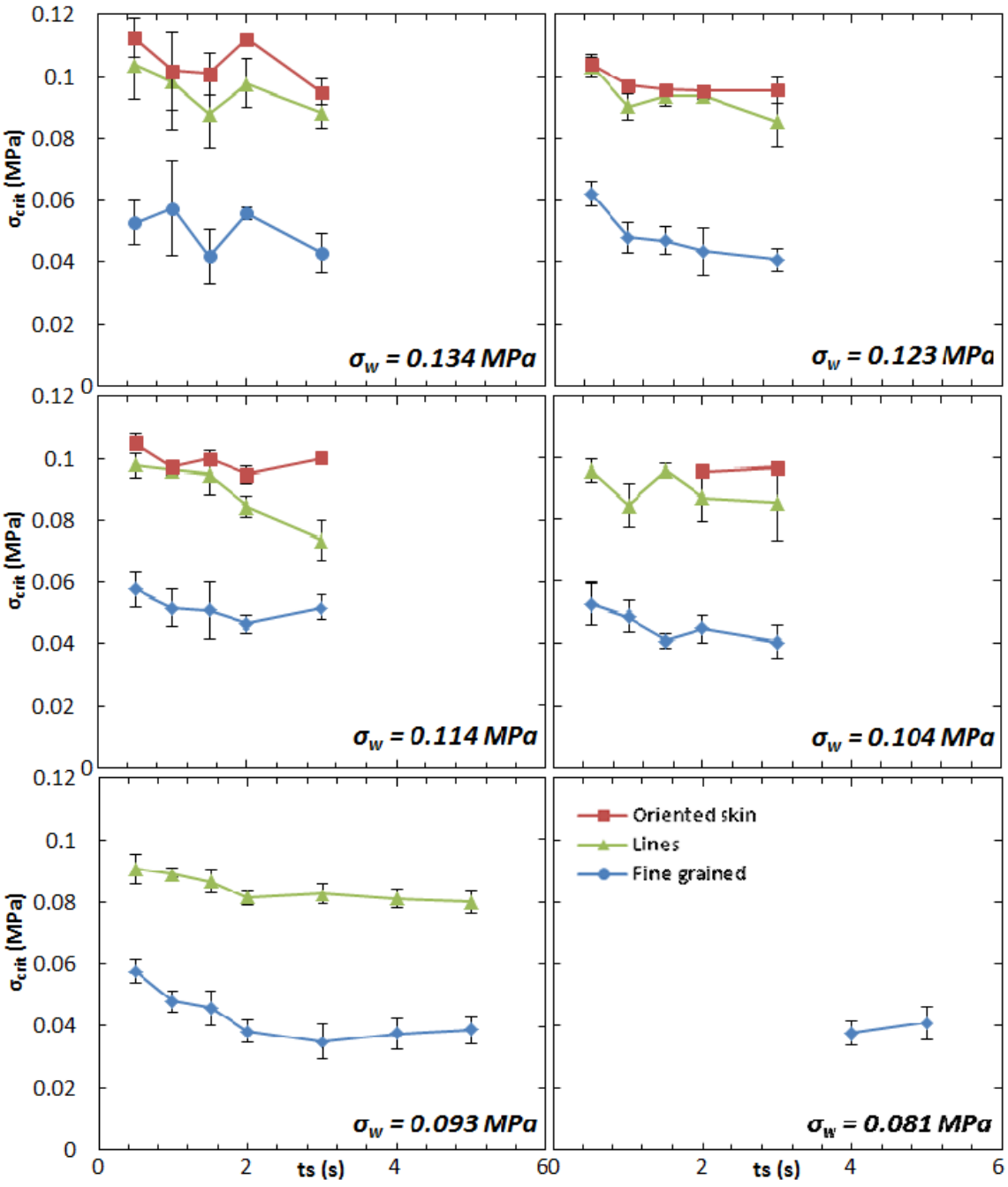

Figure 3.6 Critical shear stress (σ_{crit}) for formation oriented skin (red squares), skin-line (green triangles) and fine-grained layer (blue circles) determined for experiments with different σ and t_s.

The critical shear stress for a highly oriented skin $\sigma_{crit\text{-}skin}$ is slightly decrease with increasing shearing time up to $t_s \sim 1$ s; then $\sigma_{crit\text{-}skin}$ remains at a value of ~ 0.1 MPa with any further increase in t_s (Figure 3.6). The critical stress for oriented lines $\sigma_{crit\text{-}lines}$, is somewhat below that of the oriented skin. The oriented lines sometimes spread on a

large area, but no lines can be observed under 0.8 – 0.7 MPa. Other studies find that there is a direct transition between oriented skin and fine grained layer [37] [66], but in our case this boundary is not as sharp due to the presence of these lines. Finally, the critical stress for the fine grain layer $\sigma_{crit\text{-}fine\text{-}grain}$ follows a similar trend as $\sigma_{crit\text{-}skin}$: it shows a slight decrease with increasing t_s until it plateaus at ~ 0.04 MPa for the longest shearing times.

Figure 3.6 confirms the presence of a threshold shear stress $\sigma_{crit\text{-}skin}$ required to stretch molecules such that formation of oriented precursors is promoted. At the lowest shearing time ts = 0.5 s, molecules have no enough time to get properly stretched so that a higher shear stress is required for formation of shish to occur. For $\sigma_w < 0.093MPa < \sigma_{crit\text{-}skin}$, orientation isn't possible.

3.1.4 Real time optical measurements

The birefringence in-situ measurements allow tracking the development of oriented crystallization in real time at different σ_{crit} and σ_{crit} (Figure 3.7).

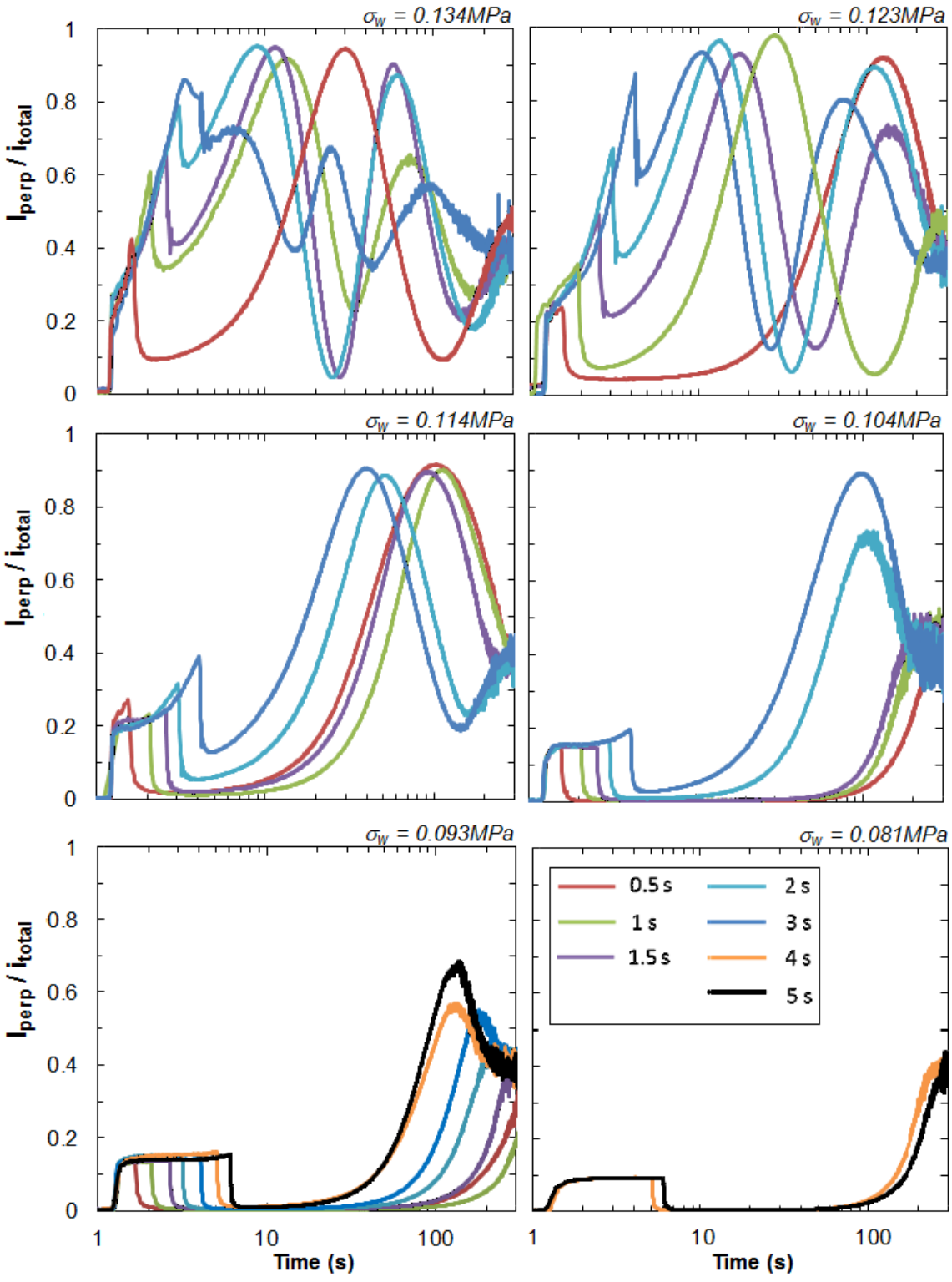

Figure 3.7 Real-time birefringence measurements for different σ_w and t_s.

As an example, a typical birefringence curve for a sample that develops orientation is shown in Figure 3.8, such as the majority of curves in Figure 3.7 corresponding to the three highest levels of σ_w.

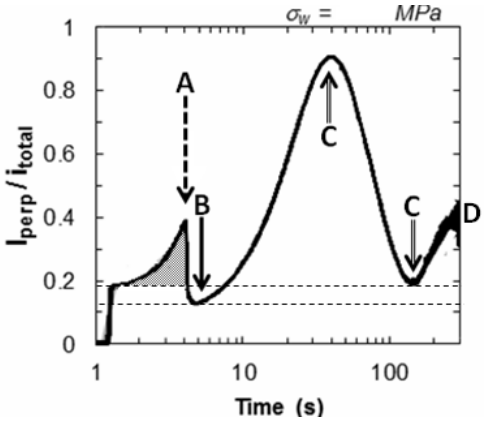

Figure 3.8 Schematic representation of birefringence curve from oriented sample. A: Upturn, B: residual birefringence, C: birefringence going over orders, D: high depolarization. The grey area represents the upturn area.

First, birefringence exhibits a sudden increase during the shear pulse due to orientation of molecules by flow. Note that in our experiments, an initial overshoot in birefringence—which can occur with some materials, particularly with highly polydisperse melts [37]—was not observed. During flow, an upturn (A) was observed when the shear stress was high enough to trigger formation of an oriented structure. When this occurs, this oriented structure does not fully relax after shear and displays residual birefringence after cessation of flow (B). [37] The polymer then undergoes quiescent crystallization, and a sinusoidal curve is measured, which corresponds to the retardance δ going over orders:

$$\frac{I\perp}{I\perp + I\parallel} = [\mathrm{Sin}\,(\frac{\delta'}{2})]^2 \qquad (18)$$

Arrows in Figure 3.8 (C) indicate the number of orders revealed by maxima and minima in measured birefringence. Maxima and minima do not reach their maximum

value of transmission and extinction (1 and 0) because of depolarization [60]. At long times, high levels of depolarization cause measured intensities to go towards a value of ~ 0.5 (D).

In contrast, a specimen that doesn't develop oriented crystallization (Figure 3.7, all curves for σ_w = 0.081 MPa, and experiments at intermediate σ_w's with shortest t_s's) shows no upturn during flow, there is essentially no residual birefringence after cessation of flow, and there is no measurable birefringence during the experiment (although at long times, depolarization due to isotropic crystallization can become high enough for the measured intensity to reach D).

Indeed, by comparing Figure 3.7 and Figure 3.5, experiments with upturns are always followed by peaks and valleys and always provide an oriented skin or a line-skin. The upturn has been shown to arise from the creation of oriented of thread-like precursors during flow [67]. However, for our iPP, growth of kebabs may be contributing to the upturn as well at the highest σ_w and longest t_s. For example, for the highest σ_w = 0.134 MPa and longest t_s = 3 s (Figure 3.7), birefringence goes over orders during the shear pulse, suggesting that oriented lamellae growth is contributing to the signal also. It should be noted that for this particular experiment, a significant drop of the turbidity signal appeared during the shear pulse (Figure 3.10) with a half-time of only 3.5 seconds . Therefore, a significant amount of crystallization may be occurring already during the shear pulse, and could potentially be affecting flow.

In general, upturns become more subtle at lower imposed σ_w and finally are absent for the lowest stress levels. Since the birefringence measurements track the real-

time development of oriented crystallization, the first maxima serves as a measure of the kinetics of oriented crystallization (Figure 3.9). For fixed t_s, a shift of the first maxima to shorter times is observed with increasing σ_w. For fixed σ_w and increasing t_s the time for the first maxima plateaus, suggesting that particularly for the highest levels of σ_w further shearing time does not significantly increase the amount of oriented nuclei from which oriented crystallization occurs. Also, note that the height of the first order maxima are similar for all oriented experiments at a given σ_w, implying that the growth of an oriented layer has no significant impact on transparency.

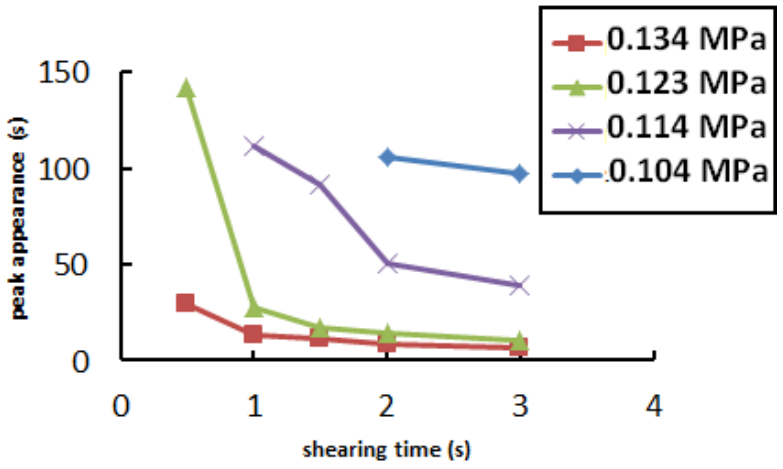

Figure 3.9 Time at which first maxima in Iperp / Itotal occurs for iPP for different σ_w and t_s.

Turbidity provides a qualitative measurement of the kinetics of overall crystallization, as light can be scattered by both oriented and unoriented crystallites. Turbidity measurements (Figure 3.10) show that enhancement of crystallization increases with σ_w. Even for the lower applied σ_w –which do not show oriented crystallization in birefringence or optical micrographs—crystallization remains still accelerated in

comparison with quiescent crystallization (Figure 3.2) because flow strongly improves the formation of point like nuclei [67].

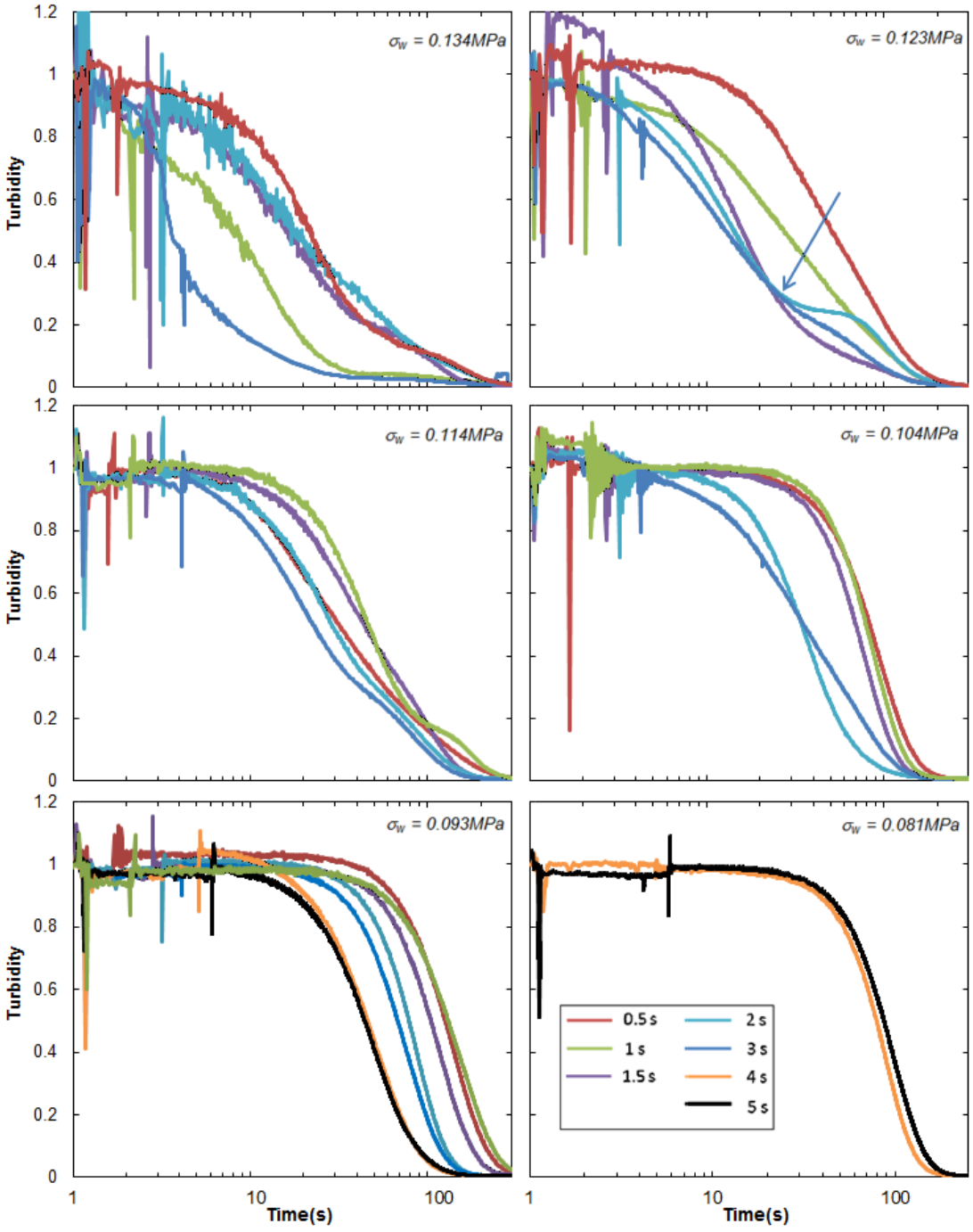

Figure 3.10 Turbidity of iPP of flow-induced experiments at different σ_w and t_s.

For some samples, the turbidity signal manifests plateaus and step-type decrease (some shown by arrow in Figure 3.10). Sometimes the referred plateaus and 2-steps are subtle and difficult to identify or may be absent. The plateaus and steps are always linked to oriented layers, but oriented layers don't always exhibit them. However, they are never found for experiments in which no oriented layers develop. They are thought to arise from impingement between oriented crystallites that grow from oriented nuclei which are very close together. When they impinge, the medium becomes more homogeneous than when it is partially crystallized, and therefore is expected to not scatter the light as much [68].

The extent of qualitative acceleration can be better observed by plotting the crystallization half times $t_{1/2}$ at which the intensity going through the sample becomes 50% of the initial intensity before crystallization (Figure 3.11). Again, for the highest levels of σ_w the effect of t_s plateaus above 1 s of shearing time.

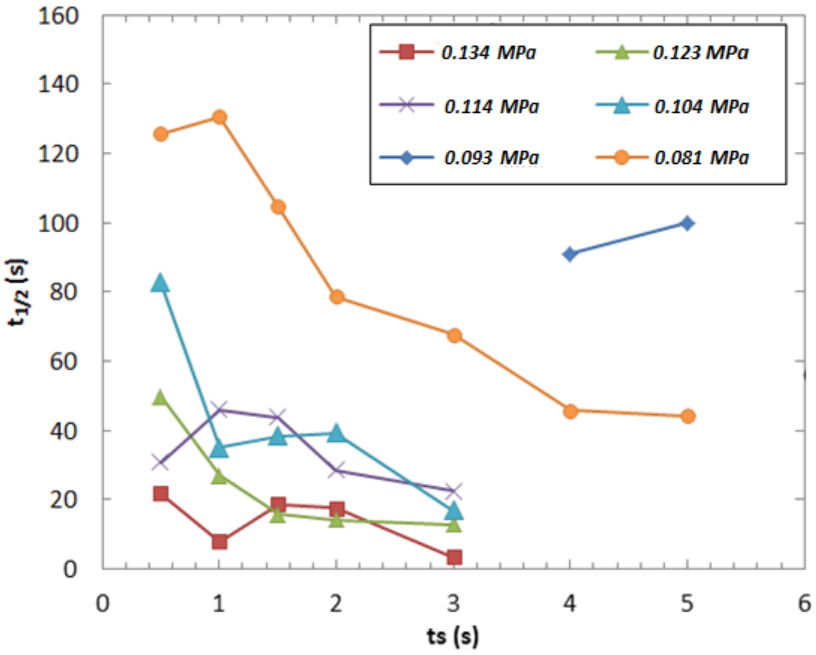

Figure 3.11 Half time versus shearing time for different σ_w.

3.1.5 Retardation

Retardation is calculated using equation (6), and maxima and minima are plotted as explained in section 2.3.3. The computed retardance (Figure 3.12) reveals that a knee and plateau occur for experiments experiencing orientation (ie: experiments with at least one maxima in birefringence); however, such knee and plateau shape are never found for non-oriented samples. This curved shape of retardation would mostly originate from the impingement of kebabs growing off neighboring highly oriented crystallites which affect the overall oriented crystallite growth [60].

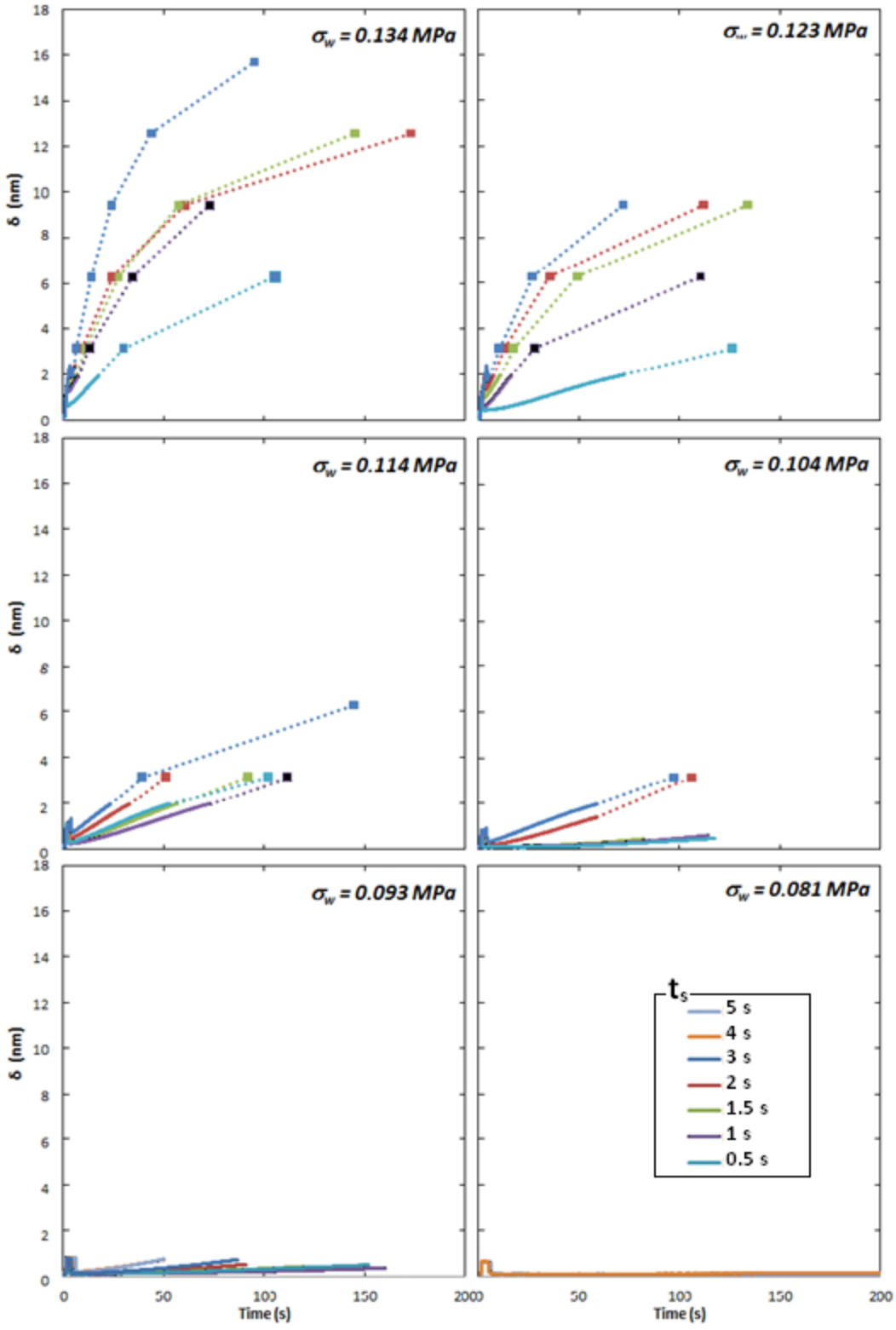

Figure 3.12 Real-time retardation development for iPP.

Figure 3.13 shows an example of retardance during shear flow for σ_w = 0.123 MPa (which has oriented crystallization at all shearing times) and for stress = 0.093 MPa which does not develop orientation. A close look shows that for fixed σ_w and increasing t_s, the retardance during flow matches, as expected. Also, for all experiments which developed orientation and exhibited an upturn, a residual retardance remained after flow, i.e. it did not return to the initial retardance present before flow (~0).

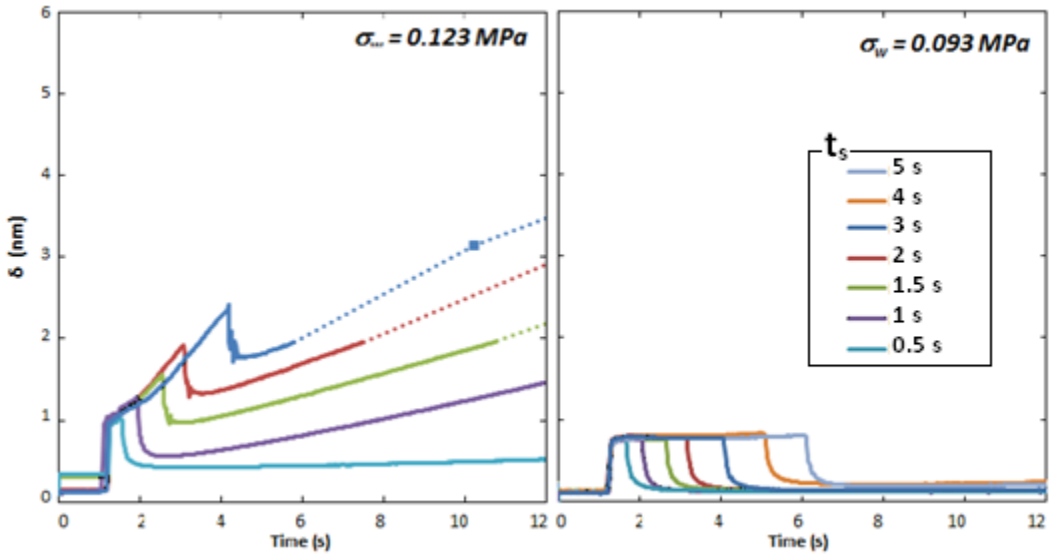

Figure 3.13 Retardation of the inset calculated from birefringence measured experiment for σ_w=0.123MPa (left) and σ_w=0.093MPa (right).

The height difference of upturn (Figure 3.8, gray area) and of residual retardance were computed and plotted for different σ_w and t_s (Figure 3.14). There is an unambiguous correspondence: The higher the upturn, the higher the residual. At higher σ_w, the residual retardance is higher than the upturn and the difference seems to increase with increasing σ_w and t_s, that is, the difference is larger for samples that develop more oriented crystallization. This observation suggests that, if a large amount of oriented nuclei is created during flow and the radial growth velocity of kebabs is high enough, a large quantity of oriented crystallites may be created already during and right after the shear

pulse which contributes significantly to the retardance. This phenomenon was observed for iPP at t_s = 3 s and σ_w = 0.134 MPa, for which previous measurements suggest that significant amounts of crystallization occur during the shear pulse (see Figure 3.10),

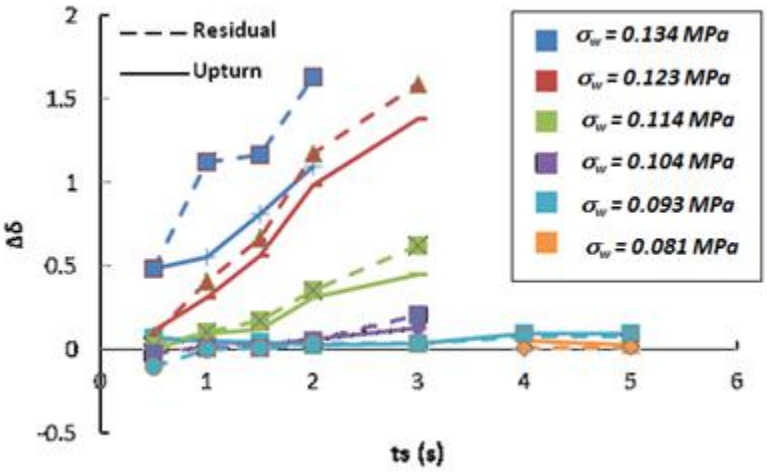

Figure 3.14 Comparison between upturn (line) and residual (dashed line) retardance at given σ_w and ts.

Oriented precursors form during flow if stresses and ts high enough, but after cessation of flow, no more oriented nuclei length is created [52] [29] hence, the initial slope of retardation right after cessation of flow arises from the growth rate of kebabs on the oriented precursors. Therefore, this initial slope of retardance should be proportional to the amount of shish [60]. The initial slopes of retardation after cessation of flow are shown in Figure 3.14. Again, the amount of σ_w is a determinant parameter. However, at high σ_w some saturation occurs with increasing t_s, as manifested by the curvatures in Figure 3.15. The influence of t_s remains minor for $t_s \geq 1$ s, while the increase of total length of oriented precursors between t_s of 0.5 s and 1 s is drastic.

One has to keep in mind that the shearing time t_s impacts the size of shish created, and longer t_s leads to longer shish formation. Hence, although t_s has to be relatively short

for short-term shearing type of experiments, t_s also needs to be long enough to expect a sufficient growth of shish due to molecules that have reached a critical condition of stretch [67]. This may explain the differences in behavior between experiments with t_s = 0.5 s and experiments with $t_s \geq 1$ s.

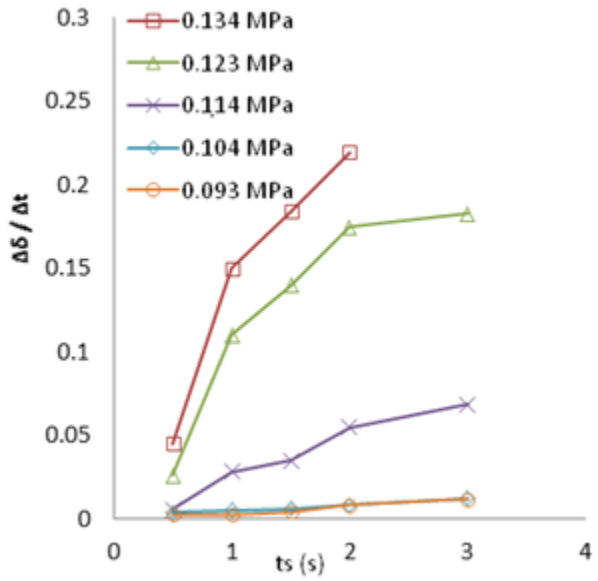

Figure 3.15 Slope of initial retardation right after cessation of flow versus t_s.

3.2 Effect of ethylene content (Raco3 and Raco7)

To examine the effect of comonomer content on flow-induced crystallization, experiments with the same conditions have been performed for random copolymers with 3.4 and 7.3 % mol of etheylene, respectively named Raco3 and Raco7.

3.2.1 Effect of ethylene comonomer on morphology

As expected, Raco3 and Raco7 required a significantly longer time of crystallization under quiescent conditions than iPP to become completely turbid: ~70 and

~ 77 h for Raco3 and Raco7, respectively, compared to ~ 37 hour for iPP (Figure 3.16 top and middle). These experiments are called 'long quiescent'. Their quiescent half time $t_{1/2,Q}$ is represented in Table 2.1 for both grades of copolymers which occurs about 30 times later than the homopolymer.

Table 3.1 Turbidity half times $t_{1/2,Q}$ under quiescent crystallization.

Grade	$t_{1/2,Q}$
iPP	2770 s
Raco3	77710 s
Raco7	81920 s

Similarly to iPP, shorter quiescent tests have been performed for both Raco3 and Raco7 which match the experimental length of their flow induced crystallization experiments, i.e. 1 hour of isothermal crystallization (Figure 3.16 top).

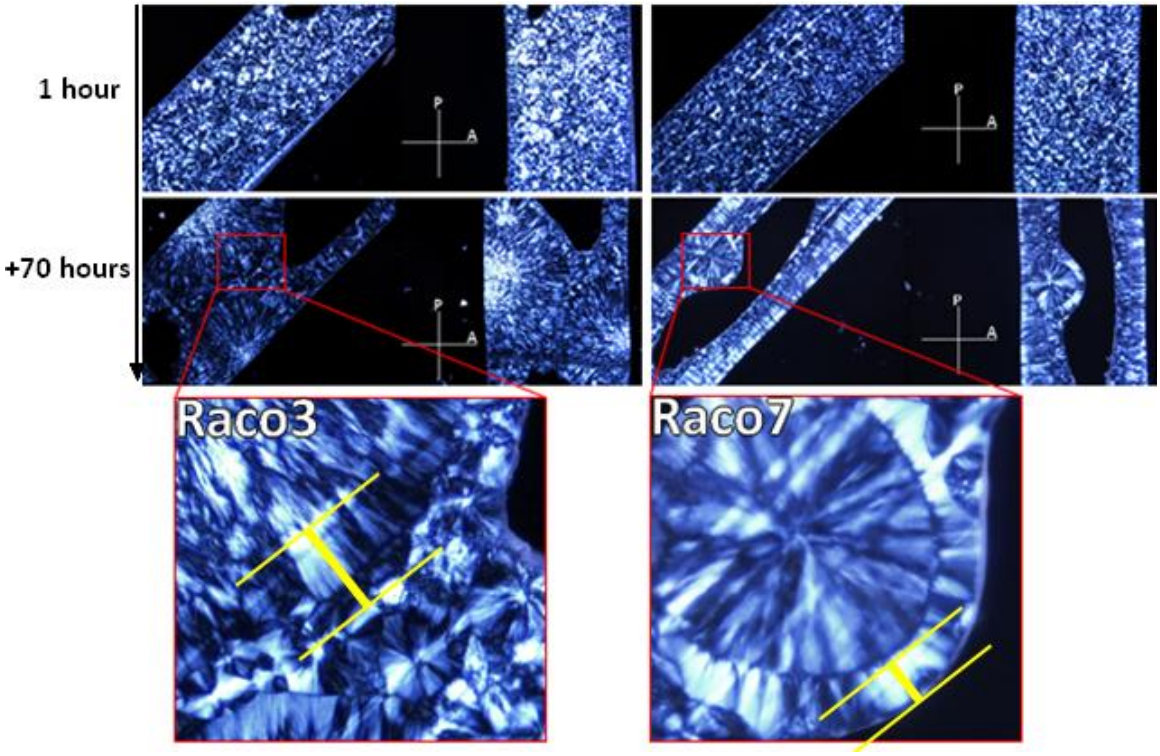

Figure 3.16 Optical polarized micrographs of Raco3 (Left side) and Raco7 (right side) quiescently crystallized during 1 hour (top), ~ 70 h (medium left) and ~77 h (medium right). Yellow lines indicate the structure grown during cooling.

Both grades exhibit a dense spherulitic core with small dimensions after 1 hour of isothermal crystallization before cool down. Some growth from the mold wall has occurred and represents about 7% of the samples width. For the "long" quiescent experiments, very large spherulites are present while the regions in between exhibit much smaller spherulites (See appendix for a detailed pictures of "long" quiescent experiment). At 140°C, the ethylene based copolymers have very low nucleation, so big spherulites originate under isothermal condition while the areas of small spherulites originate during cooling. A change of the morphology of these big spherulites near the border (yellow lines on Figure 3.16 bottom) results from spherulitic growth when cooling is first started and T is not low enough to create large amounts of nuclei. This is the same morphology displayed near the wall mold of the 1 hour quiescent experiments, denoting the non-

isothermal origin of this weakly-oriented layer. The linear growth rate for Raco7 is lower than for Raco3 due to the higher amount of ethylene content [56] while the short quiescent experiments for all three grades of polymer display a spherulitic core, the size of these spherulites is bigger for iPP. Due to the higher growth rate for iPP, upon cooling, the free space is filled up faster from spherulites nucleated under quiescent. The growth is enhanced with the decrease of temperature of the medium resulting to bigger spherulites at the expense of the nucleation. This growth being lower for copolymer, the nucleation is less troubled; more spherulites nucleate and quickly impinge resulting to smaller sizes.

3.2.2 Effect of flow on copolymer crystallization

As for iPP, the morphology is strongly affected by flow. Some types of morphology are the same as for iPP, while some other differ (see nomenclature in Figure 3.17 Nomenclature of the different morphology encountered during short term shearing for Raco samples.). While flow can also create a highly oriented skin for Raco3 and Raco7 (Figure 3.17 Nomenclature of the different morphology encountered during short term shearing for Raco samples., A), the transition between oriented skin and the core of the sample is sharp and does not show lines or sausage-like oriented structures as it did for iPP. However, lines or skin-lines are found in some samples which do not exhibit a highly oriented skin (Figure 0.10 in Appendix, Raco3 : σ_w = 0.114MPa t_s = 0.5s, σ_w = 0.104MPa 0.5s $\leq t_s \leq$ 1.5s; Figure 0.11 in Appendix Raco7 : σ_w = 0.123MPa t_s = 0.5s, σ_w = 0.104MPa 1s $\leq t_s \leq$ 1.5s) Also, for most specimens, the fine-grained layer observed on iPP cannot been distinguished on copolymers which, nevertheless, doesn't preclude its existence. A fine-grained layer can only be noticed for some experiments at the lower

levels of σ_w, particularly at the longest t_s (Figure 0.10, Raco3 : σ_w = 0.093MPa $t_s \geq 2s$; Figure 0.11 Raco7 : σ_w = 0.093MPa $t_s \geq 2s$, in Appendix). Possibly, the larger size of spherulites in the core of iPP samples facilitates the observation of this fine-grained layer, while the smaller spherulite size for the core of the RACO's may hinder the differentiation between the core and a fine-grained layer. Finally, a microstructure denominated 'black layer' has been found in some samples (Figure 3.17 D, and Figure 0.10, Raco3 : σ_w = 0.093MPa $t_s \leq 1s$; Figure 0.11 Raco7 : σ_w = 0.093MPa and 0.104MPa $t_s \leq 1s$) which grew perpendicular to flow and which surprisingly appears dark under crossed polars at 45° and bright when parallel (opposite to the appearance of the highly oriented skin). It always grows from an oriented line structure present near the mold wall. However, that oriented border line can appear without necessarily developing a black layer and has been called 'frame line' or 'border line'.

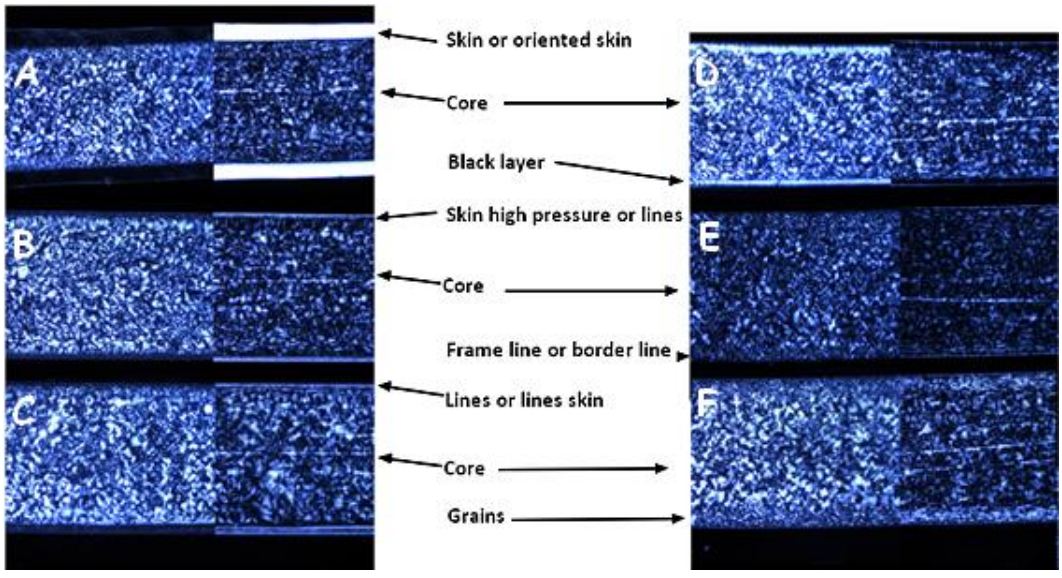

Figure 3.17 Nomenclature of the different morphology encountered during short term shearing for Raco samples. With Raco7: A) σ_w = 0.134MPa t_s = 2s, B) σ_w = 0.123MPa t_s = 0.5s, C) σ_w = 0.104MPa t_s = 1.5s, D) σ_w = 0.093MPa t_s = 0.5s, E) σ_w = 0.093MPa t_s = 2s, F) σ_w = 0.093MPa t_s = 5s.

3.2.3 Effect of ethylene comonomer on critical shear stress

The same range of σ_w and t_s as for iPP was imposed on the two copolymers (Figure 0.10 and Figure 0.11 in Appendix), and the critical shear stress for the highly oriented skin $\sigma_{crit\text{-}skin}$, the line-skin $\sigma_{crit\text{-}line}$, and the fine-grained layers $\sigma_{crit\text{-}fine\text{-}grain}$ was calculated (Figure 0.2 and Figure 0.3 in Appendix). The average of $\sigma_{crit\text{-}skin}$ obtained at different σ_w is compared for the three polymer grades (Figure 3.18). As with the iPP homopolymer, at a given shearing time t_s, the value of $\sigma_{crit\text{-}skin}$ matches for all σ_w applied to each polymer grade. Interestingly, iPP and Raco3 have similar $\sigma_{crit\text{-}skin}$, while Raco7 is clearly higher for $t_s \geq 1$ s. The $\sigma_{crit\text{-}skin}$ has a larger value for $t_s = 0.5$ s which matches for all three grades. When ts is increased to 1 s and above, $\sigma_{crit\text{-}skin}$ quickly decreases and plateaus to ~ 0.100 MPa for iPP and Raco3 and ~ 0.105 MPa for Raco7. The influence of ethylene on $\sigma_{crit\text{-}skin}$, hence, is only observed for $t_s \geq 1$ s.

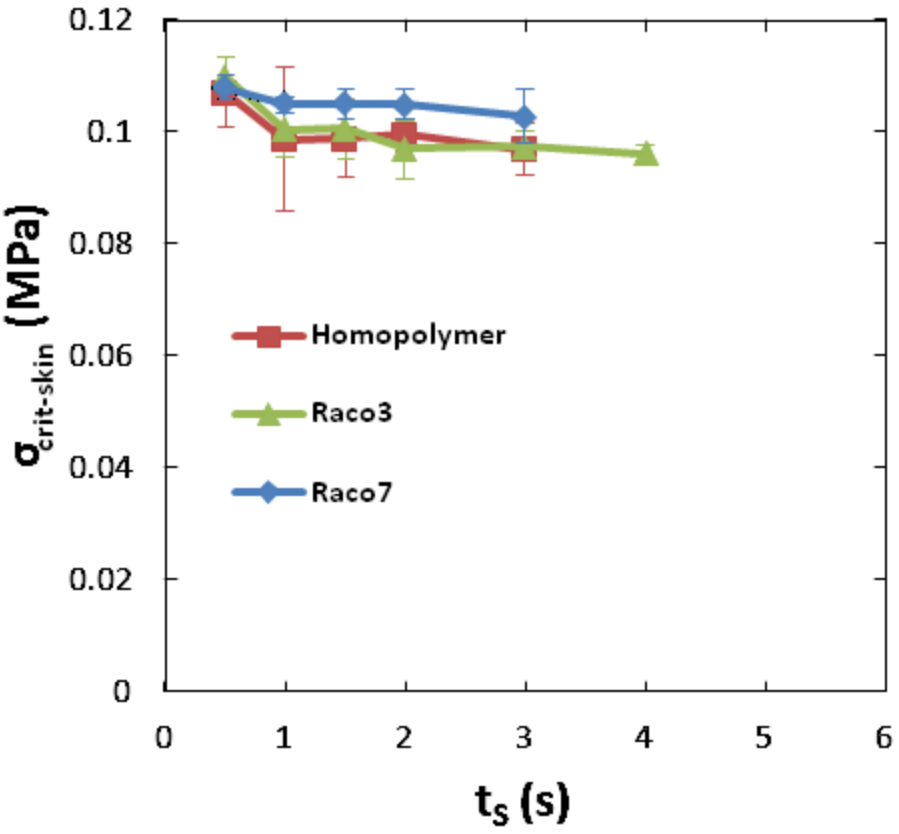

Figure 3.18 averaged $\sigma_{crit\text{-}skin}$ for iPP, Raco3 and Raco7 at different ts.

It is interesting to note that for raco3 at σ_w = 0.104 MPa Figure 0.10, there is a line-skin for the three shortest shearing times and, once t_s reaches 2s, a highly oriented skin with the same thickness appears. This may be explained as follows: For a given high σ_w (> $\sigma_{crit\text{-}skin}$) the strain is high enough to promote the growth of shish during flow [52]. This results into a line-skin because the strain is not high enough to create a sufficiently dense formation of shish which would result in a highly-oriented skin layer. This explains why the lined-skin tends to occur mostly at very short ts or at low σ_w.

3.2.4 Critical specific work

A number of authors argue that the amount of applied specific work is a critical parameter controlling flow-induced crystallization [30], [26], [44]. Specific work W and rate of specific work $\dot{W}$ are defined as:

$$W = \sigma_{.}\dot{\gamma}.\ t_s \tag{19}$$

$$\dot{W} = \sigma_{..}\dot{\gamma} \tag{20}$$

Where t_s is the shear stress and $_{.}\dot{\gamma}$ is the shear rate. If the value of wall shear stress σ_w is used, then the rate of work and specific work at the wall $\dot{W}_w$ and W_w can be calculated, respectively.

A fixed σ_w means that the rate of specific work $\dot{W}_w$ is constant. Therefore, each row in Figure 3.5, Figure 0.10 and Figure 0.11 (in appendix) correspond to fixed $\dot{W}_w$. It can be noted that at a given $\dot{W}_w$, increasing ts over 1 s does not result on a thicker highly oriented skin; hence, the increase of specific work W_w has no influence on the thickness of oriented layers and on the critical shear stress to form an oriented skin $\sigma_{crit\text{-}skin}$.

The specific work at the wall W_w is represented against the wall shear stress σ_w in Figure 3.19 for all three grades, and the plateau critical stress for formation of skin $\sigma_{crit\text{-}plateau}$ (section 3.2.3) has been represented by a vertical line. Below the plateau critical shear stress for highly oriented skin $\sigma_{crit\text{-}plateau}$, no orientation can occur at any specific work W_w. When $\sigma_w > \sigma_{crit\text{-}plateau}$, one can observe that above a certain value of W, orientation is always obtained. This value of work has been denominated as “specific

work threshold" and is represented by a dashed horizontal line. According to Figure 3.19, the effect of ethylene content on the threshold specific work is minimal.

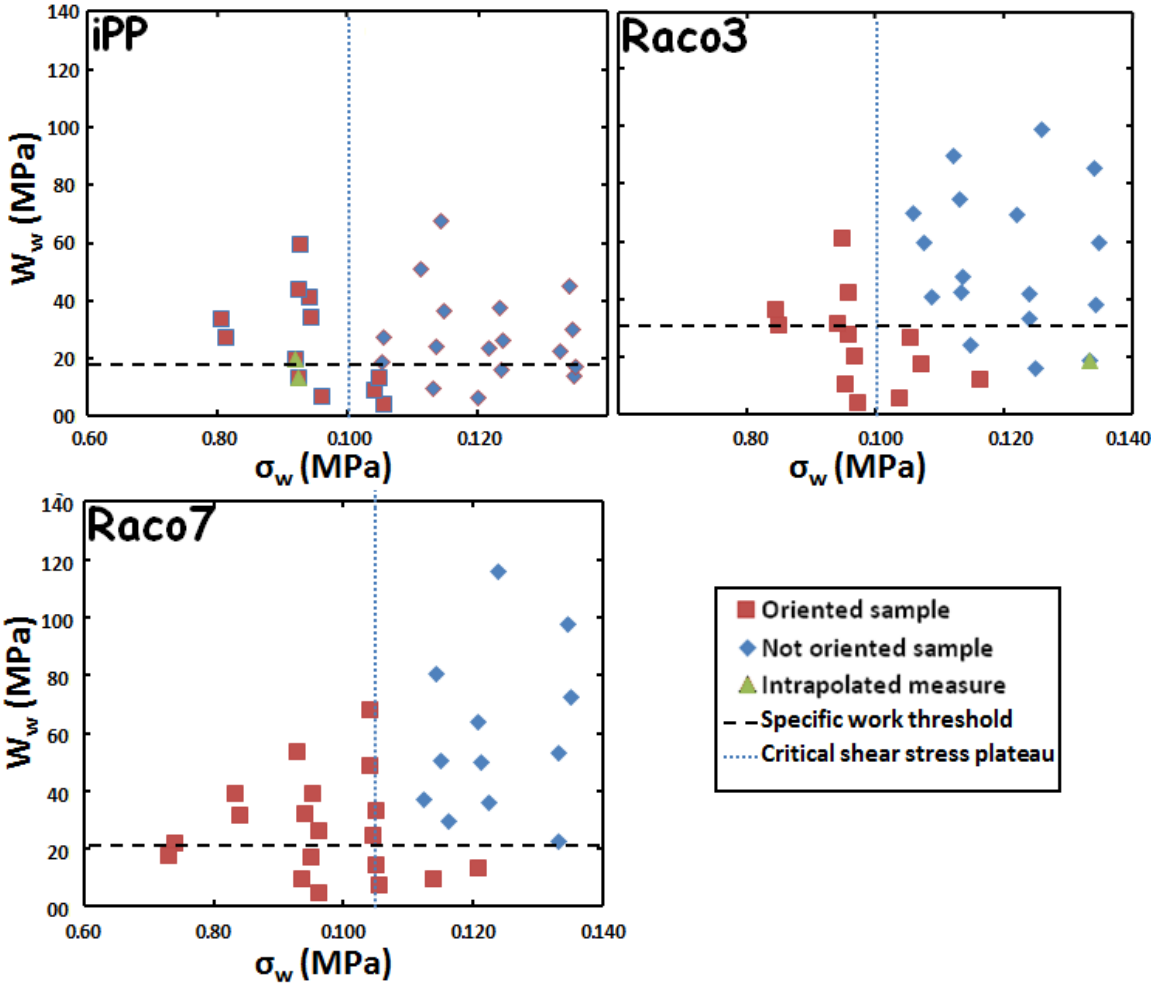

Figure 3.19 Specific work at the wall W_w versus wall shear stress σ_w. The plateau critical shear stresses $\sigma_{crit\text{-}plateau}$ from Figure 3.18 are represented by a dashed vertical line, and the specific work threshold is represented by a horizontal dashed line.

Above $\sigma_{crit\text{-}plateau}$ but below the specific work threshold, both oriented and unoriented samples are obtained (mixed region, bottom right quadrant in each plot of Figure 3.19). The results in this mixed area indicate that above $\sigma_{crit\text{-}plateau}$, an increase of the wall shear stress σ_w results in a decrease of the threshold specific work required for orientation. Unfortunately, it was not possible to obtain more data for the mixed area at

very low W_w and high wall shear stress σ_w due to experimental limitations related to using extremely short shearing times and to uncertainty when measuring very small extruded polymer weights (needed to calculate shear rate, see section 2.5).

3.2.5 Effect of ethylene content on kinetic

Measurements show that the kinetics of flow-induced crystallization become significantly slower for fixed conditions when increasing the ethylene content (Figure 3.20, complete set of birefringence curves is given in Figure 0.4 and Figure 0.5). Slower kinetics was particularly expected because of the known decrease of linear growth rate with increasing of ethylene content [56]. The overall kinetics of crystallization and oriented crystallization are measured with the turbidity and birefringence. However, it is not possible to elucidate the effect of ethylene on the formation of oriented nuclei at particular flow conditions because turbidity and birefringence combine both effect of nucleation and growth.

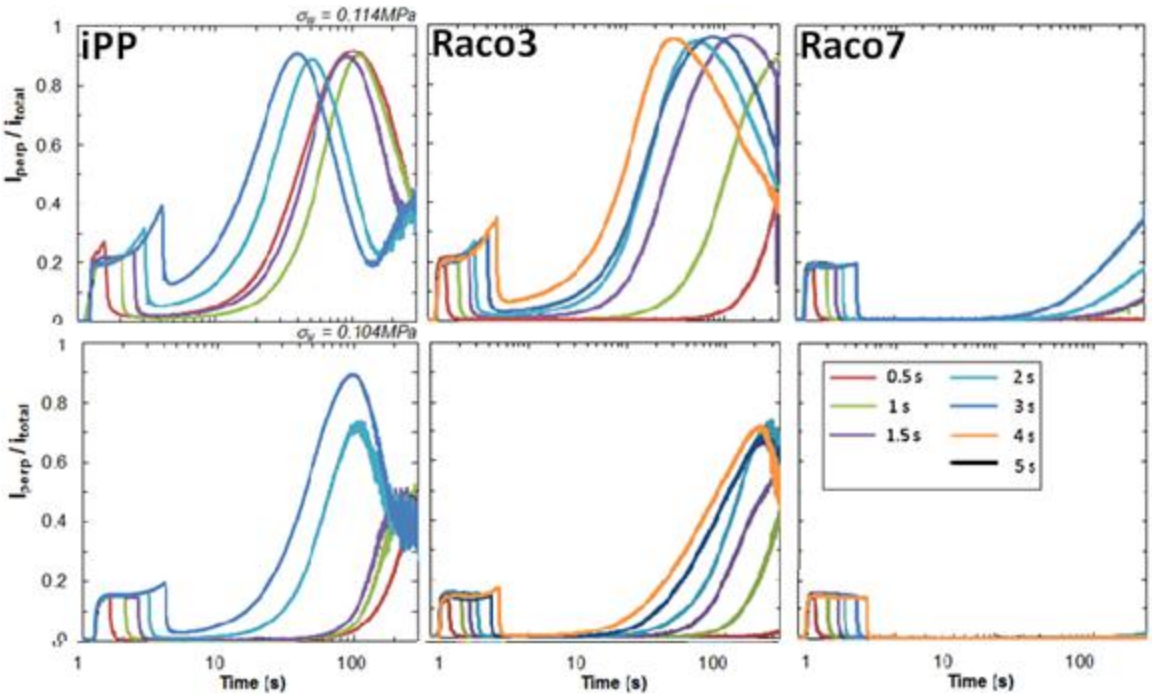

Figure 3.20. Birefringence comparison between iPP, Raco3 and Raco7 at selected wall shear stress of 0.114 MPa and 0.104MPa.

Highly oriented layers were found for all three polymers grades (Figure 3.20, first row) at and all ts (except ts = 0.5 s for raco7). Real-time birefringence for σ_w = 0.114 MPa (Figure 3.20 top row) shows that increasing ethylene content lengthens the time for peak appearance. For Raco7, the lengthening is such that the peak appearance is delayed to times longer than the experiment one (1 hour). The bottom row in Figure 3.20, is representative of a change in morphology since no oriented skin is observed for Raco7 at σw = 0.104 MPa while both iPP and Raco develop a highly oriented layer for the longest shearing times.

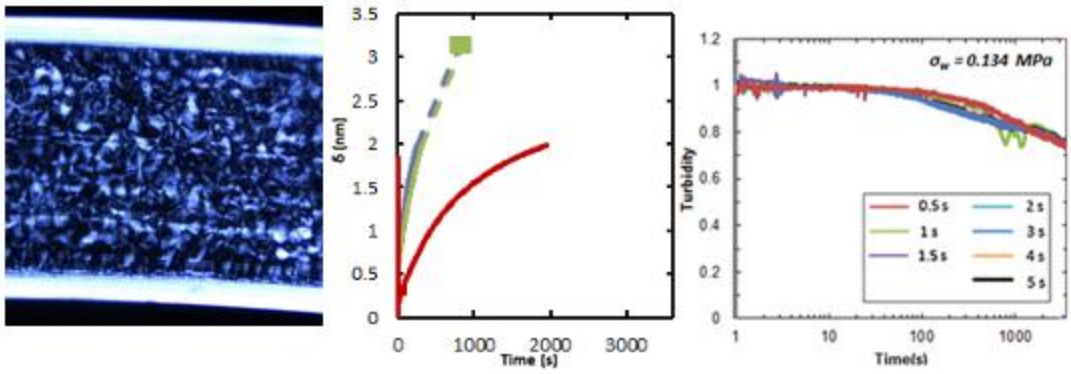

Figure 3.21 Micrograph (left), retardance (middle) and turbidity (right) of Raco7 exhibiting an highly oriented skin for every ts

It is interesting to note that for Raco7, the turbidity is very low during the 1 h measurement even for samples that develop a highly oriented skin, indicating a minimal effect of skin on the turbidity at this stage. For example, under σ_w = 0.134 MPa all shearing times result in a highly oriented skin (ts = 0.5 s shown in Figure 3.21 left, all ts shown in Figure 0.11 in appendix). Furthermore, the curvature of retardance (Figure 3.21, middle) manifests that impingement of kebabs growing off threadlike precursors occurs at ~ 500 s of isothermal crystallization, so the skin region has already crystallized to a significant extent. Despite this, the turbidity remains low and for almost all Raco7 samples, the duration of an isothermal crystallization (1 hour) was not long enough to measure the turbidity half-time.

For some Raco3 and Raco7 subjected to low σ_w that does not promote oriented crystallization, the birefringence displays a subtle decrease during flow (Figure 0.5 σw = 0.104 and 0.093MPa). This may be due to the presence of an overshoot in the beginning of the shear pulse [30]). The absence of this phenomena for iPP may be the presence of lines, sausages, fine-grained layer that may be already crystallizing during flow due to the higher linear growth rate at 140C.

3.2.6 Effect of ethylene on real-time retardance

Similarly to iPP, the retardance for Raco3 and Raco7 shows a knee and slowdown in rate of change (Figure 0.8, Figure 0.9) for samples that develop a highly oriented skin, signifying that impingement of kebabs growing off neighboring oriented nuclei is occurring at later times with increasing ethylene content.

The comparison between the upturn in retardance during flow and the residual level of retardance right after cessation of flow is shown in Figure 3.22. First, it can be observed that, for the same flow conditions, both the upturn and residual retardance decrease with increasing ethylene, indicating that a smaller amount of long-lived oriented structures (oriented precursors and possibly some kebabs) form during flow.

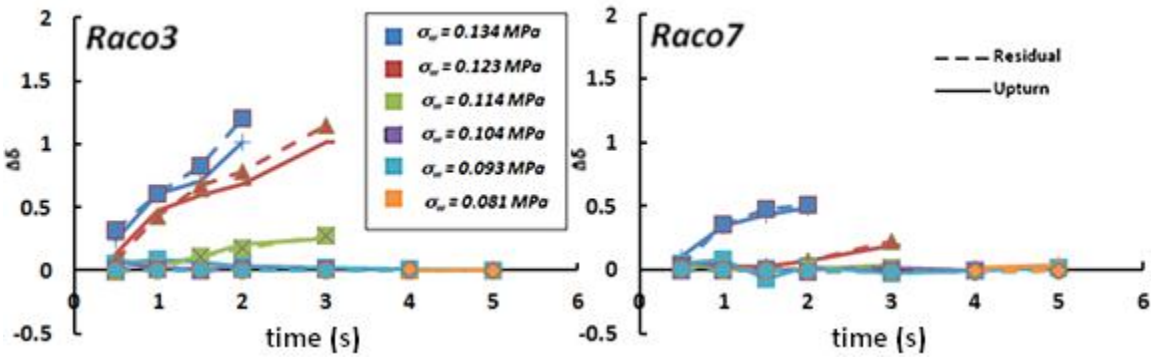

Figure 3.22 Comparison between upturn (line) and residual (dashed line) retardance at given σ_w and ts.for (left) Raco3 and (right) Raco7.

Similarly to iPP, the residual retardance for Raco3 is larger than the upturn at the highest σ_w and longest ts (Figure 3.22, left), although the discrepancy is not as large as for iPP (Figure 3.14). This effect is absent with Raco7, for which the upturn and residual retardance coincide (Figure 3.22, right).

The difference in residual retardance and upturn is attributed to a delay ≥ 1 s for the complete relaxation of retardation after cessation of flow. For iPP and Raco3, the large amounts of oriented nuclei formed at the strongest flow conditions combined with relatively large linear growth rates G leads to large quantities of kebabs forming during this delay. The result is observed by a continuous increase of retardance right after flow which precludes retardance from reaching a lower value matching the magnitude of the upturn. Indeed, note that after cessation of flow, it takes at least 1 s for the retardance to reach its minimum relaxed value (for example in Figure 3.23, All curves in Raco7 except the dark blue one [ie : all not oriented samples]). However, for Figure 3.23 (iPP blue dark curve) the high rate of growth of kebabs manifested by the large initial slope after stopping flow prevents the retardance from reaching the minimum value it would have otherwise.

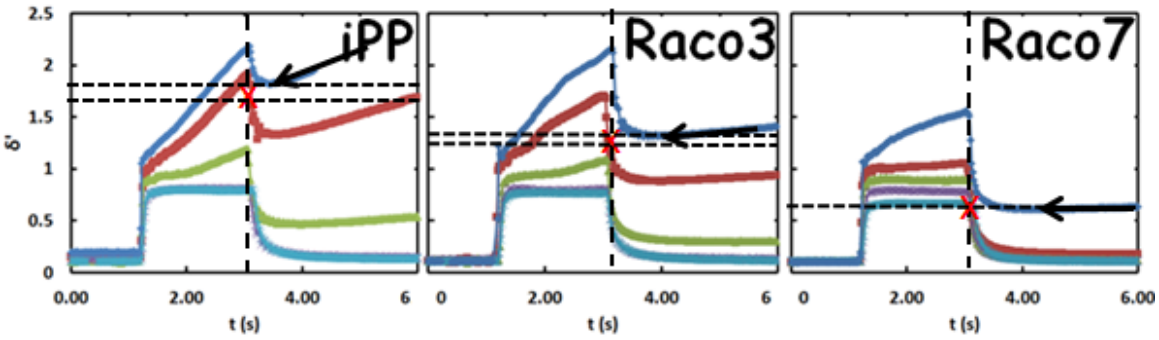

Figure 3.23 Representation of retardance experiments for iPP, Raco3 and Raco7. One can denote the influence of the growth of kebabs on the residual signal : Vertical dashed line shows the cessation of flow, the arrow shows the height of the actual residual while the red cross shows the expected residual without kebabs influence. The two horizontal lines denote the difference between expected residual and actual residual.

3.2.7 Depth sectioning

The depth sectioning is particularly interesting to isolate the effect of stress on microstructure at different depths. The depth sectioned retardance D.S.δ for 2s shown in

Figure 3.25 is representative of most shearing times (except ts = 0.5 s, and for iPP ts = 1s, Figure 0.12, Figure 0.13 and Figure 0.14 in appendix). In general terms, it can be deduced that the increase of birefringence and retardance shown earlier for samples with oriented skins (See appendix) were dominated by the outermost layers (L1-L3 for iPP and Raco3, L1-L2 for Raco7, see Figure 3.24), which present the highest oriented nucleation. For the innermost layers (lower δ, L4), the nucleation is low so its contribution to the signal is minimal.

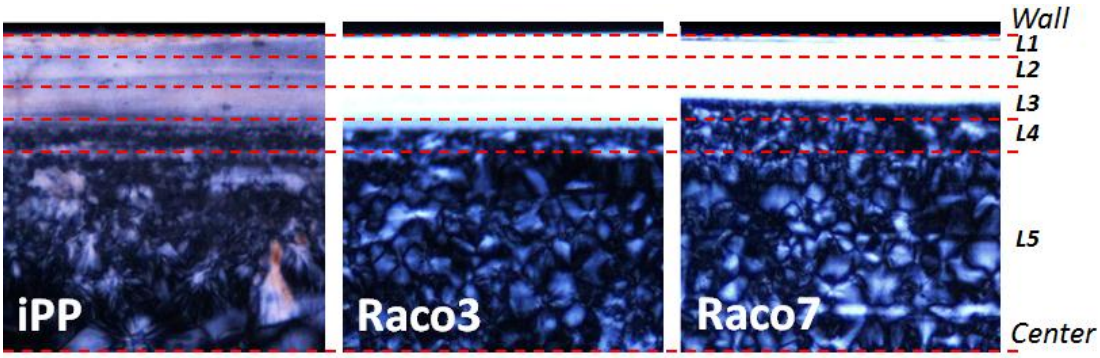

Figure 3.24 Definition of the layers thickness for the three grades

Surprisingly, for iPP and Raco3, the retardance of the outermost layer L1 (0.134-0.123 MPa, blue inFigure 3.25) increases at a lower rate during flow than the retardance of the adjacent layer L2 (0.123-0.114 MPa, red in Figure 3.25). In contrast, for Raco7, the increase of all depth sectioned retardances for outermost L1 during shear is higher than for layers further from the wall (i.e. subject to lower σ).

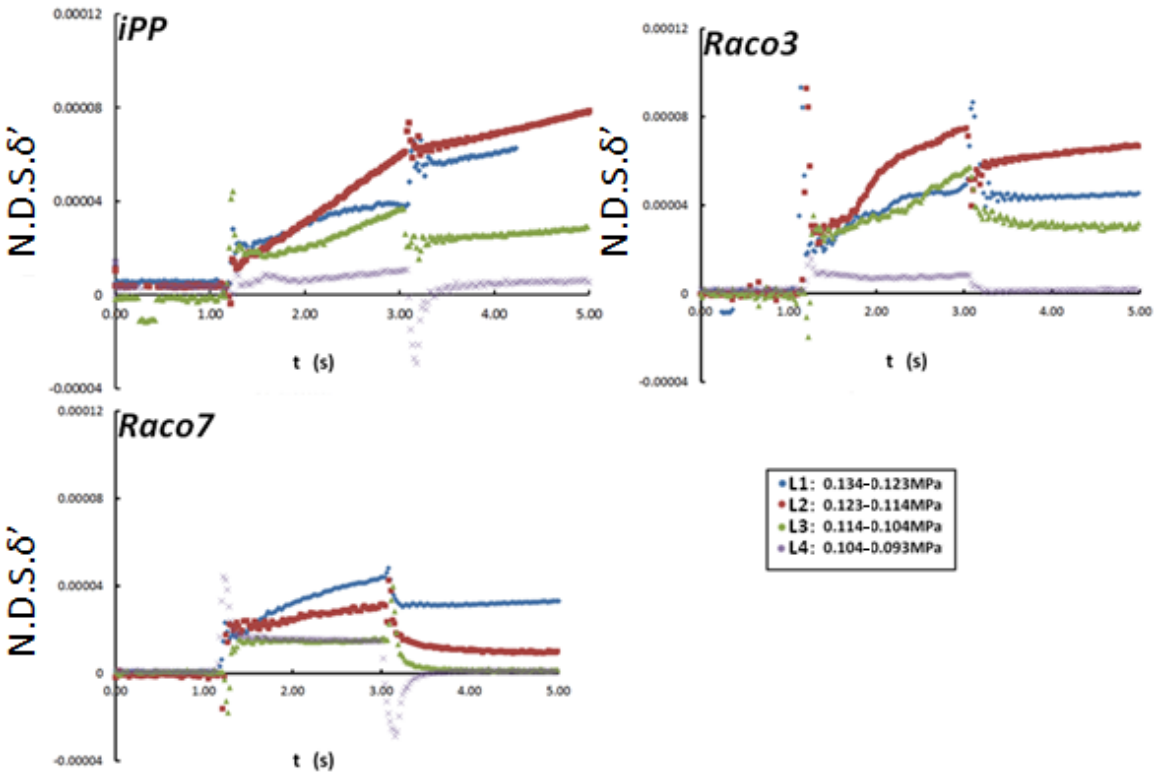

Figure 3.25 Depht sectioning of retardance D.S. δ'of iPP at a shearing time of 2 seconds revealing a domination of precursor for the outermost layer with iPP and Raco3.

The drop after cessation of flow corresponds to the drop in melt flow birefringence, as explained earlier. It's interesting to note that for iPP, layers subject to the highest σ and to ts > 0.5-1s, the drop in retardance after cessation of flow is essentially absent (Figure 3.25 iPP, L1 and L2, see Figure 0.12). This can be related to significant crystallization occurring during flow for iPP outermost layers (i.e. subject to higher σ) resulting in minimal contribution from melt flow birefringence.

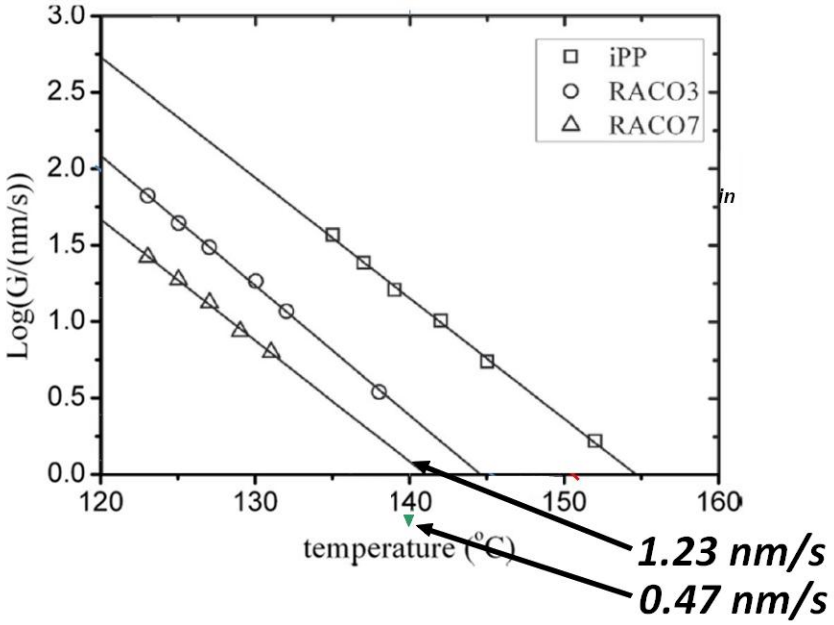

Figure 3.26 Linear growth rate of iPP, Raco3 and Raco7 (1.23nm/s at 140°C) from [56].The green triangle (0.47nm/s) represents the measured linear growth rate from the fiber pull test after 12 hours of isothermal crystallization at 140°C.

The initial slopes of depth sectioning right after shear have been computed and normalized by the linear growth rates G of 14.07, 2.44 and 1.23 nm/s for iPP, Raco3 and Raco7 respectively [56]. In Figure 3.27, these initial slopes N.D.S.δ′ are plotted vs, the highest stress in each layer. The required extrapolation of the linear growth rate in [56] being high at 140°C, a fiber pull test has been carried out assuming the growth of crystals at a quiescent growth velocity. Experimental protocol followed is explained in [69]. The temperature of crystallization is chosen to be at the regular temperature of crystallization for this project (ie : 140°C). The growth of crystals has been observed under optical polarized microscope during 12hours. The deducted linear growth rate G of Raco7 has been computed and reveal a slower velocity than expected from [56] with G = 0.47nm/s (Figure 3.27).

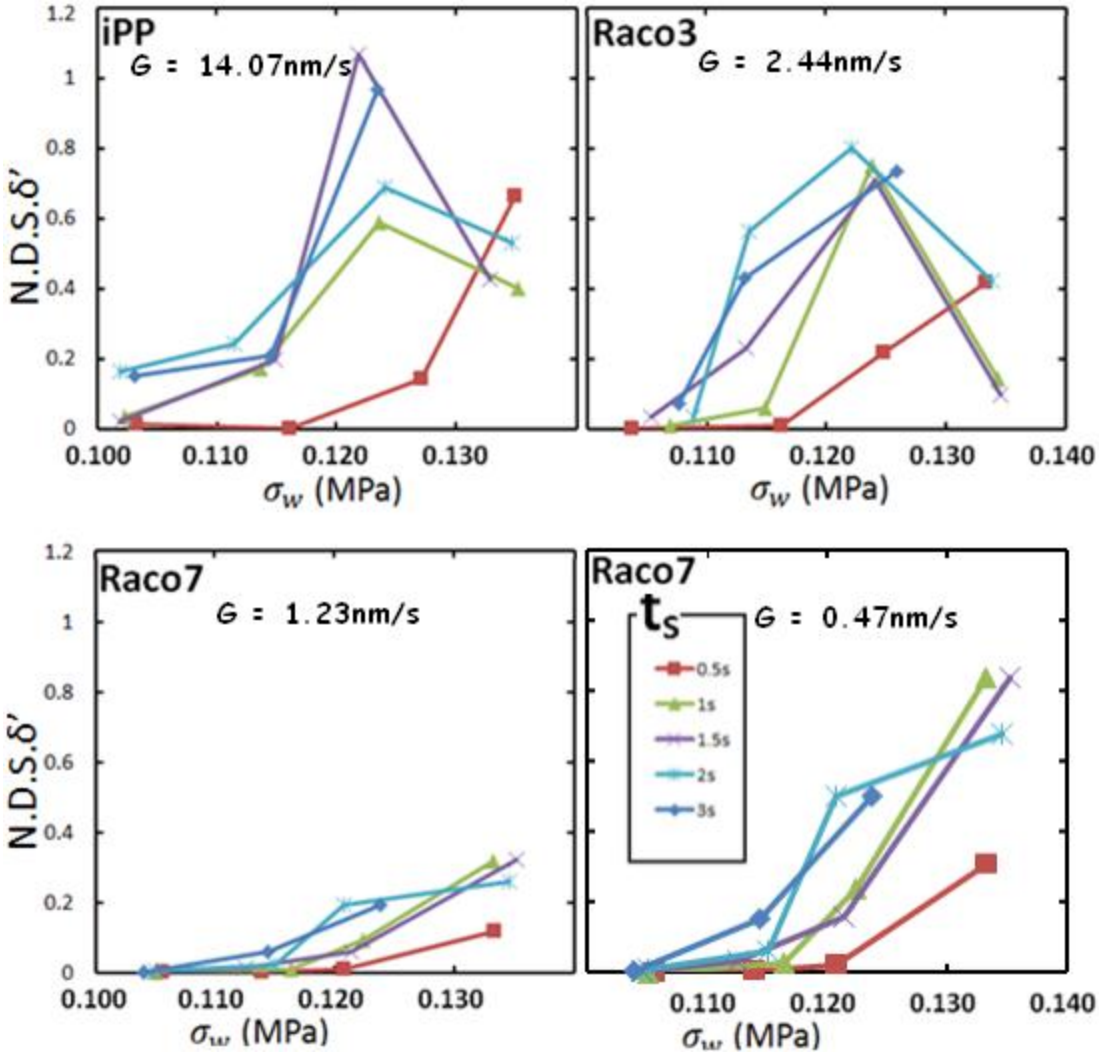

Figure 3.27 Initial slopes of normalized depth sectioning (by linear growth rate G) versus wall shear stress.

For iPP and Raco3 and ts ≥ 1 s, the initial N.D.S.δ' increases with increasing σ for layers up to L2, indicating that the total length of oriented precursors formed strongly increases with higher levels of stress. Surprisingly, at the highest σ (outermost layer L1, 0.134-0.123 MPa) a sudden drop in the initial N.D.S.δ' occurs in the outermost layer (L1) indicating a lower nucleation of oriented precursors. However, Raco7 does not display any drop in L1.

A few scenarios might explain the observation of such drop in iPP and Raco3. At the highest stress level, it's expected that large amounts of oriented nuclei will form very quickly, onto which kebabs can start immediately growing. At such high nucleation densities, a destructive action during flow can take place: molecular bridges between oriented crystallites can break during flow due to the large difference of shear rate between them [29]. Also, the high density of oriented nuclei formed early during flow implies that there is much less free space for other oriented nuclei to develop during the remainder of the shear pulse. Finally, the formation early during flow of large amounts of oriented nuclei and corresponding oriented crystallites increases the viscosity, thus lowering the achieved shear rate, which may have an impact on further development of oriented nuclei. Interestingly, Raco7 does not seem to encounter these scenarios.

It's interesting that even though the L1, L2 and L3 layers correspond to the oriented skin for iPP and Raco3 (see Figure 3.24 left and middle), Figure 3.27 shows that the contribution to orientation is different for each layer, which means that the nucleation density can be inhomogeneous within the oriented skin.

3.3 Capillary rheometry

The determination of the true shear rate at the wall has required the determination of the volumetric flow rate Q. Using the particular convenient configuration of the duct flow, the determination of the *n* power law coefficient and the viscosity has been realized.

It must be noted that wall shear stress σ_w never exceeded 0.15 MPa so no slip or melt fracture was expected [37]. The throughput has been thoroughly monitored to

ensure that no slip was encountered. Wall slip happens when a critical flow rate is exceeded and can lead to distortion such as sharkskin aspect [70], slip-stick, bamboo melt fracture and highly distorted extrudate [70]. Polypropylene slip usually results in spiral or corkscrew aspect [70]. For capillary experiments, slip decreases the shear stress which can be observed as a decrease of viscosity [70]. None of these aspects have been encountered during the experiments.

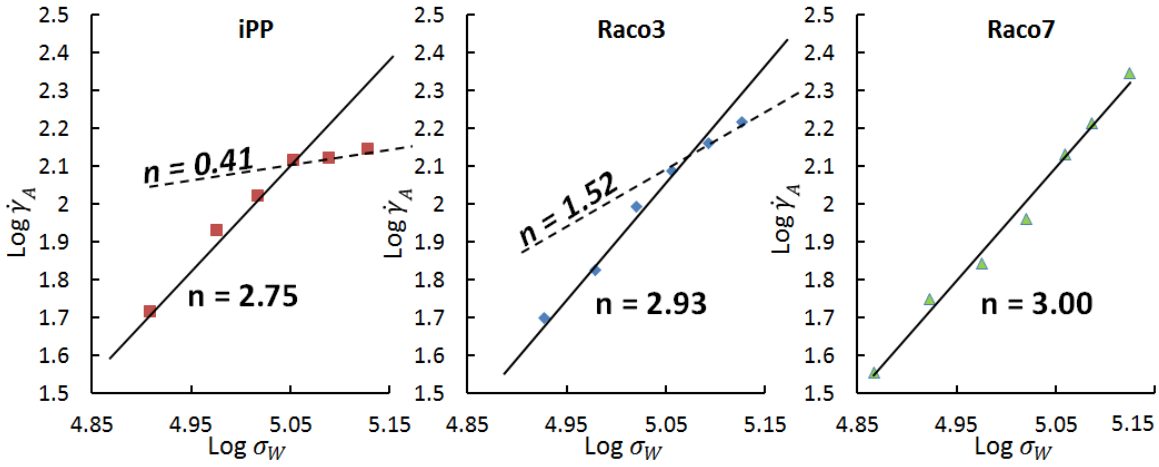

Figure 3.28 Determination of n exponent from the power law behavior of the polymer (in dash line is represented the n value of the broken curve)

The *n* coefficient can be found for the three grades in Figure 3.28 that show an exponent *n* particularly close for the two copolymers and slightly lower for the homopolymer. Interestingly the curves display a broken shape at high shear stress for iPP and Raco3 displaying a different value of *n*. As no slip is assumed, this change of state corresponds to the appearance of highly oriented layers for homopolymer, however, while the copolymer Raco7 is also subject to these layers no change happens on his *n* exponent.

It has been shown that a drastic increase in viscosity arises from the appearance of crystals in the sheared melt [71]. When very low amounts of crystallites are present, the viscosity exhibits amorphous behavior but adopts a ‘step-like’ change once significant crystallization occurs [71]. The physical mechanism is not completely understood, but the existence of two critical strain rates has been hypothesized: the first one corresponds to individual stretching of chains, while the second one corresponds to the stretch of a network of chains. This cooperative work of chains—acting as a network— increases the viscosity tremendously [72].

Thus, the initial *n* value is retained on the three grades corresponding to the region of nondestructive flow at values respectively 2.75, 2.93 and 3.00 for iPP, Raco3 and Raco7. The points corresponding to the destructive flow are computed separately and correspond to n value of respectively 0.41 and 1.52 for iPP and Raco3. The viscosity has then been computed considering the two regimes of flow described earlier (Figure 3.29). Under nondestructive flow, the three grades of polymer display the same viscosity profile against the true shear rate, which here exhibit a shear thinning behavior. As stated previously, once under the destructive domain of flow, the viscosity increases while bridges formation between nuclei trend the shear rate to decrease.

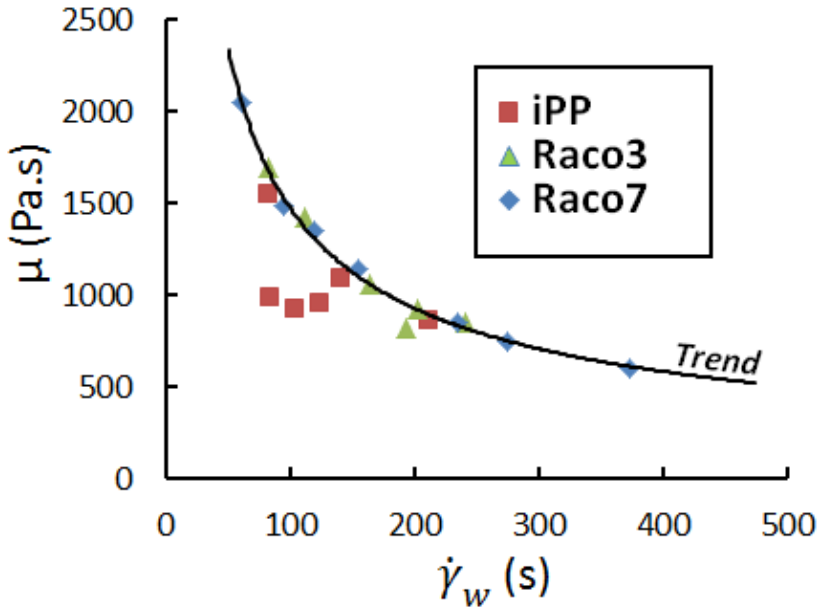

Figure 3.29 Viscosity versus true shear rate.

3.4 The Black layer

Some flow-induced crystallization samples for Raco3 and Raco7 exhibit a black layer that appears dark under cross polarizers when aligned at 45 degrees with respect to P and bright when parallel to P (opposite to the behavior of highly oriented skin layers, Figure 3.17 A) and D)). The fact that the black layer appears bright when oriented along the P directions indicates that there it has an oriented structure. It is interesting to note that if a section is obtained perpendicular to flow (in the plane perpendicular to $\vec{v}$ and $\Delta\vec{v}$), the black layer appears bright when oriented at 45° to P (Figure 3.30), instead of dark as the skin would appear (Figure 0.15) Black layers are never found for iPP (Figure 3.5). For Raco3, it is observed under low stresses and t_s such $t_s \leq 1$ s and $\sigma_w \leq 0.093$MPa and for Raco7 is is found at $t_s \leq 1$ s and $\sigma_w \leq 0.104$MPa (Figure 0.10 and Figure 0.11 in

appendix). This layer has not been observed in quiescent experiments, indicating that it is induced by flow.

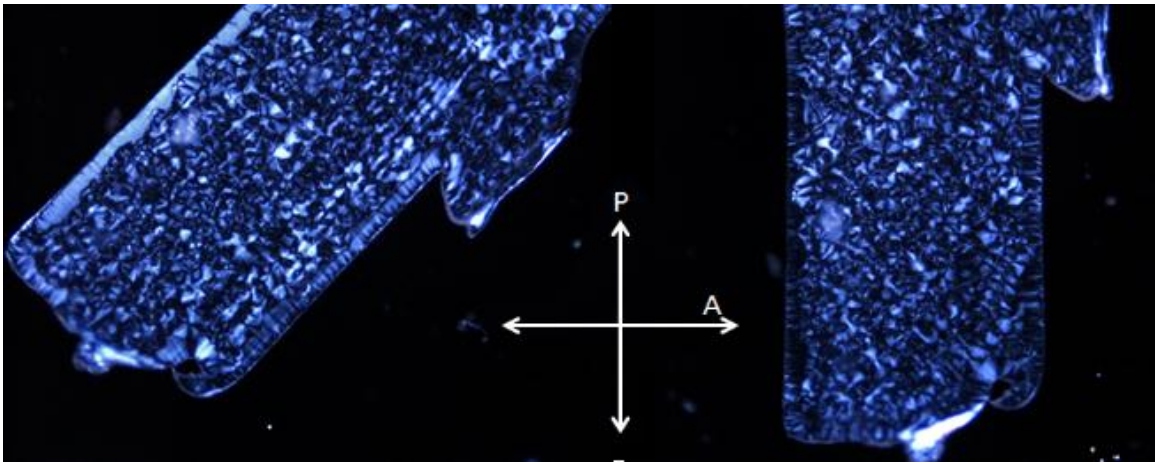

Figure 3.30 Transversal cut from the flow of sample manifesting a black layer.

The experimental range of conditions for appearance of this black layer is biggest for Raco7 and nonexistent for iPP. Therefore, it is hypothesized that the presence of significant γ-phase or α branching could be the cause of appearance of the black layer. Indeed, it is well known that increasing ethylene content encourages the formation of γ-phase and α branching [57] [11].

Wide Angle X-ray Diffraction (WAXD) performed on the sample displaying the largest black layer (Raco7, t_s = 0.5s, σ_w= 0.093 MPa, black layer with a thickness of ~30 microns, i.e. 11%) shows a strong dominance of α phase by the presence of large peaks from the reflection of planes $(110)_\alpha$, $(040)_\alpha$, $(130)_\alpha$, $(111)_\alpha$ and $(041)_\alpha$ (Figure 3.31). No characteristic β peak can be discerned. However, at $2\theta = 20.07°$ there is a slight peak representative of the plane $(117)_\gamma$ from the γ-phase [73]. Other γ peaks such as $(008)_\gamma$ and $(111)_\gamma$ cannot be distinguished as they are hidden by $(110)_\alpha$, and $(040)_\alpha$. The amount of γ phase seems to be too low for the black layer to be caused by it.

The presence of α branching is distinguished by looking at the azimuthal distribution of the $(110)_\alpha$ reflection: the equatorial intensity corresponds to the parent lamellae and the meridional one comes from the daughters [74]. Figure 3.31 is an azimuthal average already, so no information about the amount of parent-to-daughter lamellae can be obtained. Previous studies have found that α-branching is highly probable especially for low flow rate while high flow rate induced preferential growth in the c-axis [74], which is mainly the axis of formation of shish-kebabs structures [75],

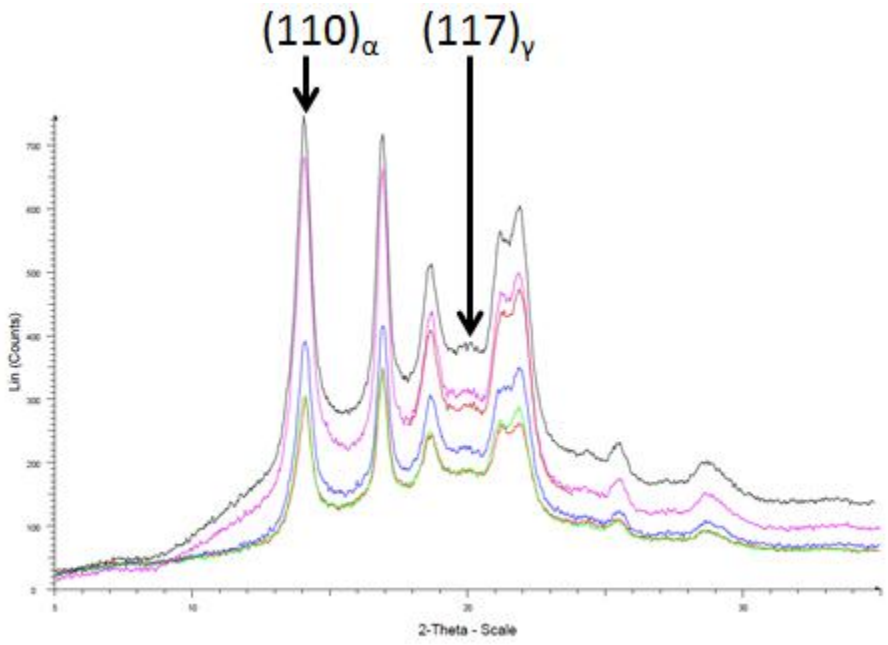

Figure 3.31 WAXD pattern for sample manifesting a black layer (Raco7, ts=0.5s, σw=0.093MPa).

The thickness of the black layer appears to decrease for longer t_s or higher wall shear stresses σ_w until it completely disappears. At a given σ_w, the black layer is found for the lowest ts, while a sufficient increase in t_s causes the appearance of a fine-grained layer and disappearance of the black layer.

The thickness of the black layers found along with the linear growth rates of Raco3 and Raco7 at 140C indicate that the black layer must have formed during cooling. Indeed, according to the reported linear growth rate of Raco7 [56], it is not possible to grow a layer thickness of 30 microns during isothermal crystallization at 140°C for only 1 hour: only 4.4 μm would be reached with G = 1.23 nm/s extrapolated in literature [56], or 1.7 microns with our measured G = 0.47 nm/s (fiber pull experiment).

For a better understanding of the cause of this layer formation, several experiments have been carried out. A summary is stated in the table below, all experiments have been realized under shear impulse favorable for black layer formation under regular test with ts = 0.5 s, T = 140°C and σ_w = 0.093 MPa :

Table 3.2 Results of tests for Black Layer determination for specifics crystallization conditions after shear impulse with ts = 0.5s, T = 140°C and σ_w = 0.093 MPa.

	Crystallization conditions	**Time of crystallization before quenching**	**Results**
1)	Isothermal at 140°C	1 hour	**Black layer (BL)** – Small core spherulites
2)	Isothermal at 140°C	11 hours	Crystallized from border – Small size core spherulites
3)	Slow cooling from 140C to 100C at ~ 0.7°C/min	1 hour	Border has lower shrerulite sizes - Medium size core spherulites
4)	Fast cooling to 100°C (~ xxC/min) and then isothermal at 100C	1 hour	Small size spherulites at the border, big size spherulites at the center
5)	Fast cooling to 80°C (~ XXC/min) and then isothermal at 80C	1 hour	Small size spherulites core – **slight appearance of black layer**

Figures in appendix (Figure 0.16)

Condition 1) and 2) demonstrate that this particular layer doesn't grow from the isothermal quiescent crystallization at 140C after shear as expected from the kinetics analysis made previously in this section. Indeed, 2) doesn't exhibit a black layer (BL) but crystallization has happened during isothermal crystallization (increase of turbidity of 25%, during isothermal not shown in Table 3.2) from the border.

The condition 3) demonstrates that the growth of spherulites in the range of temperature comprised between 140 and 100°C prevent the formation of the black layer. This layer must appear at a lower temperature which seems confirmed by the condition 4) that does not display BL. The appearance of the BL in condition 5) confirms the lower range of temperature required. Hence, The black layer only appear at lower temperatures (which for our experiments were only reached during the cooling of the cartridge) and its size seems limited by the quick development of spherulites at this range of temperature manifested by the small size of the spherulites from the core which may explain that no experiment has allowed a better expansion of this BL.

Conclusion

The effect of random ethylene comonomer content on flow-induced crystallization has been examined. For all polymers, ex-situ optical polarized micrographs show that the critical shear stress for formation of a highly oriented skin ($\sigma_{crit\text{-}skin}$) first decreases with increasing shearing time and then reaches a plateau ($\sigma_{crit\text{-}plateau}$) for ts ≥ 1 s. Interestingly, the presence of 3.4% ethylene does not noticeably affect the plateau critical stress: both iPP and Raco3 have the same $\sigma_{crit\text{-}skin}$ ~ 0.100 MPa. However, Raco7 at 7.3% comonomer contents does exhibit a higher value of $\sigma_{crit\text{-}plateau}$ ~ 0.105 MPa.

A threshold of specific work ($W = \sigma_{..}\dot{\gamma}.\ t_{s,}$) for formation of the highly oriented skin has also been investigated. It was found that for all three grades and stresses $\sigma_w < \sigma_{crit\text{-}plateau,}$ orientation cannot be triggered even at relatively high levels of applied specific work. When the imposed stress $\sigma_w > \sigma_{crit\text{-}plateau}$, the required specific work to induce a highly oriented skin decreases with increasing applied stress, and a highly oriented skin is always formed if a given threshold of specific work is reached. The specific value of such threshold specific work does not seem to be dependent of the amount of ethylene content (no clear trend).

The flow-induced crystallization kinetics are observed to decrease with the amount of ethylene, as expected. The kinetics of crystallization are greatly accelerated for all three grades, especially for conditions that allow formation of a highly oriented skin. In most cases where this skin is formed, the retardance measurements exhibits and slow

down in growth (knee) which signals that kebabs growing off neighboring threads have impinged. The comparison of retardance and turbidity for Raco7 indicates that the highly oriented skin does not contribute greatly to the loss of clarity; hence, it may arise mainly from the oriented lines and fine-grained layer that develop quickly for iPP. Also, the residual retardance after cessation of flow is larger than the upturn retardance at the highest levels of stress and shearing time for iPP and Raco3. This observation indicates that the amounts of kebabs growing for 1s after cessation of flow is large enough to significantly contribute to the retardance signal.

The use of the depth sectioning method allows isolating the contribution of the retardation at different depths of the samples, so that the amount of oriented crystallites can be tracked and the relative total length of oriented nuclei can be estimated. All three grades exhibit varying total lengths of oriented nuclei at different depths of the oriented skin; in other words, the oriented skin is not homogenous. In general, the density of oriented nuclei increases with increasing stress σ except for the outermost layer of the 'oriented skin' and ts > 0.5 s (i.e. subject to the highest σ) of both iPP and RACO#, where the birefringence contribution is lower than for the adjacent layer. This may be attributed to a process of saturation or destruction that seems to be reflected in a drastic change of viscosity only observed for iPP and RACO3 at the highest level of stress. The lowest total length of nuclei for RACO7 and for ts < 1 s after shear may delay the observation of saturation to high levels of stress that were not encountered in this work.

Bibliography

[1] J. Karger-Kocsis, Polypropylene Structure, blends and composites volume 1 Structure and morphology, London: Chapman & Hall, 1995.

[2] D. v. d. Meer, "Structure-Property Relationships in Isotactic Polypropylene," 2003.

[3] Moore, Polypropylene handbook, Munich: Hanser Publisher, 1996.

[4] Ravi Kumar and Giridhar Madras, "Thermal degradation kinetics of isotactic and atactic polypropylene," *Journal of Applied Polymer Science,* vol. 90, no. 8, p. 2206–2213, 2003.

[5] B. Lotz, S. Graff, C. Straupé and J.C. Wittmann, "Single crystals of γ-phase isotactic polypropylene: Combined diffraction and morphological support for a structure with non-parallel chains," *Polymer,* vol. 32, no. 16, p. 2902–2910, 1991.

[6] B. Lotz, "alpha and beta phases of isotactic polypropylene: a case of growth kinetics ‘phase reentrency’ in polymer crystallization," vol. 39, no. 19, 1998.

[7] Bin Zhang , Jingbo Chen, Jing Cui, Hui Zhang, Fangfang Ji, Guoqiang Zheng, Barbara Heck, Günter Reiter and Changyu Shen, "Effect of shear stress on crystallization of isotactic polypropylene from a structured Melt," *Macromolecules,* vol. 45, no. 21, p. 8933–8937, 2012.

[8] B. Lotz and J. C. Wittmann, "The molecular origin of lamellar branching in the α (monoclinic) form of isotactic polypropylene," *Journal of Polymer Science Part B: Polymer Physics,* vol. 24, no. 7, p. 1541–1558, 1986.

[9] K. Mezghani and P. J. Phillips, "The γ-phase of high molecular weight isotactic polypropylene III - The equilibrium melting point and the phase diagram," *Polymer,* vol. 39, no. 16, p. 3735–3744, 1998.

[10] I. L. Hosier, R. G. Alamo and J.S. Lin, "Lamellar morphology of random metallocene propylene copolymers studied by atomic force microscopy," *Polymer,* vol. 45, p. 3441–3455, 2004.

[11] Claudio De Rosa, Finizia Auriemma and Luigi Resconi, "Influence of Chain Microstructure on the Crystallization Kinetics of Metallocene-Made Isotactic Polypropylene," *Macromolecules,* vol. 38, pp. 10080-10088, 2005.

[12] C. De Rosa, F. Auriemma, M. Paolillo, L. Resconi and I. Camurati, "Crystallization Behavior and Mechanical Properties of Regiodefective, Highly Stereoregular Isotactic Polypropylene: Effect of Regiodefects versus Stereodefects and Influence of the Molecular Mass," *macromolecules,* vol. 38, pp. 9143-9154, 2005.

[13] Mezghani, K., Anderson Campbell, R. and Phillips, P.J, "Lamellar Thickening and the Equilibrium Melting Point of Polypropylene," *Macromolecules,* vol. 27, p. 997–1002, 1994.

[14] R. P.A.Lovell, Introduction to polymers Second Edition, London: Chapman and Hall, 1991.

[15] Ratta, Varun , "Crystallization, Morphology, Thermal Stability and Adhesive Properties of Novel High Performance Semicrystalline Polyimides," VirginiaTech, 1999.

[16] D. C. Bassett, "Polymer Morphology - Pure and applied," *Journal of Macromolecular Science, Part B,* vol. 35, no. 3, pp. 277-294, 1996.

[17] Ewa Piorkowska and Gregory C. Rutledge, Handbook of Polymer Crystallization, Wiley; 1 edition, 2013.

[18] P.J.Bassett, Materials Science and Technology: A Comprehensive Treatment, vol. 12, Weinheim: Materials science and technology, 1993.

[19] J. W. B. Lotz, Materials Science and Technology: A Comprehensive Treatment, vol. 12, Weinheim: Materials Science and Technology, 1993, pp. 79-151.

[20] Claudia Stern, "On the Performance of Polypropylene between synthesis and end-use properties," University of Twente, 2005.

[21] A. K. M.J.Hill, "Further studies on polyethylene crystallized under stress: Morphology, calorimetry, and stress relaxation," *Journal of Macromolecular Science Part B,* vol. 5, no. 3, pp. 591-615, 1971.

[22] A. E. Woodward, Understanding polymer morphology, New York: Hanser Publishers, 1995.

[23] M. R. Kantz, H. D. Newman Jr and F. H. Stigale, "The skin-core morphology and structure-property relationships in injection-molded polypropylene," *Journal of Applied Polymer Science,* vol. 16, no. 5, p. 1249–1260, 1972.

[24] J. A. Kornfield, G. Kumaraswamy and A. M.Issaian, "Recent advances in understanding flow effects on polymer crystallization," *Amecican Chemical Society,* vol. 41, pp. 6383-6392, 2002.

[25] Hongyi Zhou, "Structure-property relationships model studies on melt extruded uniaxially oriented high density polyethylene films having well defined morphologies," Virginia Polytechnic Institute and State University, 1997.

[26] Oleksandr O. Mykhaylyk, Christine M. Fernyhough, Masayuki Okura, J. Patrick A. Fairclough, Anthony J. Ryan and Richard Graham, "Monodisperse macromolecules – A stepping stone to understanding industrial polymers," *European Polymer Journal,* vol. 47, no. 4, p. 447–464, 2011.

[27] Qing Chen, Yu-run Fan and Qiang Zheng, "Shear induced crystallization of high-density polyethylene," *Journal of Central South University of Technology* , vol. 14, no. 1, pp. 174-177, 2007.

[28] G Kumaraswamy, JA Kornfield, F Yeh and BS Hsiao, "Shear-enhanced crystallization in isotactic polypropylene. 3. Evidence for a kinetic pathway to nucleation," *Macromolecules,* vol. 35, no. 5, p. 1762–1769, 2002.

[29] E. R. H. Janeschitz-Kriegl, "Some fundamental aspects of the kinetics of flow-induced crystallization of polymers," vol. 288, no. 16-17, 2010.

[30] H. Janeschitz-Kriegl, Crystallization Modalities in Polymer Melt Processing, Springer Vienna, 2010.

[31] G. Eder, H. Janeschitz-Kriegl and G. Krobat, "Shear induced crystallization, a relaxation phenomenon in polymer melts," *Progress in Colloid & Polymer Science,* vol. 80, pp. 1-7, 1989.

[32] Eder, G. and H. Janeschitz-Kriegl, "'Crystallization' in Processing of Polymers," *Journal of*

Materials Science & Technology, vol. 18, pp. 189-268, 1997.

[33] H. Ito, K. Minagawa, J. Takimoto, K. Tada and K. Koyama, "Effect of pressure and shear stress on crystallization behaviors in injection molding," *International Polymer processing XI,* vol. 4, pp. 363-368, 1996.

[34] O. Verhoyen, F. Dupret and R. Legras, "Isothermal and non-isothermal crystallization kinetics of polyethylene terephthalate: Mathematical modeling and experimental measurments," *Polymer Engineering and Science,* vol. 38, no. 9, pp. 1594-1610, 1998.

[35] Julie Kornfield et al, "Molecular Aspects of Flow-Induced Crystallization of Polymers," *Prog. Theor. Phys. Supplement ,* vol. 175, pp. 10-16, 2008.

[36] Emmanuelle Koscher and Rene Fulchiron, "Influence of shear on polypropylene crystallization: morphology," *Polymer,* vol. 43, no. 25, p. 6931–6942, 2002.

[37] Guruswamy Kumaraswamy, Ravi K. Verma and Julia A. Kornfield, "Novel flow apparatus for investigating shear-enhanced crystallization and structure development in semicrystalline polymers," *Review of Scientific Instruments,* vol. 70, no. 4, pp. 2097- 2104, 1999.

[38] Peter Jerschow and Hermann Janeschitz-Krieg, "On the development of oblong particles as precursors for polymer crystallization from shear flow: Origin of the so-called fine grained layers," *Rheologica Acta,* vol. 35, no. 2, pp. 127-133, 1996.

[39] Rajesh H. Somani, Benjamin S. Hsiao and Aurora Nogales, "Structure development during shear flow-induced crystallization of i-PP: In-situ small-angle X-ray scattering study," *Macromolecules,* vol. 33, pp. 9385-9394, 2000.

[40] Jean-Marc Haudin, Catherine Duplay and Bernard Monass, "Shear-induced crystallization of polypropylene. Growth enhancement and rheology in the crystallization range," *Macromolecular Symposia,* vol. 185, no. 1, p. 119–133, 2002.

[41] Pawan K et al, "Shear-Induced Crystallization in Novel Long Chain Branched," *Macromolecules,* vol. 36, pp. 5226 - 5235, 2003.

[42] P.G.De Gennes, "Coilstretch transition of dilute flexible polymers under ultrahigh velocity," *J. Chem. Phys,* vol. 60, no. 12, 1974.

[43] J. A. Odell, A. Keller and A. J. Muller, "Thermomechanical degradation of macromolecules," *Colloid and Polymer Science,* vol. 270, no. 4, pp. 307-324, 1992.

[44] Oleksandr O. Mykhaylyk, Pierre Chambon, Ciro Impradice, J. Patrick A. Fairclough, Nick J. Terrill and Anthony J. Ryan, "Control of Structural Morphology in Shear-Induced Crystallization of Polymers," *Macromolecules,* vol. 43, p. 2389–2405, 2010.

[45] Huong D.M., Drechsler M., Möller M. and Cantow H., "Electron Spectroscopic Imaging of Polyethylene Shish Kebabs in Situ.," *Journal of Microscopy,* vol. 166, pp. 317-328, 1992.

[46] Sanchez, Isaac C.; and Eby, R.K., "Crystallization of Random Copolymers," *National Bureau of Standards,* vol. 77, no. 3, p. 353, 1973.

[47] Rufina G. Alamo, D. L. VanderHart, Marc R. Nyden and L. Mandelkern, "Morphological Partitioning of Ethylene Defects in Random Propylene Ethylene Copolymers," *Macromolecules,* vol. 33, pp. 6094-6105, 2000.

[48] R. G. A. a. L. Mandelkern, "Crystallization Kinetics of Random Ethylene Copolymers," Vols. 24, 6480-6493, 1991.

[49] Julie Tammy Uan-Zo-li, "Morphology, Crystallization and Melting Behavior of Statistical Copolymers of Propylene," Virginia Polytechnic Institute and State University, Virginia, 2005.

[50] Paul J. Flory, Leo Mandelkern and Henry K. Hall, "Crystallization in High Polymers. VII. Heat of Fusion of Poly-(N,N'-sebacoylpiperazine) and its Interaction with Diluents," *journal*

of the american chemical society, vol. 73, no. 6, pp. 2532-2538, 1951.

[51] Paul J. Flory, "Theory of crystallization in copolymers," *Trans. Faraday Soc,* vol. 51, no. 0, pp. 848-857, 1955.

[52] Jan-Willem Housmans, Gerrit W. M. Peters and Han E. H, "Flow-induced crystallization of propylene/ethylene random copolymers," *Journal of Thermal Analysis and Calorimetry,* vol. 98, pp. 693-705, 2009.

[53] K. Mezghani, R. Anderson Campbell and PJ. Phillips, "Lamellarthickening and the equilibrium melting point of polypropylene," *Macromolecules,* vol. 27, p. 997–1002, 1994.

[54] Y.L. Chiar, M. Vadlamudi, R. Chella, K. Jeon and R. G. Alamo, "Overall crystallization kinetics of polymorphic propylene–ethylene random copolymers: A two-stage parallel model of Avrami kinetics," *Polymer,* vol. 48, no. 11, p. 3170–3182, 2007.

[55] K. F. W. John M. Dealy, Melt Rheology and Its Role in Plastics Processing, Springer Netherlands, 1990.

[56] Z. Ma, L. Fernandez-Ballester, D. Cavallo, T. Gough and G. W. M. Peters, "High-Stress Shear-Induced Crystallization in Isotactic Polypropylene and Propylene/Ethylene Random Copolymers," *Macromolecules,* vol. 46, no. 7, p. 2671–2680, 2013.

[57] Markus Gahleitner et al, "Propylene–Ethylene Random Copolymers: Comonomer Effects on Crystallinity and Application Properties," *Journal of Applied Polymer Science ,* vol. 95, no. 5, p. 1073–1081, 2005.

[58] J. Aho and S. Syrjälä, "Shear viscosity measurements of polymer melts using injection molding machine with adjustable slit die," *Polymer Testing,* vol. 30, pp. 595-601, 2011.

[59] Macosko and Christopher W., Rheology - Principles, Measurements and Applications, John Wiley & Sons, 1994.

[60] Lucia Fernandez-Ballester, Derek W. Thurman and Julia A. Kornfield, "Real-time depth sectioning: Isolating the effect of stress on structure development in pressure-driven flow," *Journal of Rheology,* vol. 53, no. 5, pp. 1229-1224, 2009.

[61] K. Hongladarom, W. R. Burghardt, S. G. Baek, S. Cementwala and J. J. Magda, "Molecular alignment of polymer liquid crystals in shear flows. 1. Spectrographic birefringence technique, steady-state orientation, and normal stress behavior in poly(benzyl glutamate) solutions," *Macromolecules,* vol. 26, no. 4, p. 772–784, 2002.

[62] C. p. group, The theory of birefringence, Cambridge polymer group, inc, 2004.

[63] S. Royse, "Fabrication and Characterization of Biocomposites from Polylactic Acid and Bamboo Fibers," 2012.

[64] "Guide to Diamond Knife Use & Care".

[65] F. Bédoui, J. Diani and G. Régnier, "Micromechanical modeling of elastic properties in polyolefins," *Polymer,* vol. 45, no. 7, pp. 2433-2442, 2004.

[66] A. K. Ghosal, "Crystallization of Isotactic Poly(Propylenes) with," DigiNole Commons, Florida State University, 2007.

[67] J.-W. Housmans, R. J. A. Steenbakkers, P. C. Roozemond, G. W. M. Peters and H. E. H. Meijer, "Saturation of Pointlike Nuclei and the Transition to Oriented Structures in Flow-Induced Crystallization of Isotactic Polypropylene," *Macromolecules,* vol. 42, p. 5728–5740, 2009.

[68] L. Fernandez-Ballester, D. W. Thurman, W. Zhou and J. A. Kornfield, "The effect of long chains on the threshold stresses for flow-induced crystallization in iPP: Shish-kebabs vs. sausages.," *Macromolecules,* vol. 45, pp. 6557-6570, 2012.

[69] B. Schamme, "Relaxation of Shear-Induced Precursors in Isotactic Polypropylene and

Random Propylene-Ethylene copolymers," University of Nebraska - Lincoln, 2013.

[70] W. Brian Black, "Wall slip and boundary effects in polymer shear flows," *University of Winsconsin-Madison,* 2000.

[71] Hans Zuidema, "Flow Induced Crystallization of Polymers, Application to Injection Moulding," Technische Universiteit Eindhoven, Eindhoven, 2000.

[72] Rajesh H. Somani, Ling Yang, Lei Zhu and Benjamin S. Hsiao, "Flow-induced shish-kebab precursor structures in entangled polymer melts," *Polymer,* vol. 46, p. 8587–8623, 2005.

[73] K. Zapala, . E. Piorkowska, . A. Hiltner and . E. Baer, "High-pressure crystallization of isotactic polypropylene droplets," *Colloid Polym Sci,* vol. 290, no. 16, p. 1599–1607, 2012.

[74] U. Goschel, G. Peters, H. Meijer and F. Swartjes, "Crystallization in isotactic polypropylene melts during contraction flow: time-resolved synchrotron WAXD studies," *Polymer,* vol. 41, p. 1541–1550, 2000.

[75] S. o. P. E. T. Conference, ANTEC '96:Plastics--racing Into the Future : Conference Proceedings, Brookfield, Conn, 1996.

[76] B.E.Read, "Proceedings of the International Discussion Meeting on Relaxations in Complex Systems," Vols. 131-133, 408, 1991.

[77] V. P. Skripov, Metastable Liquids, New York, 1973.

[78] R. Somani, L. Yang and B. Hsiao, "Effects of high molecular weight species on shear-induced orientation," *Polymer,* vol. 47, no. 15, p. 5657–5668, 2006.

[79] M.A. Larson and J. Garside, "Solute clustering in supersaturated solutions," *Chemical Engineering Science,* vol. 41, no. 5, pp. 1285-1289, 1986.

[80] B. Monasse and J. M. Haudin, Molecular structure of polypropylene homopolymer and copolymer-B, Springer, 1995.

[81] Joannes Leonardus Jurrian Zijl, "Polymers in extensional flow, A comparison of microscopic and macroscopic simulations with birefringence experiments," aan de Technische Universiteit Delft, 2001.

[82] I. K. Park and H. D. Noether, "Crystalline “Hard” Elastic Materials," *Colloid and Polymer Science,* vol. 253, no. 10, pp. 824-839, 1975.

Appendix

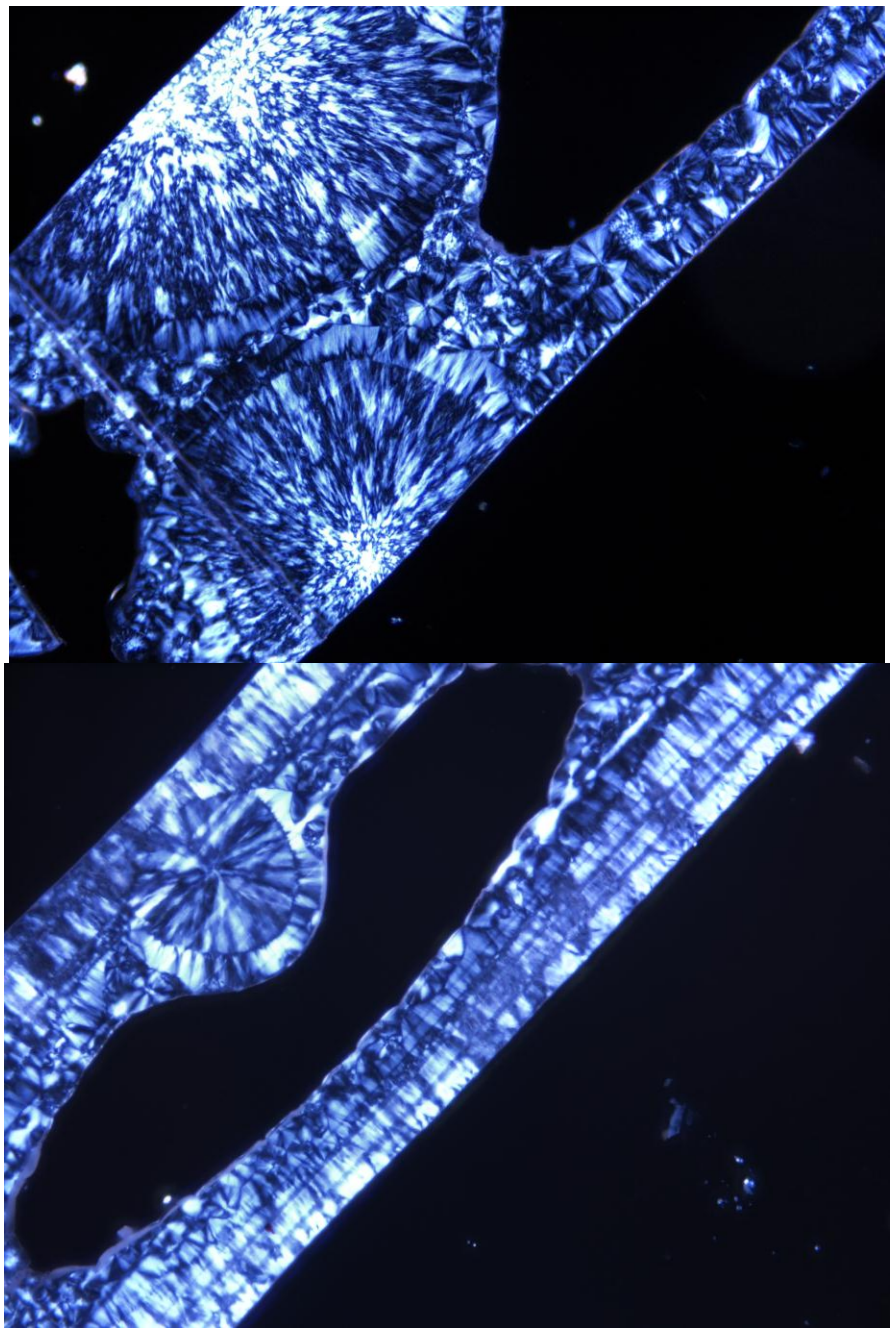

Figure 0.1 Optical microscopy of Quiescent crystallization of Raco3 (Top) and Raco7 (Bottom) after more than 70 hours of isothermal crystallization.

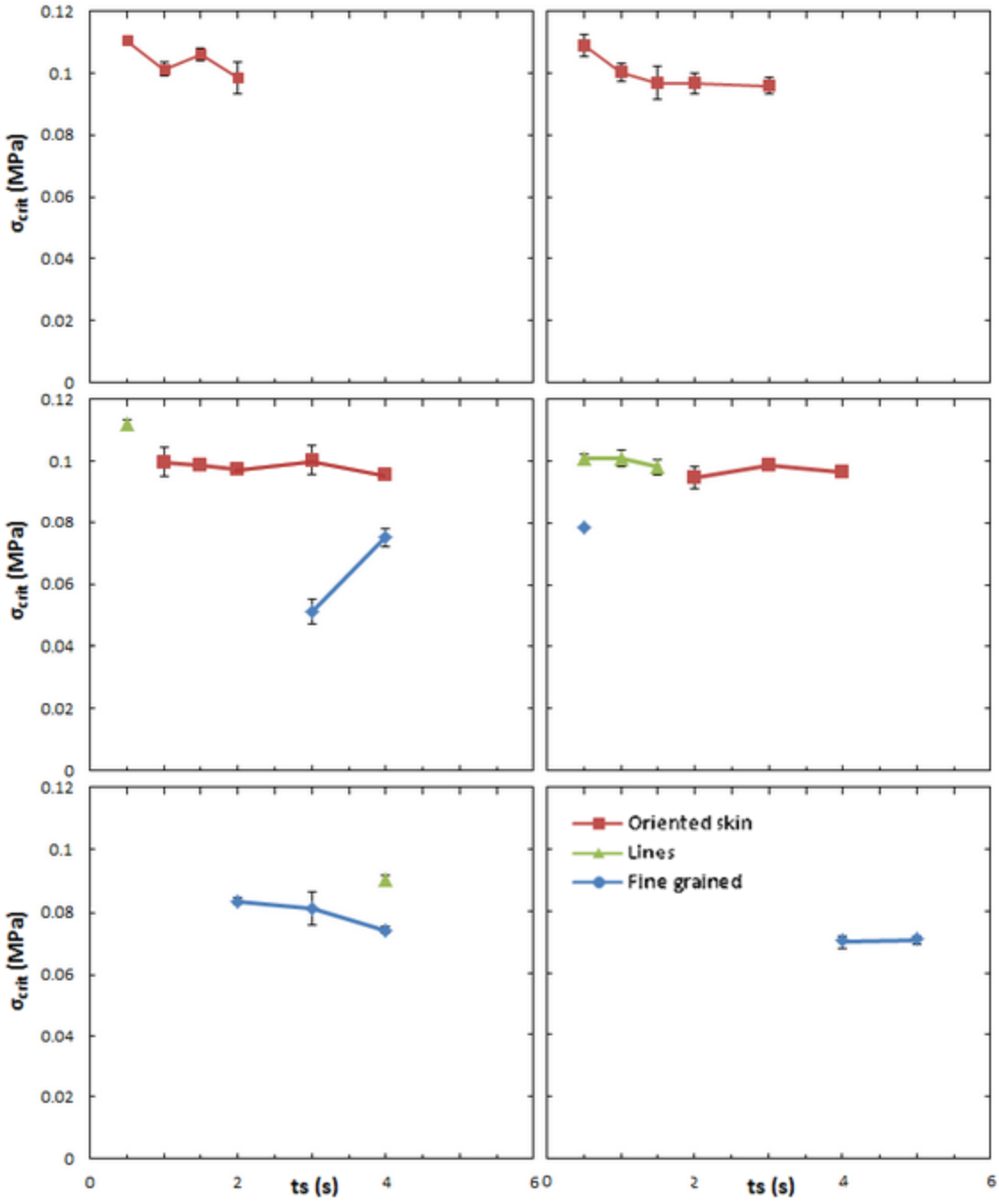

Figure 0.2 Critical shear stresses of Raco3 for oriented skin, lines and fine grained layer.

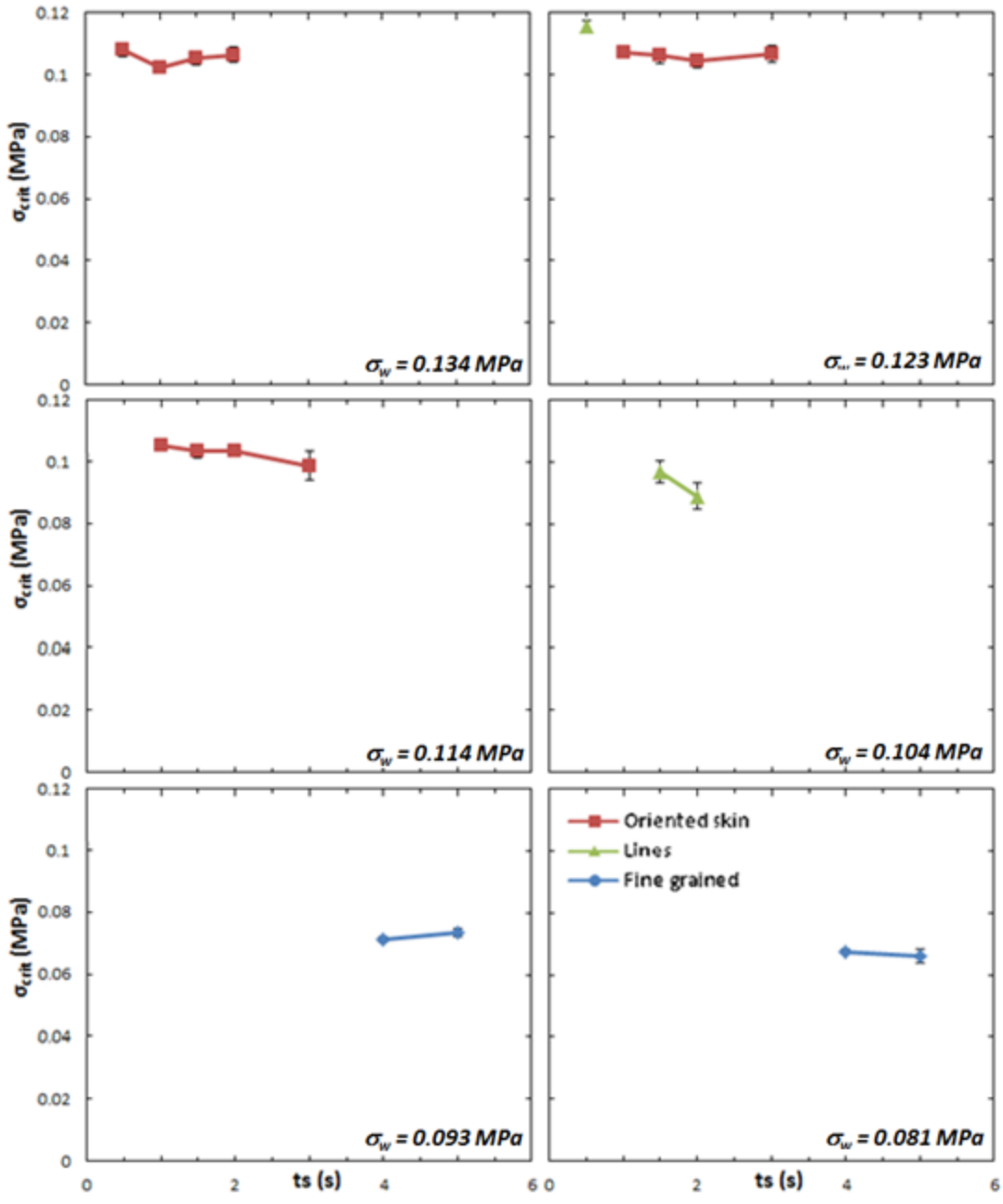

Figure 0.3Critical shear stresses of Raco7 for oriented skin, lines and fine grained layer.

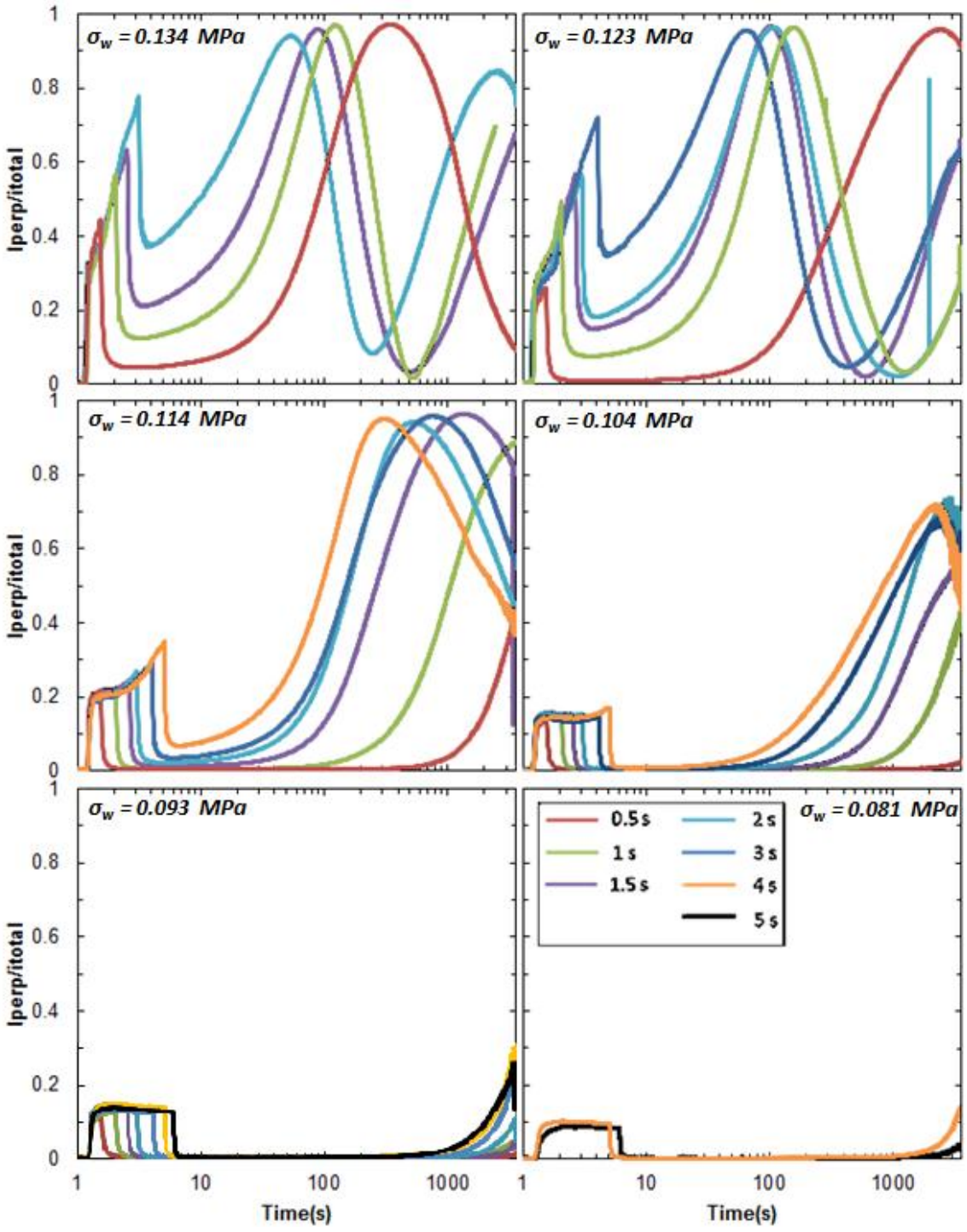

Figure 0.4 Measurements of birefringence for Raco3 for several σ_w and t_s.

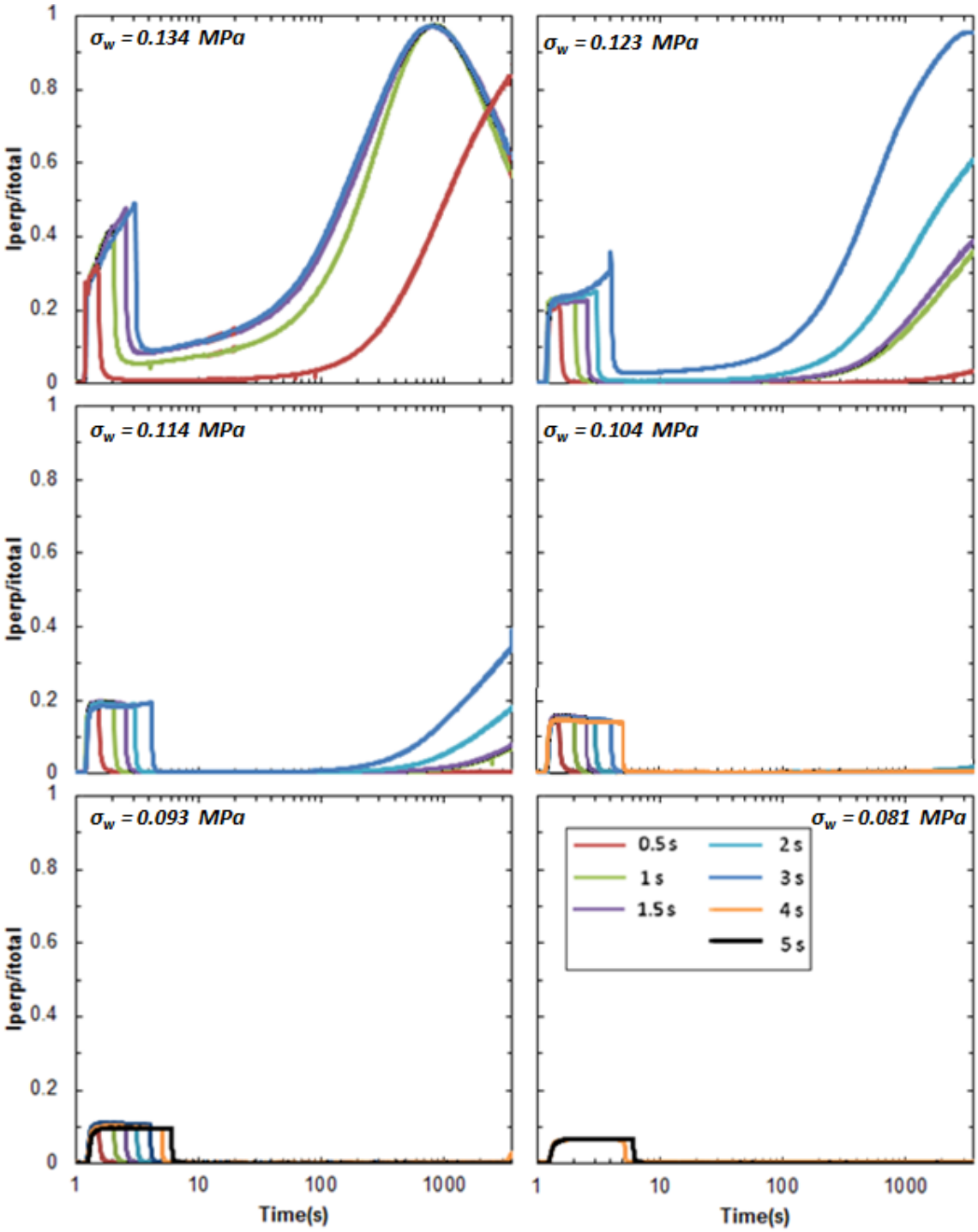

Figure 0.5 Measurements of birefringence for Raco7 for several σw and ts.

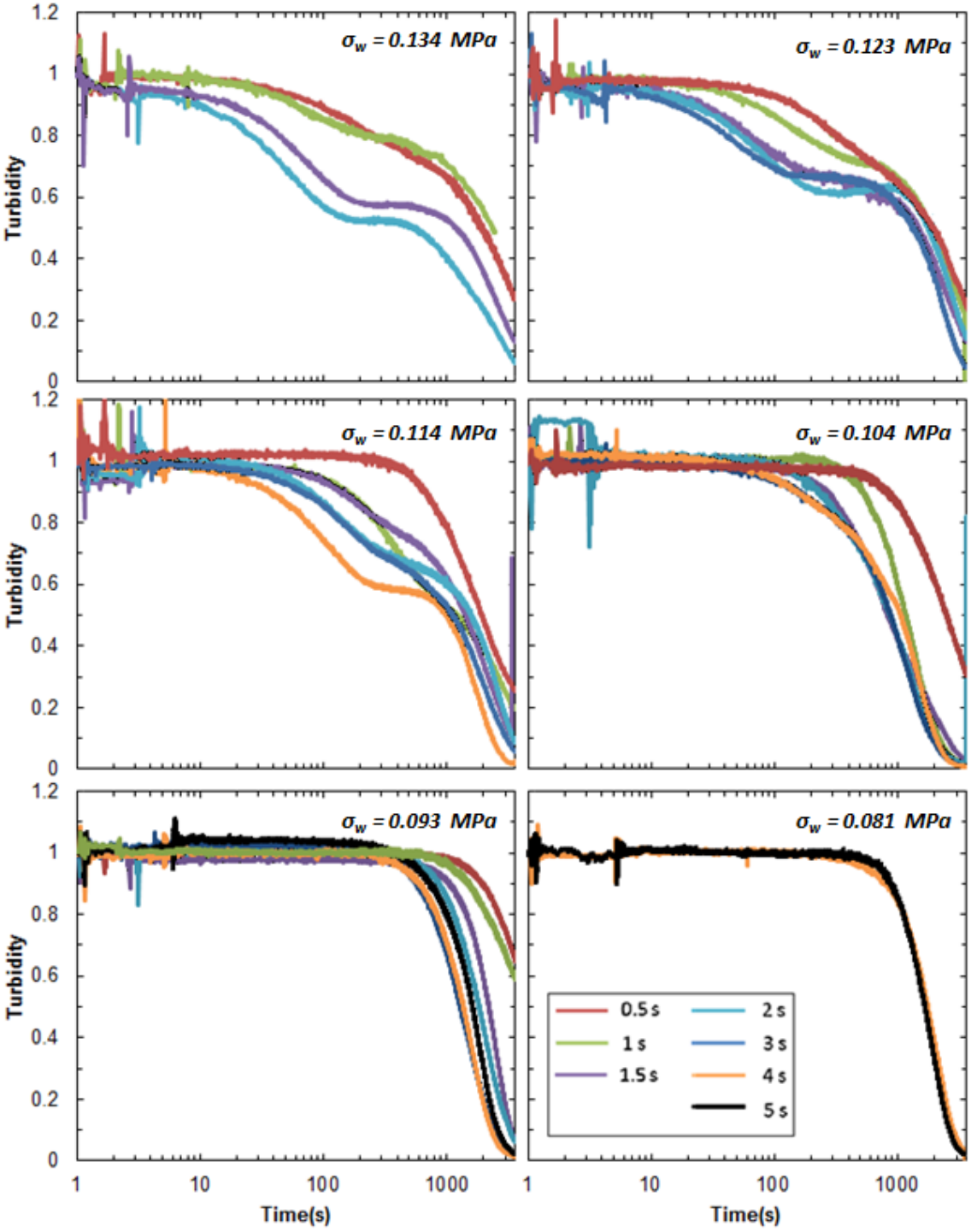

Figure 0.6 Measurements of turbidity for Raco3 for several σw and ts.

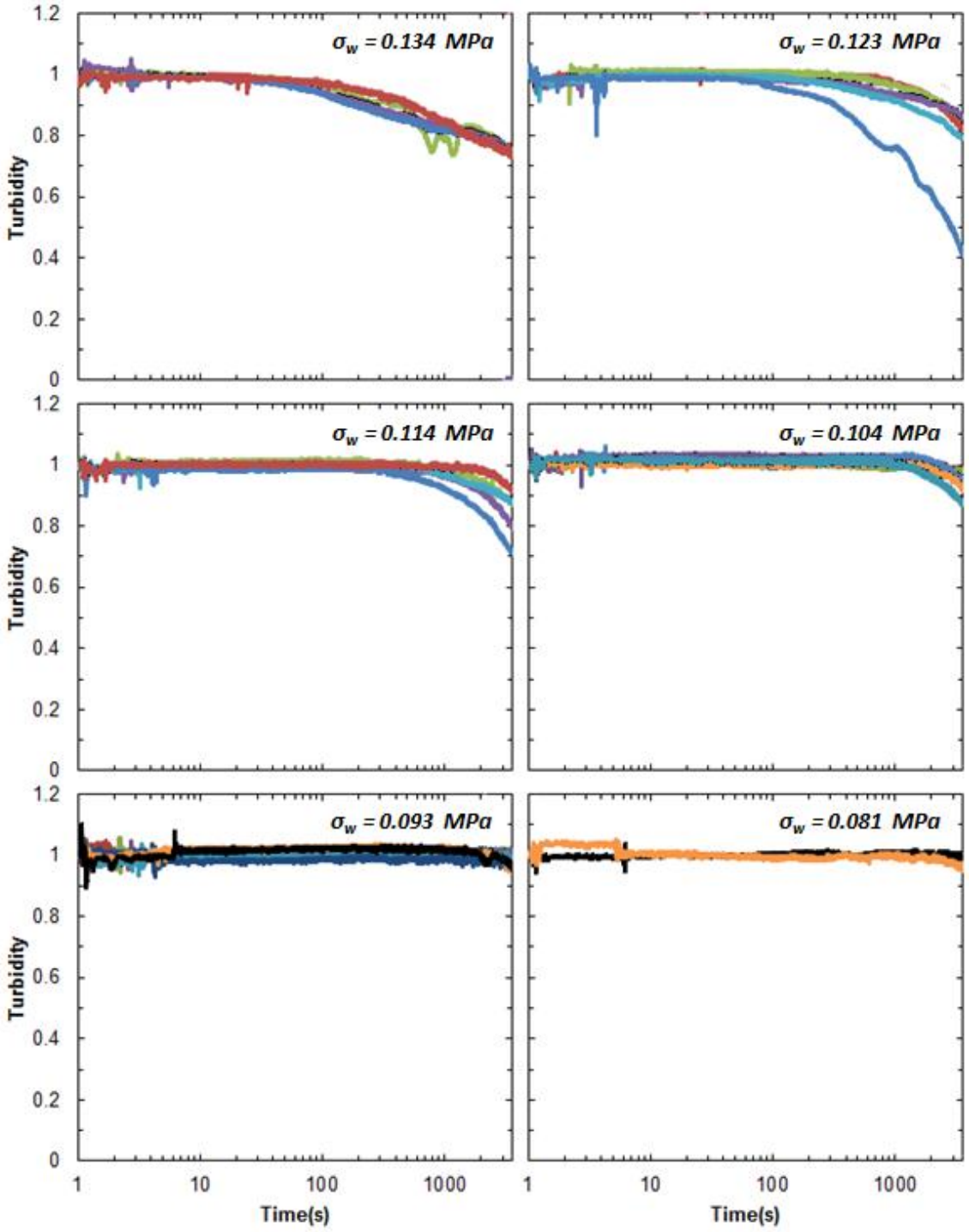

Figure 0.7 Measurements of turbidity for Raco7 for several σw and ts.

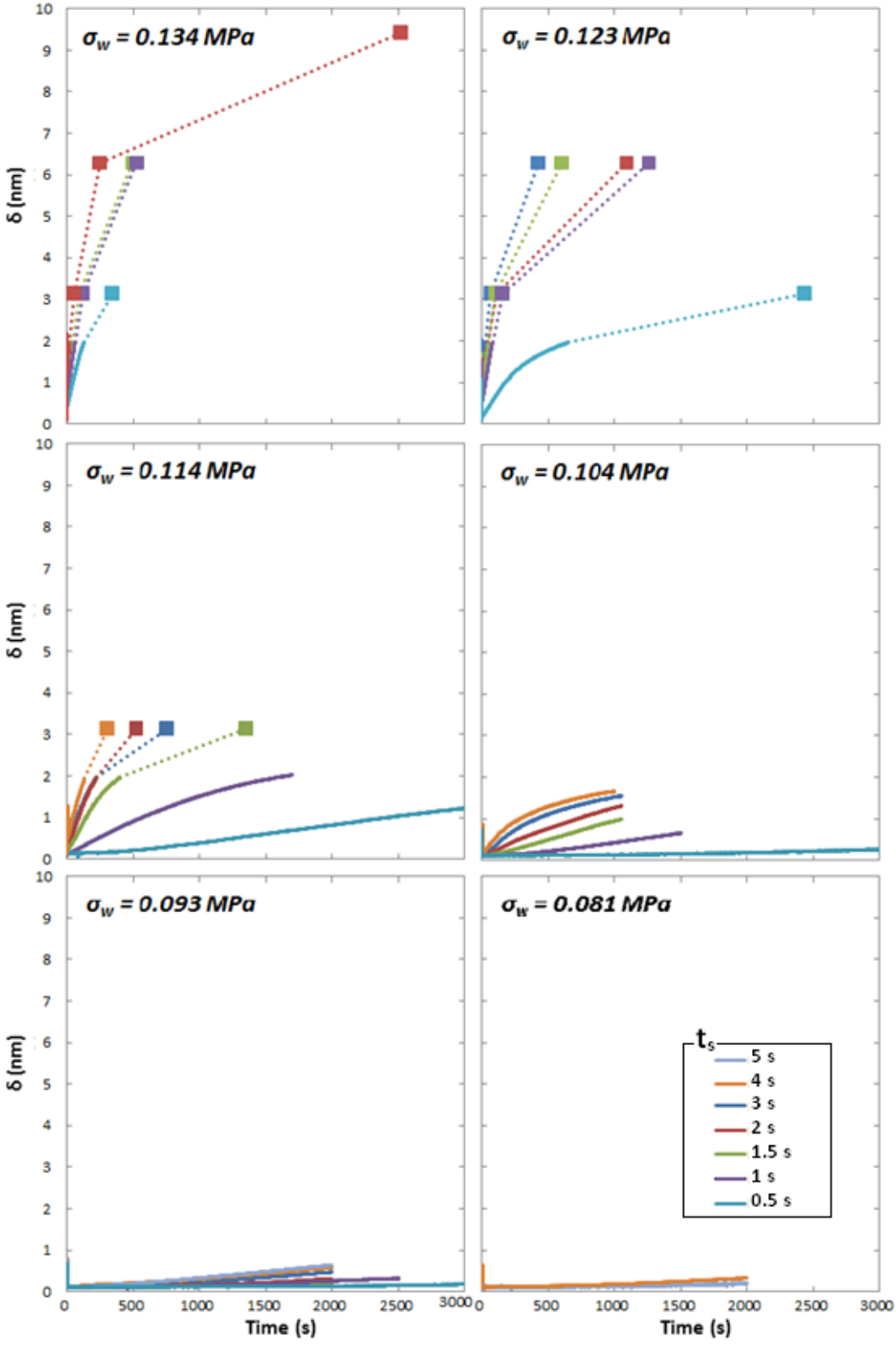

:

Figure 0.8 Measurements of retardance for Raco3 for several σw and ts.

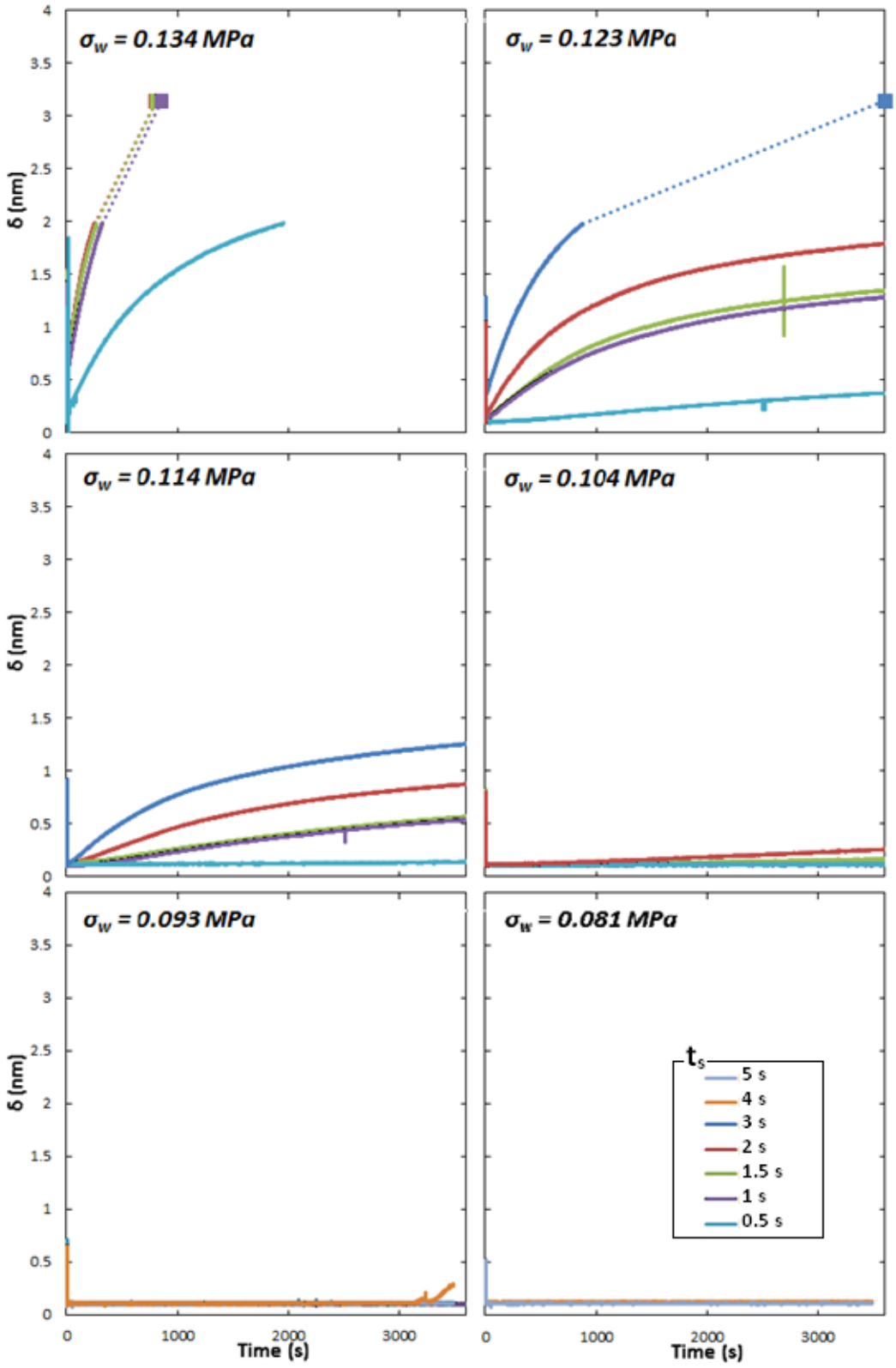

Figure 0.9Measurements of retardance for Raco7 for several σw and ts.

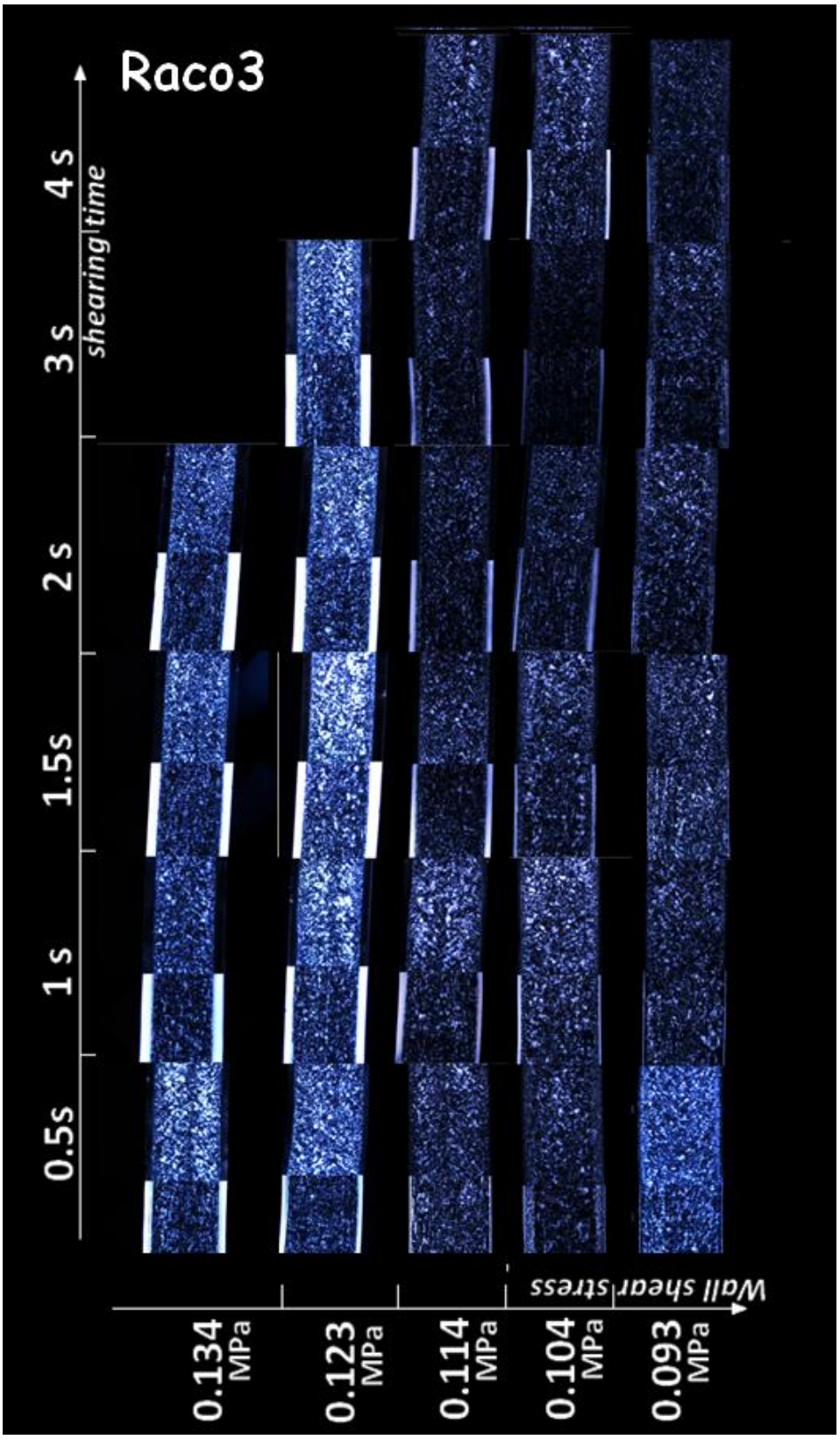

Figure 0.10 Micrographs of samples cuts of Raco3 ordered by shearing time and shearing stress.

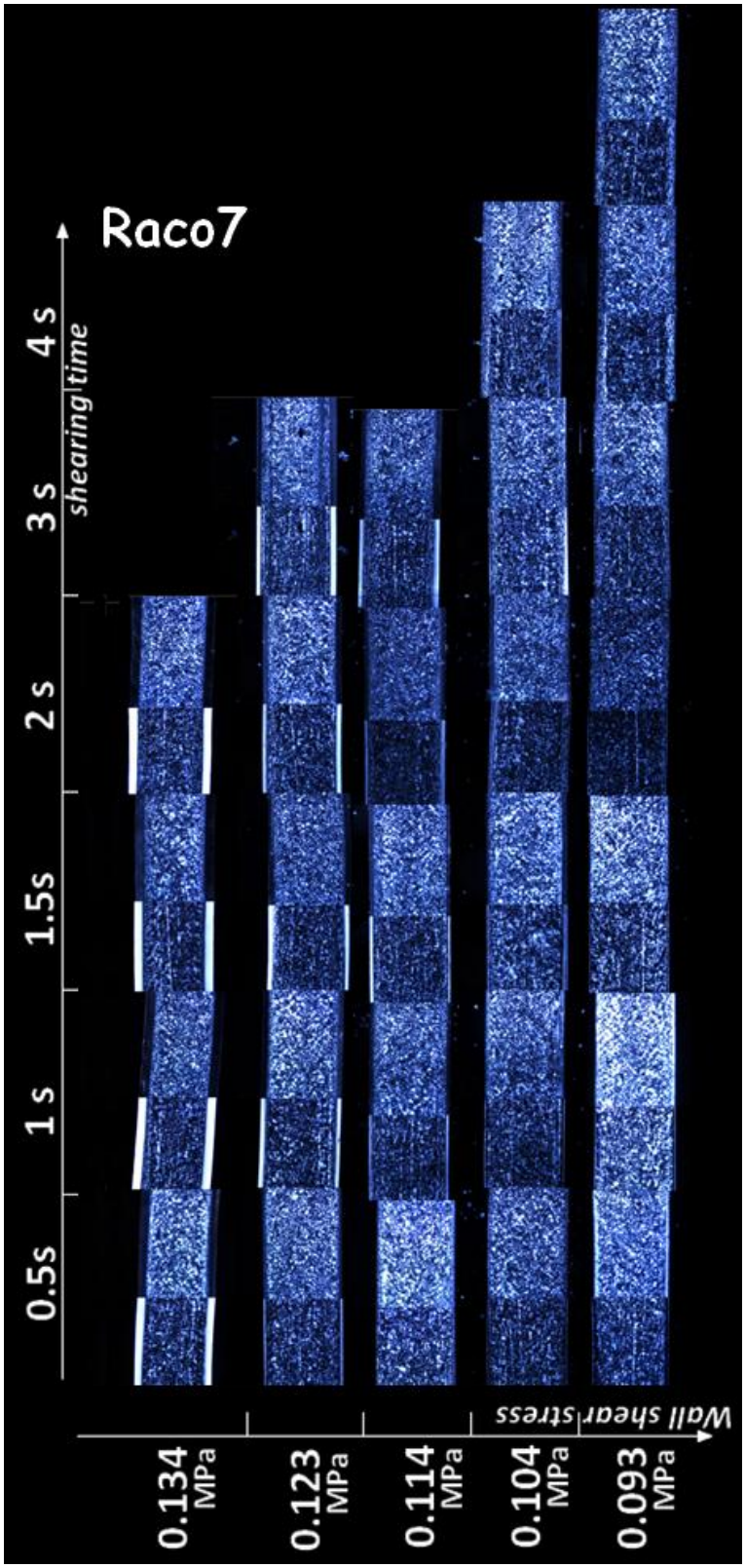

Figure 0.11 Micrographs of samples cuts of Raco7 ordered by shearing time and shearing stress.

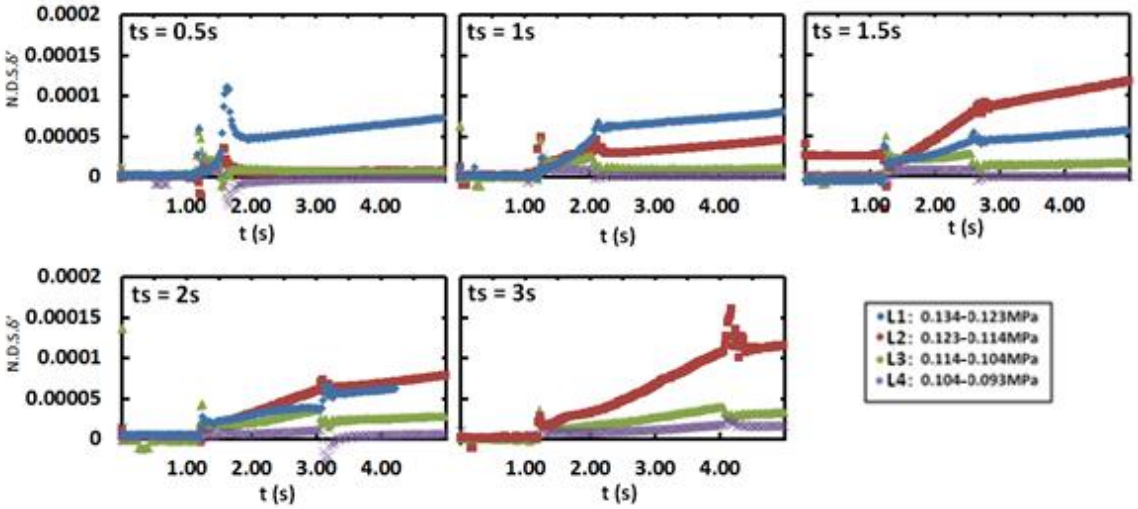

Figure 0.12 Depth sectioning comparison of iPP for different ts.

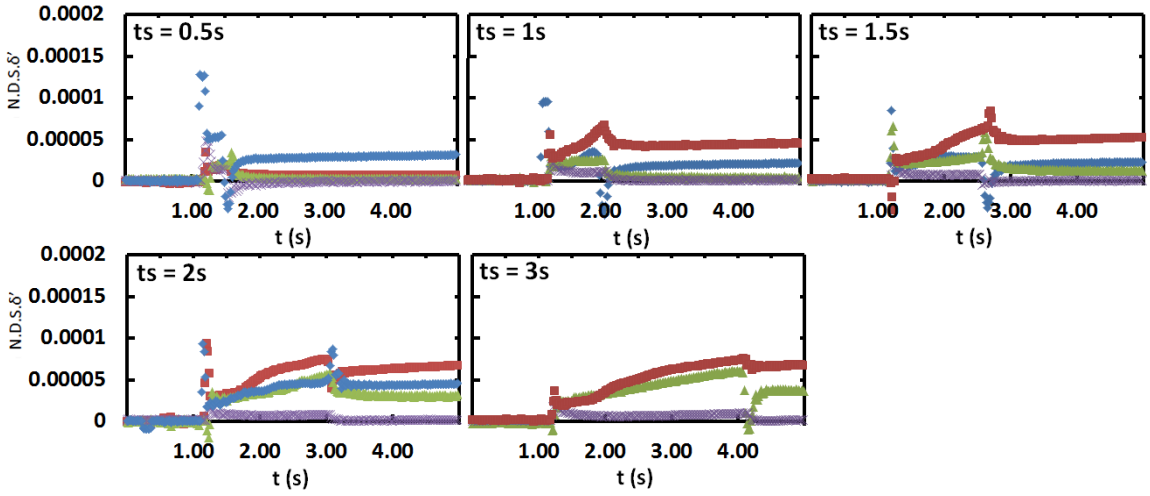

Figure 0.13 Depth sectioning comparison of Raco3 for different ts.

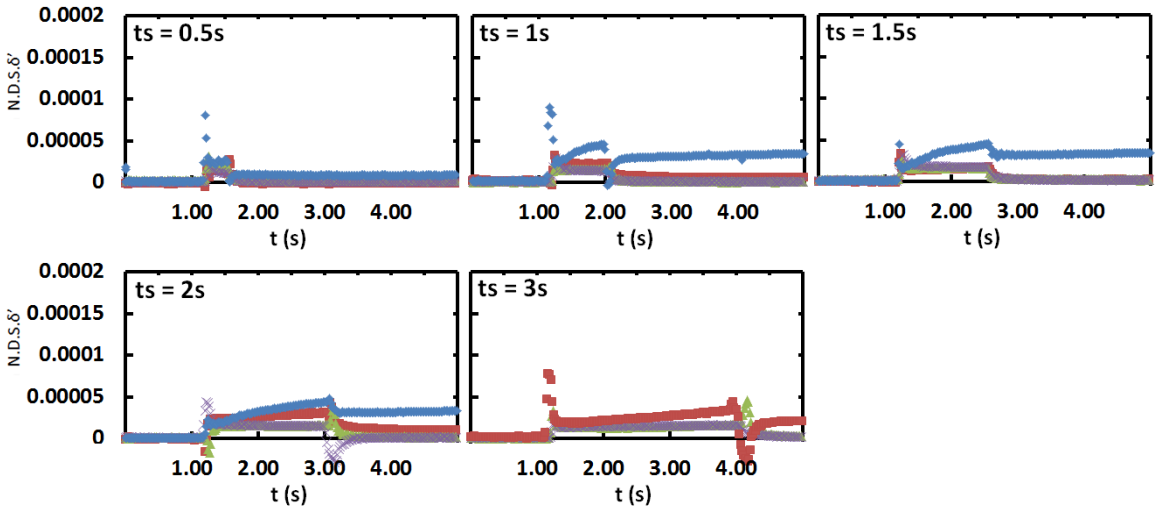

Figure 0.14 Depth sectioning comparison of Raco7 for different ts.

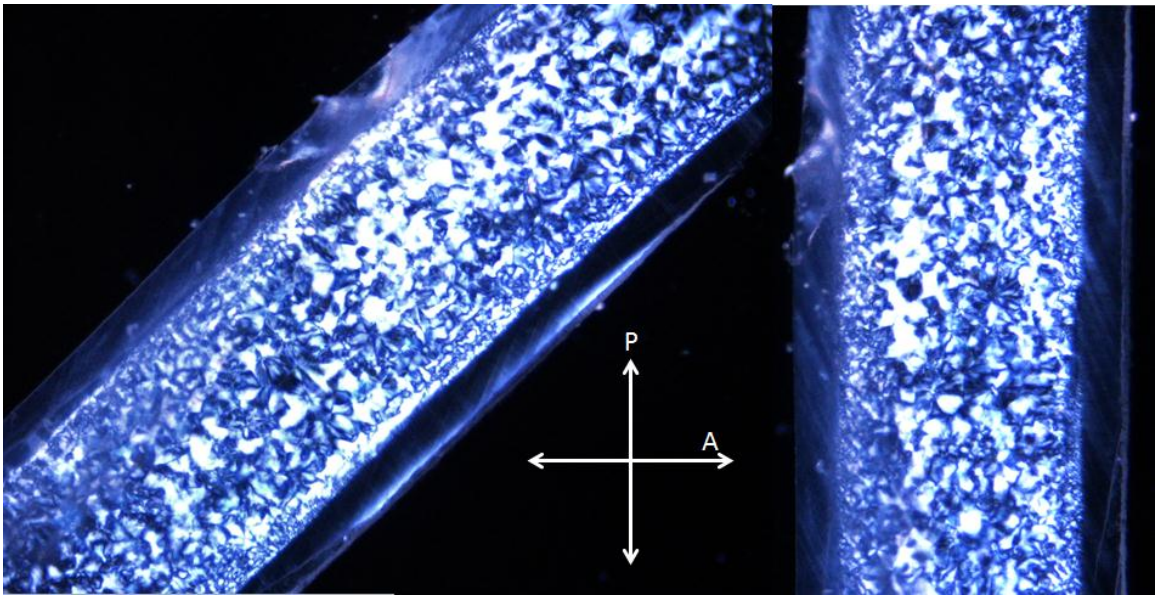

Figure 0.15 Optical Polarized Micrograph of a transversal cut (perpendicular to flow) of a highly oriented specimen (Raco7 σ_w = 0.134MPa and ts = 2s).

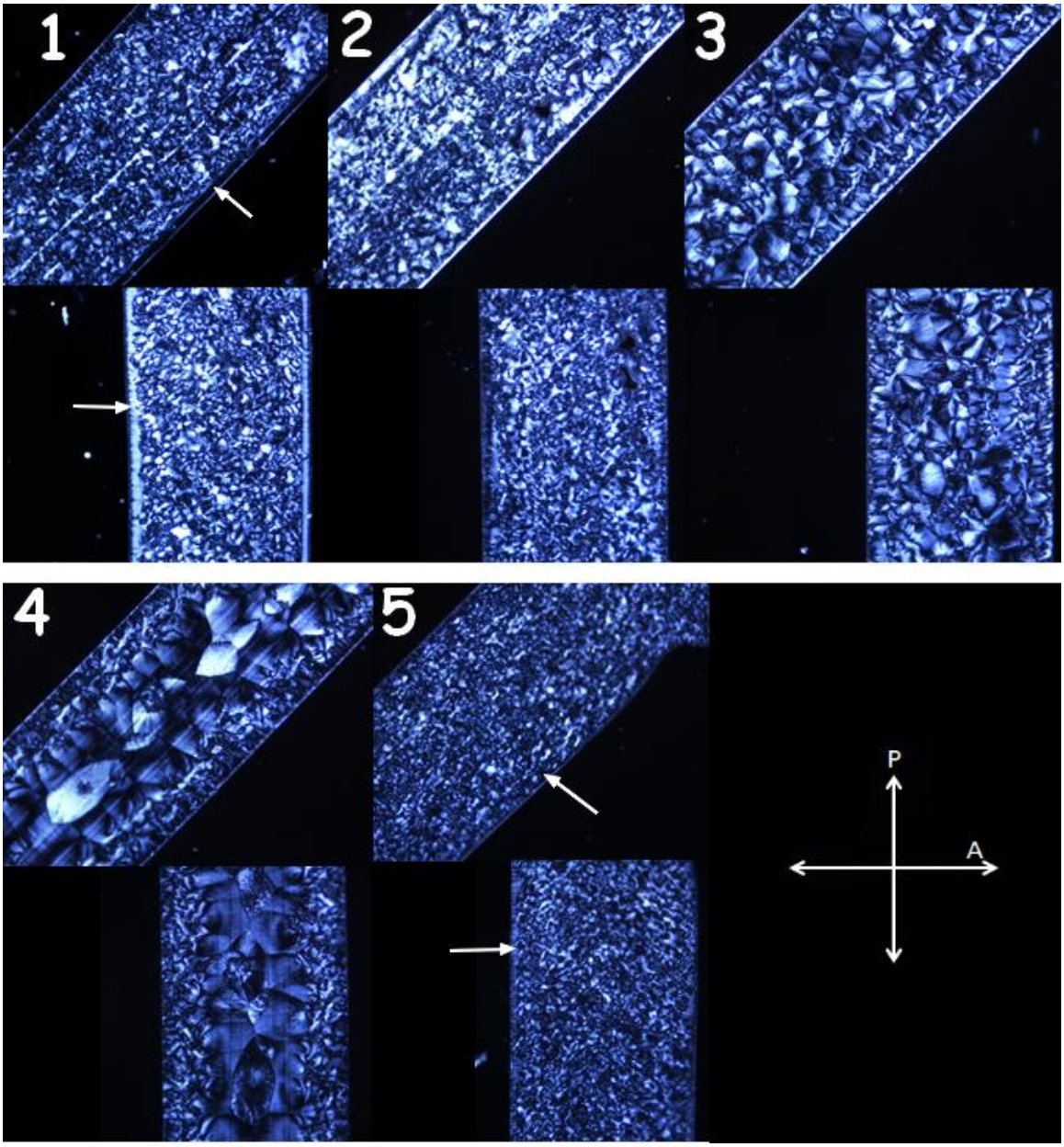

Figure 0.16 Black layer specimens : 1) regular experiment, 2) 11 hours crystallization, 3) slow cooling, 4) Quench at 100°C, 5) Quench at 80°C.